THESIS FOR THE DEGREE OF DOCTOR OF PHILOSOPHY

From data to models: a purpose-driven framework for catalyst modelling in automotive applications.

Andres F. Suarez-Corredor

Department of Chemistry and Chemical Engineering
Chalmers University of Technology
Gothenburg, Sweden, 2026

From data to models: a purpose-driven framework for catalyst modelling in automotive applications.

Andres F. Suarez-Corredor
ISBN 978-91-8103-374-8

Doktorsavhandligar vid Chalmers Tekniska Högskola
Chalmers Tekniska Högskola
Ny serie nr 5831
ISSN 0346-718X

Department of Chemistry and Chemical Engineering
Chalmers University of Technology
SE-412 96 Gothenburg, Sweden
Phone: +46 (0)31 772 1000
www.chalmers.se

Cover: The nuance between the digital and physical in a truck.

Printed by Chalmers Digitaltryck
Gothenburg, Sweden, March 2026

"Doubt is an uncomfortable condition, but certainty is a ridiculous one."

— Voltaire

Abstract

Combustion engines will remain important in heavy-duty transport for years, especially in long-haul and marine shipping. During this transition, emission aftertreatment is one of the fastest ways to reduce harmful pollutants from vehicles already in use. Stricter regulations (such as Euro 7 and EPA 27) demand low emissions during rapid transients and across a wide operating range with detailed monitoring strategies.

To meet this challenge, mechanistic catalyst models are essential. By embedding physics and chemistry in the model structure, they provide insight, transparency, and better control than purely black-box approaches. They also enable hybrid strategies that combine physical modelling with data-driven methods, while keeping a clear link to real mechanisms and parameters.

This thesis advances modelling for Selective Catalytic Reduction (SCR) catalysts in lean-burn engines, focusing on vanadium-based NH_3-SCR and Pd-based H_2-SCR. The work targets both mechanistic understanding and model quality. A workflow is developed from experiments to validated models: reactor characterization to correct dispersion and delay effects, steady-state analysis to create model structures using a data-driven framework, and model discrimination to reduce overfitting and parameter correlation.

For vanadium-based NH_3-SCR, experiments and modelling are combined to capture NH_3 adsorption and internal mass transfer in a monolith reactor. Model structures are treated as variables and optimized with a custom algorithm, supported by new objective functions that improve robustness. The final model identifies five Langmuir-type NH_3 adsorption sites with different behavior to temperature and water. Steady-state parameters are linked to thermodynamic properties, strengthening physical meaning and parameter validity. Internal mass transfer is assessed using two washcoat formulations and by considering non-square channels. The result is a compact, detailed model that captures key SCR dynamics and improves prediction of transient responses across wide conditions.

For Pd-based H_2-SCR aimed at lean H_2 engines, 1 wt% Pd catalysts on Al_2O_3, TiO_2, BEA zeolite, and SSZ-13 zeolite are tested from 100–300°C under varying H_2/NO ratios in dry and wet conditions. Pd/TiO_2 gives the highest NO conversion and N_2 yield, consistent with material characterization. A kinetic model coupled with mass transfer simulates NO reduction to N_2, N_2O, and NH_3, together with H_2 oxidation, and reproduces trends for all supports. NH_3 forms only on Pd/TiO_2, while N_2O forms on all supports and is unaffected by water concentration. External mass transfer is shown to limit fast H_2 oxidation, increasing H_2 available for NO reduction.

Keywords: Catalyst Modelling, Modelling Framework, NH_3-SCR, H_2-SCR.

Sammanfattning

Förbränningsmotorer kommer att vara viktiga inom tung transport i många år, särskilt för långväga trafik och marin drift. Under denna omställning är avgasrening en av de snabbaste vägarna att minska skadliga utsläpp från fordon som redan används. Strängare regler (som Euro 7 och EPA 27) kräver låga utsläpp vid snabba transienter och över ett brett driftområde, tillsammans med detaljerade övervakningsstrategier.

För att klara detta behövs mekanistiska katalysatormodeller. Genom att bygga in fysik och kemi i modellens struktur ger de insikt och transparens, och bättre styrbarhet än rena "black-box"-metoder. De möjliggör också hybrida strategier som kombinerar fysikalisk modellering med datadrivna metoder, samtidigt som kopplingen till verkliga mekanismer och parametrar bevaras.

Denna avhandling utvecklar modellering av SCR-katalysatorer för magra motorer, med fokus på vanadinbaserad NH_3-SCR och Pd-baserad H_2-SCR. Arbetet riktar sig både mot mekanistisk förståelse och modellkvalitet. Ett arbetsflöde tas fram från experiment till validerade modeller: reaktorkarakterisering för att korrigera dispersions och fördröjningseffekter, stationär analys för att skapa modellstrukturer med ett datadrivet ramverk, samt modelldiskriminering för att minska överanpassning och parameterkorrelation.

För vanadinbaserad NH_3-SCR kombineras experiment och modellering för att beskriva NH_3-adsorption och intern masstransport i en monolitreaktor. Modellstrukturer behandlas som variabler och optimeras med en egenutvecklad algoritm, stödd av nya målfunktioner som förbättrar robustheten. Den slutliga modellen identifierar fem Langmuir NH_3-adsorptionssäten med olika känslighet för temperatur och vatten. Stationära parametrar kopplas till termodynamiska egenskaper, vilket stärker den fysikaliska tolkningen och parameterernas giltighet. Intern masstransport bedöms med två washcoat-formuleringar och genom att även beakta icke-kvadratiska kanaler. Resultatet är en kompakt men detaljerad modell som återger viktig SCR-dynamik och förbättrar prediktion av transient respons över omfattande driftförhållanden.

För Pd-baserad H_2-SCR för magra H_2 motorer testas 1 vikt-% Pd-katalysatorer på Al_2O_3, TiO_2, BEA-zeolit och SSZ-13-zeolit vid 100–300°C, med varierande H_2/NO-förhållanden i torra och våta förhållanden. Pd/TiO_2 ger högst NO-omvandling och N_2-utbyte, i överenstämmelse med materialkarakterisering. En kinetisk modell kopplad till masstransport simulerar NO reduktion till N_2, N_2O och NH_3, tillsammans med H_2 oxidation, och återger trender för alla bärarmaterial. NH_3 bildas endast på Pd/TiO_2, medan N_2O bildas på alla bärarmaterial och är opåverkad av vattenhalten. Extern masstransport påvisas begränsa snabb H_2 oxidation, vilket ökar mängden H_2 som finns tillgänglig för NO reduktion.

Nyckelord: Catalyst Modelling, Modelling Framework, NH_3-SCR, H_2-SCR.

List of Publications

This thesis is based on the following publications:

[A] **A. Suarez-Corredor**, M. Bäbler, L. Olsson, M. Skoglundh, and B. Westerberg, "Characterization Method for Gas Flow Reactor Experiments - NH_3 Adsorption on Vanadium-based SCR Catalysts". Published in Ind. Eng. Chem. Res., 2021, 60, 30.

[B] **A. Suarez-Corredor**, M. Bäbler, L. Olsson, M. Skoglundh, and B. Westerberg, "Understanding the NH_3 Adsorption Mechanism on Vanadium-based SCR Catalyst: A Data-driven Modeling Approach". Published in Chem. Eng. Sci., 2022, 262.

[C] **A. Suarez-Corredor**, J. Shao, M. Bäbler, B. Westerberg, and L. Olsson, "Influence of Catalyst Supports on H_2-SCR Catalysts: A Combined Experimental and Modelling Approach Including Mass Transfer.". Submitted for publication in Appl. Catal. B.

[D] **A. Suarez-Corredor**, M. Bäbler, L. Olsson, A. Widd, M. Skoglundh, and B. Westerberg, "NH_3 Adsorption Dynamics in a Vanadium-based SCR Catalyst: Implications of an Improved Mass Transfer Description". Manuscript.

Conferences Presentations

1. Multi-scale modeling approach to the nature of active sites for a vanadium -based SCR catalyst.
   Suarez-Corredor, Andres F.
   Presented at the 11th International Conference on Environmental Catalysis.
   Manchester, UK, 6-9 September 2020.

2. Multi-scale modeling approach to the nature of active sites for a vanadium -based SCR catalyst: NH_3 Adsorption.
   Suarez-Corredor, Andres F.
   Presented at the Crosscut Lean Exhaust Emissions Reduction Simulation (CLEERS) Workshop 2021.
   Virtual, 13-17 September 2021.

3. Maximizing information with a data-driven modeling framework for NH_3 adsorption in a vanadium-based SCR catalyst.
   Suarez-Corredor, Andres F.
   Presented at the 12th International Conference on Environmental Catalysis.
   Osaka, Japan, 30 July – 2 August 2022.

4. A data-driven modeling framework to develop an NH_3 adsorption model for a vanadium-based SCR catalyst.
   Suarez-Corredor, Andres F.
   Presented at the 7th International Symposium on Modelling of Exhaust-Gas After-Treatment (MODEGAT).
   Bad Herrenalb, Germany, 11-13 September 2022.

5. Ammonia Adsorption in an SCR Catalyst: Improved Mass Transfer Modeling Using a Data-Driven Framework.
   Suarez-Corredor, Andres F.
   Presented at ASME-ICEF Crosscut Lean Exhaust Emissions Reduction Simulation (CLEERS) Workshop 2023.
   Pittsburgh, USA, 8-11 October 2023.

6. Ammonia Adsorption in an SCR Catalyst and NH_3 oxidation. Modelling using a Data-Driven Framework.
   Suarez-Corredor, Andres F.

Presented at FuturEMission 2024 Conference.
Karlsruhe, Germany, 21-23 July 2024.

7. Towards Improved SCR catalyst models: A framework for NH_3 adsorption, mass transfer, and redox dynamics.
Suarez-Corredor, Andres F.
Presented at the 8th International Symposium on Modelling of Exhaust-Gas After-Treatment (MODEGAT).
Bad Herrenalb, Germany, 21-23 September 2025.

Author's Contributions

Before presenting the summary of contributions, I briefly describe the experimental and modelling workflow developed in this thesis. The framework covers how experimental data were collected and used to build catalyst models. The main experimental method in this thesis was a gas-flow reactor, a well-known tool for measuring catalytic activity under controlled conditions. However, for modelling purposes, data needs to be obtained through a careful design of experiments that maximizes information, allows the identification and treatment of artifacts, and ensures that the features of interest are properly decoupled. The modelling framework then focused on creating robust algorithms capable of finding global optima in a highly non-linear problem while keeping the computations feasible within the available resources, and the resulting models were finally used to gain insight into the system, enabling fast and detailed analysis of aspects that would otherwise be costly or difficult to measure experimentally.

Paper A (Main author): For Paper A, I developed the NH_3 adsorption experimental method for deployment in the gas-flow reactor, in collaboration with the fifth author. The experimental work involved operating, troubleshooting, and maintaining the gas-flow reactor to ensure reliable data. I created the algorithm to process the experimental data, characterize the reactor, and remove artifacts, ensuring reliable NH_3 adsorption/desorption measurements. The residence-time-distribution model used to characterize the reactor was proposed and developed together with the second author. Further work done for this paper included the development of analysis and visualization tools for benchmarking the method, preparation of the first draft of the manuscript, and improving the manuscript based on feedback from the co-authors. Part of the work done for this paper involved the submission of the manuscript and the coordination of the peer-review comments.

Paper B (Main author): For Paper B, I devised the concept for the data-driven modelling workflow used to calibrate the steady-state NH_3 adsorption model. The experimental data used were the same as those processed in Paper A. I implemented the workflow on a high-performance computing (HPC) system, including the development of an automated procedure to run and report multiple models. The NH_3 adsorption model and the building blocks used in the workflow were created by the collaboration with the fifth author. The methods for model discrimination, the definition of quality indicators,

and the visualization tools for analyzing the modelling results were developed as part of this work. I conducted a literature review to connect the modelling parameters with the adsorption properties, providing the basis for discussions with the co-authors on their physical significance. I prepared the first draft of the manuscript and completed the final version together with the other authors. I also managed the manuscript submission and the peer-review process with the support of the other authors.

Paper C (Main author): For Paper C, I designed the experimental method for measuring catalytic activity in the gas-flow reactor, supported by discussions with the co-authors. I created the modelling workflow, which includes the kinetic parameters in the power-law framework and the mass-transfer analysis with valuable contributions from the third author. I worked on identifying the connection between the obtained kinetic parameters and the existing literature, as well as relating these parameters to the characterization results produced by the second author. The first draft of the manuscript, excluding the catalyst characterization section, was prepared with active support from the fourth author, and the final version was completed together with all co-authors. I also took the responsibility for submitting the manuscript and handling the peer-review process with the help of the other authors.

Paper D (Main author): For Paper D, I adapted the preprocessing method to handle time-series data from the experimental data from Paper A and B. The model framework and its deployment on the HPC system were developed as part of this work. The modelling approach includes the implementation of a conventional single-channel model with heat and mass balances, carried out under the supervision of the sixth author. Also, I worked on the integration of the kinetic parameters obtained in the steady-state modelling framework (Paper B) into the NH_3 dynamic model developed here. Additional contributions include performing the N_2 physisorption measurements and optical microscopy, processing these data. Strategies to account for non-square channels and non-homogeneous washcoat porosity were designed and implemented with input from the sixth author. I prepared the first draft of the manuscript, and the final version was completed together with the co-authors.

Acknowledgments

This research project was sponsored by Scania CV AB. The Competence Centre for Catalysis is hosted by Chalmers University of Technology and financially supported by the Swedish Energy Agency (Project No. 52689-1) and the member companies Johnson Matthey, Perstorp, PowerCell Sweden, TRATON, Umicore, VAROPreem and Volvo Group.

Beyond this formal acknowledgement of funding, I would now like to turn to the people behind the work, the mentors, colleagues, friends, and family whose support carried me through this journey.

Life is, most of the time, random and full of uncertainty, little accidents, constant change. The ups and downs are what make life worth living, and for all the experiences I lived during this project, I am extremely thankful. This project took more time than expected, and there were deviations from the original plan that led to an amazing learning experience, both as a professional and as a person. However, this journey would not have been possible without the people who were always there, with their stability, their unconditional support, their experience and learnings, their kindness, and the warmth and humanity that is often missing in relationships that are so ephemeral: merely academic, merely work-related. Too often, those relationships do not let us show who we truly are, in our vulnerabilities, in our defects. And yet it is precisely this transparent human state that lets us find the greatest treasures: knowledge, mentorship, friendship, belonging.

I owe this project to the best mentors I could ever have asked for, Dr. Björn Westerberg and Prof. Matthäus Bäbler. Life has changed a lot in recent years, but you were always there, encouraging, supporting, pushing for excellence, being critical, and at the same time empathetic and caring. That combination gives me hope for how knowledge, science, and engineering, done with value, ambition, and heart, should be carried in a world where systems sometimes seem corrupted or uninspired, driven by the rush to be noticed rather than to be relevant; chasing visibility instead of the reward of finding something new, of understanding a little more of the complexity of our world. I will always be thankful for the opportunity to work with you, and I hope we can have more endeavours like this one.

I also want to thank my other collaborators, Prof. Louise Olsson and Prof. Magnus Skoglundh. Louise, thank you for your support in navigating the scientific and academic tasks that a Ph.D. demands. Magnus, I truly appreciate

your support, your empathy for our project, and your optimism about the results we achieved. It was always encouraging to hear your positive words and to feel your trust as we continued our work. I also want to thank Dr. Anders Widd for the fruitful discussions we had on a monthly basis during this project, where knowledge, experience, and encouragement were shared. These meetings were vital for trying new things and questioning the way we did things.

I would like to thank all the people I was lucky to work with and collaborate with at Scania CV AB. Each interaction contributed immensely to building knowledge and creating valuable experiences. Especially, I want to thank the managers who supported me throughout this journey, Karl Rejnö, Martina Levin, and Klara Lizarraga. Thank you for appreciating our work and seeing the value in it, for advocating for it, and for helping it find its place in the organisation. I also want to thank Klas Olofsson, Roger Olsson, Victoria Lindberg, and Lars-Göran Nylén for all the administrative support, managerial assistance, and experience-sharing during my time at Scania. Thanks to you, I was able to focus on the project, knowing that everything related to administrative tasks was running smoothly.

At Scania, I also want to acknowledge the following colleagues, who shared knowledge, friendship, great energy, and helped me grow personally and professionally. I want to thank Petra Holsten for always bringing a contagious positive energy, and for her approach to work, always with enthusiasm and high standards. To Daniel Danielsson, for his wisdom, his experience, and his easy way of sharing knowledge, together with his curiosity about life and work. To Sara Lögdberg: we have worked together for a long time in the TWC realm, and I will always remember the support, the discussions, and the curiosity to reach a high technical level. Your discipline and rigour in doing proper, fact-based development are virtues the company should take as an example.

I want to thank Brad Adelman for his energy and support, for always bringing the bright side and the humour when things were not working as they should, and for how easy it was to discuss and find new ideas with you. To Carl Jansson, for his chill vibe, his eagerness to learn, and for always finding practical solutions to the challenges we face at work. To the other people at PAEC who brought positive energy to me during this project, thank you as well: Pak, Robert, Sandra, Swathy, Charlotta, and the M.Sc. students I had the privilege to supervise and learn from during this project: Gabriele, Aaron,

and Elin. To other colleagues at PAE, I want to thank Jonas Granestrand for always being open to deep discussions, about projects, or just life. Thank you for showing a way of working that looks for explanations, seeks informed decisions, and tackles knowledge with humility. Bright minds deserve to be noticed more. To Arun, Khyati, Paul, Michal, Shalabh, Nitin and Fredrik for the nice energy and the short discussions we have had.

In my new group, working on ICE control, I want to thank Magnus Jansson Edqvist for his support and expertise, which have helped me in this new path as a software developer. You are always open to helping, teaching, and supporting with great energy. I also want to thank the SCR team, Kurre, Erik, Disa, and Piyush, for all the support during this transition, and for all the expertise and knowledge you have shared that has permeated this project. Thank you for giving me a sense of belonging to a community where we can share ideas, show our frustrations, and get the support we need. To the rest of my new group, Athanasios, Volkan, Nirnay, Serhat, and Pooja, you help make daily life enjoyable and easier to handle. When challenges and tasks are tackled as a group, the experience becomes more gratifying. I am also honoured to belong to a group that is open to new ideas, friendly, looking for the best solutions, and willing to learn and grow together as a team.

I want to give special thanks to Ola Stenlåås for the fruitful discussions, for your rigour in development and science, and for pushing for a way of working based on data and proper analysis. To Per Stålhammar, for the endless discussions about TWC, and for challenging us to deliver the best possible product. I believe technical discussions, even disagreements, handled respectfully are among the best ways to create ideas and synergies, and to train our curiosity.

My time at Chalmers was not long, but I want to acknowledge the people who made me feel I belonged: Manuela, Feryal, Rick, Michael, Leandro, Lucas, Aqsa, and Joonsoo. I enjoyed all the time, discussions, and activities we shared, and I wish you a lot of success in your endeavours. I also want to thank Jieling Shao for the collaboration during the HEER project, for our fruitful discussions, and for the knowledge we shared. Your contribution helped us better understand how to close the gaps between experiments and modelling for application.

At Chalmers, I had the opportunity to have amazing scientific discussions with Prof. Henrik Grönbeck, Ronnie Andersson, and Per-Anders Carlsson. All these discussions shaped the output of this research and helped us reflect

on the complexity we were facing. Also, though not directly related to this project, but to the ageing campaigns done at Chalmers, I want to extend my thanks to Lasse Urholm and Lennart Norberg for their flexibility and support in running new experiments that have been valuable for the organisation and for the projects I participated in.

Now I want to thank the friends I made in my life during my accidental journey to Sweden. In Stockholm, to my Swedish Institute peers: Krisna, Ati, Alberto, and Jairo. Time has gone so fast, but I am grateful we still find time to support each other. To Alejandro, Oscar, and Sebastian, for making life easier with your company, anecdotes, and philosophy. To Ramiar and Camila, for giving valuable feedback on my work and life choices, and for giving me a space where we could talk, have fun, and grow.

To my family, my parents, Antonio and Yolanda, thank you for your unconditional support in all my decisions; for being my foundation as a person; and for all the energy and effort you both put in so we could have the opportunities we have had in life. Everything I am, and everything I have done, has been thanks to the way you raised me. To my brothers, Daniel, Mario, and Santiago, thank you for sharing life with me, for supporting me, and for showing me that thinking out of the box is often necessary to find the answers we are looking for. Thank you for teaching me different ways to view the world, and to be more empathetic. Thank you for showing me what a real family should be: supportive, loving, and present. You are always on my mind.

Finally, I want to thank Joanna, and the happy coincidences that let our paths cross. Thank you for your unconditional support, energy, and motivation. I cannot describe how thankful and happy I am to have you in my life, and to see how sharing life with the person you love can give you a breath of fresh air, energy, and a perspective that permeates everything you do. Having a safe place where you can be yourself, where you get the support and encouragement you need, and at the same time feel the excitement of living and the expectations for a bright future, is something I am grateful for, and happily surprised to have found with you. I love you, and I wish you happiness, peace, and an amazing future. Even better if it is with me. Also, I want to thank Gustaw for his imagination, his energy, and his questions, those that remind us why we should listen to children more often if we want to see the world in a different, but positive, way. I am sure life will be full of success and great moments for you.

Nomenclature

Abbreviations

AI	Artificial Intelligence
AIC	Akaike Information Criterion
ASC	Ammonia Slip Catalyst
CCU	Carbon Capture and Utilization
CPSI	Cells Per Square Inch
CSTR	Continuously Stirred Tank Reactor
DFT	Density-Functional Theory
DOC	Diesel Oxidation Catalyst
DPF	Diesel Particle Filter
EATS	Exhaust Aftertreatment System
EV	Electric Vehicles
FTIR	Fourier Transform Infrared Spectrometer
GA	Genetic Algorithm
GHG	Greenhouse Gases
GDP	Gross Domestic Product
ICE	Internal Combustion Engine
ISC	In-service Conformity
LCA	Life Cycle Assessment
LH	Langmuir-Hinshelwood
LNG	Liquefied Natural Gas
MFC	Mass Flow Controller
OBD	On-board Diagnostic
OBM	On-board Monitoring
ODE	Ordinary Differential Equation
OSPA	Oxford Scenario Planning Approach
PEMS	Portable Emissions Measurement System
PGM	Precious Group Metal
PM	Particle Matter
RDE	Real Drive Emissions
RTD	Residence Time Distribution
SCM	Single Channel Catalyst Model
SCR	Selective Catalytic Reduction
TWC	Three-way Catalyst

WHO	World Health Organization

Variables

A	Pre-exponential factor, unit depends on reaction order
A	Area, m^2
a_p	Washcoat surface area per volume of catalyst, m^2/m^3
C	Surface concentration, mol/m^3
$\overline{c}$	Bulk gas concentration, mol/m^3
D	Molecular diffusivity, $m^2/$ s
D_{eff}	Effective diffusivity, m^2/s
D_K	Knudsen diffusivity, m^2/s
Da	Damkohler number, –
d_a	Washcoat thickness, m
d_o	Open channel width, m
E_a	Activation energy, J/mol
F	Gas molar flow, mol/s
k_a	Adsorption rate constant, $m^3/(kg.s)$
k_d	Desorption rate constant, $mol/(kg.s)$
k_m	Mass transfer coefficient, m/s
m_s	Total mass of catalyst, kg
N	Total amount of adsorption sites, mol/kg
N	Number of sample points, –
N_{WP}	Weisz-Prater criterion, –
P	Pressure, Pa
q	Washcoat conductive flux, $J/(s.m^2)$
R	Gas constant, $R = 8.3145$ J/(mol.K)
r	Reaction rate, unit depends on reaction
r^{obs}	Apparent reaction rate, $mol/(m^3.s)$
S	Selectivity, –
Sh	Sherwood number, –
t	Time, s
T	Temperature, K
v	Superficial gas flow velocity, m/s
w	Washcoat mass for each discretization volume, kg/m^3
X	Conversion, –
Y	Yield, –

y_{exp}	Experimental mole fraction, –
y_{mod}	Modelled mole fraction, –
z	Axial coordinate, m
z_{Sh}	Sherwood dimensionless axial coordinate, –

Subscripts

i	Gas species
j	Site index
k	Catalyst axial section
m	Reaction
n	Washcoat layer

Greek letters

$\alpha, \beta, \delta, \gamma$	Reaction orders, –
ΔH	Change of Enthalpy, J/mol
ΔS	Change of Entropy, J/(mol.K)
ϵ	Washcoat porosity, –
ω	Weighting function, –
φ	Micropore mass transfer coefficient, m/s
σ^2	Variance, –
τ	Washcoat tortuosity, –
Γ	Mass transfer coefficient, m/s
θ	Adsorbed species coverage, –

Contents

Part I

Overview

CHAPTER 1

Introduction

"Anyone who believes that growth can go on forever in a finite world is either a madman or an economist"

— Kenneth Boulding

1.1 Sustainability in a World Built for Us

Sustainable development is broadly defined as “development that meets the needs of the present without compromising the ability of future generations to meet their own needs" [1]. This definition is normative and subjective, and it is also anthropocentric. It frames the planet as a supporting system with its value mainly linked to human needs, now and in the future. Within this framework, promoted by companies, states, and citizens, the question becomes: how far should we create new technology and reorganize our societies so that planet Earth continues providing services that allow humanity to flourish?

Today, this anthropocentric view is reinforced by the term "ecosystem services”. This term suggests that ecosystems provide provisioning, regulating, and cultural “services” that contribute to human well-being (Fig. 1.1) [2].

The term makes our strong dependence on nature clear, and it influences policies and economic thinking. However, it is also widely criticized. It defines and classifies the environment mainly in terms of benefits for people or the economy, which can promote an exploitative human–nature relationship. It also supports a view of nature as a commodity that can be traded through markets or politics. One advantage of this view is that it allows us to quantify parts of nature's value and to define limits.

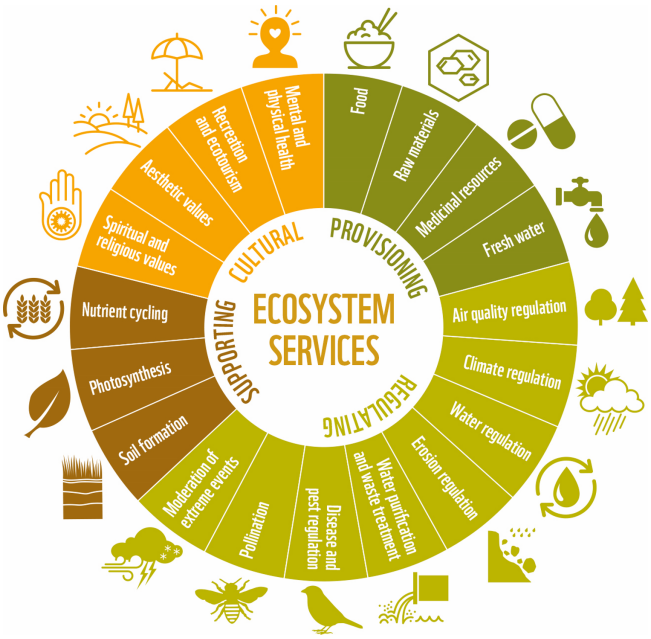

Figure 1.1: Ecosystem services. Taken from [3]

.

Based on those limits, there is evidence that the planet is already operating beyond several planetary boundaries (Fig. 1.2). These boundaries were proposed as limits that define a safe operating space for human development. They include climate change, biodiversity loss, freshwater systems, critical resources, and more [4]. This version of sustainability can be conflicting because it assumes that natural capital can be replaced by technology and other forms of capital. This makes it easier to maintain current economic systems and

consumption levels, while shifting environmental burdens across time and space. As a result, a world "built for us" often does not account for the risks and costs placed on non-human entities and on future generations through our current, and often controversial, concept of sustainability.

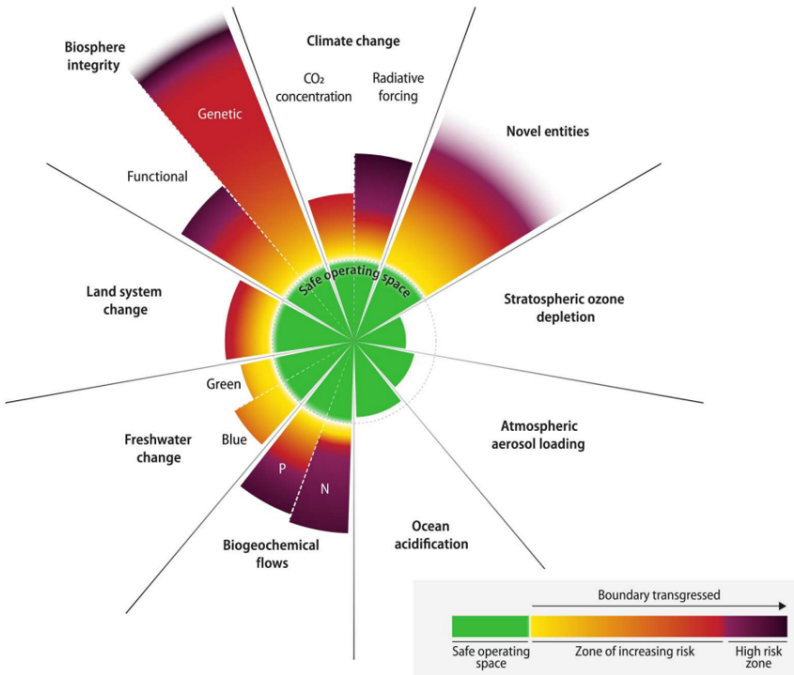

Figure 1.2: Planetary boundaries assessment for year 2023. Taken from [4]

.

The transportation sector is a clear example of these tensions. Transport on land, sea, and air still depends heavily on combustion engines running on fossil fuels, and it accounts for more than one third of CO_2 emissions [5], [6]. Beyond CO_2, transport infrastructure affects land use, generates noise and air pollution, and supports growing demand for goods and services. Transport planning has often focused on minimizing cost while accommodating demand coming from other sectors. The sustainable mobility paradigm challenges this by calling for demand management, better resource use, and technological measures [7].

Unfortunately, technological measures often focus narrowly on emissions, which can neglect other ecosystem services affected by new technologies and infrastructure. Policy efforts, such as the Euro emission standards, have successfully reduced tailpipe emissions and have supported decarbonization by improving vehicle efficiency. However, focusing mainly on air quality and climate change can hide other impacts: soil and water quality, biodiversity, landscape fragmentation, resource extraction, and the social distribution of environmental burdens and benefits.

Electric vehicles (EVs) show both the potential and the limits of this dominant approach. Life cycle assessments (LCA) often find that EVs can reduce greenhouse gas emissions compared to fossil-fuel combustion engines, especially when the electricity grid is low-carbon [8]. However, results are highly sensitive to the grid mix, driving patterns, and vehicle size. EVs also create new impacts through mining, processing, and refining critical minerals such as lithium, cobalt, nickel, and rare earth elements, which are often located in ecologically fragile and socially vulnerable regions [9]. From an environmental justice perspective, safeguards are needed because the EV transition can reproduce or deepen existing injustices along global supply chains and within cities, where access to clean mobility options is highly unequal [10].

With new technologies, rebound and spillover effects can also occur. Lower operating costs, higher performance, and "zero emission" branding can encourage more travel, second-car ownership, and shifts toward larger vehicles, reducing environmental gains [11]. System dynamics models suggest that rebound effects from electric cars can change consumption patterns in ways that offset life-cycle emission reductions and increase other burdens, such as critical resource use [12]. From an ecosystem services perspective, we may improve certain services (urban air quality, climate regulation) while worsening others (water availability, habitat quality, cultural landscapes in mining regions). These trade-offs are rarely visible when sustainability is framed only at the vehicle tailpipe.

Given the complexity of the transportation sector and its interaction with society, it is clear that there is no single technological pathway toward "sustainable transportation." The choice and mix of technologies, infrastructure, and policies reflect societal and ethical values, for example, how we prioritize mobility, which ecosystems or resources we are willing to sacrifice, and how we distribute risks between places and generations. In this context, the role of

researchers is not to prescribe a universal and "rigorous" road map (which is often biased), but to provide robust facts, models, tools, and scenario analyses. These can make trade-offs explicit and allow societies to make informed and democratic choices.

At the same time, there is a challenge in implementing solutions quickly. Even under ambitious decarbonization scenarios, internal combustion engines are expected to remain a significant part of the global vehicle fleet for decades, especially in heavy-duty transport, marine, and aviation, and in regions with limited infrastructure and capital where climate policies move slowly. In many countries, second-hand ICE vehicles will continue circulating long after new sales and regulations shift. Ignoring the current and future ICE vehicle stock in the name of sustainability is unrealistic, and it would miss opportunities to reduce emissions in the near term.

This uncertainty and the diversity of pathways call for developing and improving all available technologies. For the internal combustion engine platform, this involves integrating advanced mitigation and remediation strategies. This can be done through efficiency improvements, low-carbon fuels, and sophisticated after-treatment systems to reduce the overall environmental footprint and to remediate some of the damage already done. These actions can buy time while society negotiates deeper changes in economic and social structures and while more evidence is developed. Among these strategies, emission after-treatment remains one of the key pillars for reducing local environmental and health impacts.

Modern exhaust after-treatment systems combine several catalytic functions, such as three-way catalysts, diesel particulate filters, and selective catalytic reduction (SCR), in increasingly complex architectures. Their task is to transform harmful species (NO_x, CO, hydrocarbons, particulate matter) into lower-impact products (CO_2, H_2O, N_2) under highly transient operating conditions. As emission limits become stricter, engines are pushed toward more efficient combustion modes that often increase raw NO_x emissions, and the demands on catalytic systems become more intense. SCR catalysts have become a key technology for NO_x reduction. Recent developments focus on high conversion across wider temperature ranges, improved durability, reduced secondary emissions such as N_2O, and better integration with advanced control and diagnostic systems [13], [14].

In this context, detailed mechanistic models are essential for a more honest

sustainability strategy in a world that is still built around combustion engines. Mechanistic models enable more accurate impact assessment, support emission reporting (through on-board monitoring systems), and can improve control strategies by reacting to the system's dynamic nature. This helps operate the system closer to its best performance point. By enabling optimization of after-treatment systems under real driving conditions, these models can reduce the remaining environmental burden of combustion engines and make socio-technical transitions broader. They can support alternative fuels, different engine platforms, and solutions that require less new infrastructure, options that may fit different societies, especially those with economic and social constraints in the transition toward a more equal and sustainable transportation sector.

1.2 The Promise of AI for Catalyst Modelling

Rapid digitalisation in the automotive industry has popularised concepts such as digital twins and artificial intelligence (AI) as universal solutions for system design, optimisation, and control. It is increasingly common to encounter managerial expectations that a "digital twin" of the powertrain, especially the emissions aftertreatment system, can be built quickly once enough data is available, and that machine learning will soon replace kinetic modelling and mechanistic models. Current literature on digital twins, machine learning in chemical engineering, and catalyst modelling shows that a naive deployment of AI, without clear goals and strong domain guidance, tends to add noise and complexity rather than deliver robust solutions and insight [15], [16].

Recent definitions of digital twins clarify that they are not simply detailed simulation models, but an automation strategy that connects a physical system to an adaptive, real-time simulation framework through bidirectional communication [17]. A digital twin comprises a physical system, a model, and a data infrastructure that synchronises the two. This definition has two important consequences. First, without feedback from the model to the system, the "digital twin" is only a digital model. Second, a digital twin is only as good as its components: if mechanistic principles, such as mass and energy balances, are poorly captured, real-time coordination will only propagate innacurate predictions [18].

There are also recurring misconceptions in industry expectations. A digital

twin industry report by Hexagon AB [19] points to "digital twins replace human expertise" as the biggest misconception, since digital twins are meant to enhance human expertise rather than replace it. In catalyst modelling, expert insight is still required to interpret outputs, check if results are physically reasonable, and design experiments that generate useful data [20], [21].

For emissions aftertreatment models, the physics includes compressible and transient flow, strong temperature gradients, multicomponent transport and diffusion in the washcoat, and highly non-linear reaction kinetics. Key outputs (such as tailpipe NO_x, NH_3 slip, and pressure drop) depend on internal states that are not fully measured in practice. This is why aftertreatment modelling requires reliable reduced-order models, accurate parameter estimation, and strategies to handle uncertainty. A digital twin based on generic AI cannot capture this physics from data patterns alone, especially during transients and when operating conditions change.

In aftertreatment modelling, another common over-optimism is the assumption that machine learning methods developed for large-scale data (images, language, advertising, internet platforms) can be transferred directly to catalytic systems [22], [23]. In chemical engineering and catalyst modelling, Thebelt et al. [24] identify four problematic data regimes: high-variance, low-volume data; low-variance, high-volume data; noisy, corrupt, or missing data; and data limited by physical constraints. Experiments in emissions aftertreatment mostly fall in the first and third regimes, since experiments are expensive, the design space is high-dimensional, and many variables are hard to measure or control. Therefore, a general machine learning framework often struggles when it is applied directly to aftertreatment systems. Hybrid workflows (ML + mechanistic) offer a more systematic alternative to the simplistic narrative that "AI will learn kinetics" and remove the need for physics-based models.

From a more abstract perspective, the "no free lunch" (NFL) theorems for optimisation by Wolpert and Macready [25] formalise the intuition that there is no single best black-box method for all scenarios. Averaged over all possible objective functions, no method is best. A model can outperform others in a given case only by exploiting structure that matches the real system, which usually requires expert knowledge.

For catalyst models, that structure is the physics encoded in conservation equations (mass and energy), transport mechanisms, and reaction kinetics. Believing that a black-box model will discover this intrinsic structure from a

small, noisy, and limited dataset is implicitly assuming a "free lunch": that the model will encode prior knowledge without being given it. The NFL message is not that AI is useless, but that AI needs proper frameworks and governance, with constraints aligned to system physics and reliable parameter estimation for conservation equations and kinetics [17].

Mechanistic models differ from machine-learning models because they are built from our current understanding of the system. They are ruled by conservation of mass and energy, transport processes, and reaction schemes. The structure of the model is driven by physics rather than only by data patterns [23], [26].

Mechanistic models provide insight. Comparing predictions with experiments or real data helps us understand the influence of each parameter, identify where assumptions fail, and refine understanding of the system. They also have stronger validity and can be extrapolated because they are grounded in physical laws. If the main assumptions hold, a mechanistic model of an emissions aftertreatment system can operate across many conditions and support forecasting for new scenarios.

Mechanistic models also give control and transparency because the parameters have clear meaning and relate to catalyst properties, geometry, and operating conditions. People in the field can understand the equations, verify that predictions respect conservation laws, and adjust the model as new knowledge becomes available. These models guide the design of experiments to extract the highest amount of information from the experiment. They are also scalable: a model developed on a gas-flow reactor can be extended to engine test-bench experiments or engine calibration environments with lower experimental effort, because the physics framework remains the same. In this sense, the most robust route to a digital twin for aftertreatment is usually a mechanistic (or hybrid) core supported by data infrastructure, where AI is used as an enabler, not as a replacement for physics (Fig. 1.3).

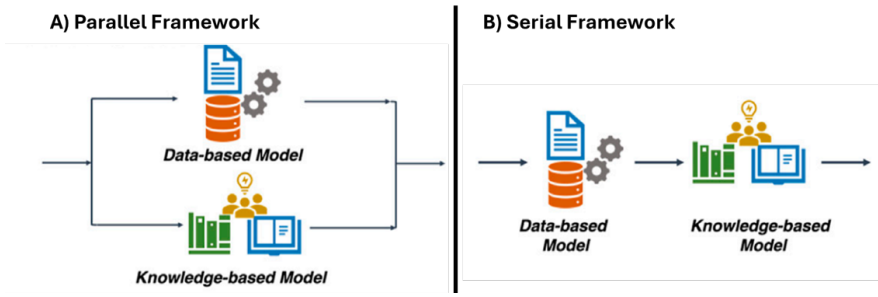

Figure 1.3: Hybrid modelling frameworks with mechanistic and data-driven methods [27].

1.3 Thesis Outline

This thesis presents modelling frameworks for SCR catalysts, developed with the goal of gaining new understanding of the systems studied. In this thesis, a modelling framework includes: the design of experiments to collect the right data, data processing to meet model input requirements, parameter estimation using tailored optimization strategies, and validation schemes that test model quality. Once a model is validated, it can be used to answer the specific questions it was designed for.

The thesis covers all key steps needed to build mechanistic models, and explains why these steps matter from a system perspective. Emission after-treatment models can support the transition to a more sustainable transportation sector, where combustion engines are expected to remain important in the near and mid-term. Mechanistic models are also valuable because they can increase system understanding and provide a structured base for hybrid approaches, where machine learning is used together with physical modelling.

In Background (Chapter 2), the thesis describes the complexity of the transportation sector and the uncertainties for the future. It explains why emission after-treatment models will stay relevant for design, optimization, and control, especially as new fuels, new legislation, and new driving patterns increase the need for accuracy and deeper understanding of reaction mechanisms. This includes side emissions and aging effects. The chapter also presents system architectures for lean-burn engines using diesel or hydrogen, and summarizes the current knowledge on NH_3-SCR catalysts (especially vanadium-based)

and H_2-SCR catalysts (especially Pd-based).

The experimental framework (Chapter 3) describes the experimental setup used in this thesis: a gas flow reactor designed to measure catalyst activity under controlled conditions of flow, temperature, and gas composition. Additional methods are used to support model development. The design of experiments follows an iterative process. A screening phase, based on prior knowledge, is used to understand how key variables affect the response. Based on the screening results and parameter sensitivity, a refined experimental region is defined and the final protocol is formalized. The chapter also presents data-processing strategies to identify experimental artifacts and to separate reactor and measurement effects from the catalyst behavior of interest (**Papers A and C**).

The modelling framework (Chapter 4) uses a single-channel monolith model (SCM) as a basis, and develops different strategies depending on the modelling objective. Based on these objectives, tailor-made models are developed (**Papers B, C, and D**). A key point in this thesis is that the model structure is treated as a design choice and a central part of model discrimination. The thesis shows that a data-driven approach, where many candidate models can be tested, is enabled by first calibrating thermodynamically consistent steady-state models. This step adds physical meaning, reduces parameter correlation, and makes parameter estimation for the dynamic model more robust (**Paper B**). Mass transfer is studied from multiple perspectives (**Papers C and D**), including evidence of non-uniform washcoat porous structure, and the thesis proposes practical strategies for model validation and model quality assessment.

Finally, the thesis presents conclusions and an outlook on the need for systematic frameworks to develop mechanistic models where quality, traceability, and validity are transparent to users and to the scientific community. It also highlights the need to improve current models through a more detailed description of mass transfer. This is important because stricter legislation increases the demand for reliable and predictive models. The thesis also discusses how a data-driven workflow can support more advanced modelling strategies, including hybrid approaches with machine learning.

1.4 Thesis Objective

The objective of this thesis is to improve modelling approaches for catalysts used in emission after-treatment systems, with focus on vanadium-based NH_3-SCR and Pd-based H_2-SCR catalysts for lean-burn engines. The work targets both mechanistic understanding and model quality, so that the models can be used for analysis, design, and control. Three main objectives are defined.

SCR Catalyst knowledge

Generate new insight through model development and simulation.

For a vanadium-based NH_3-SCR catalyst, the work develops an NH_3 adsorption mechanism with multiple adsorption sites, where adsorption and release dynamics depend on water concentration and catalyst state. Steady-state parameters are linked to thermodynamic properties, which gives physical meaning and improves parameter validity. Based on this adsorption model, mass transfer effects are studied and included in a more detailed way by representing the non-uniform nature of the washcoat.

For a Pd-based H_2-SCR catalyst, different supports are studied. A power-law kinetic model coupled with mass transfer is used to estimate gas concentration profiles and to evaluate how H_2 availability changes through the catalyst, especially under mass transfer limitations that affect the SCR reaction.

Data-driven Modelling Framework

Develop a systematic workflow from experiments to validated models.

A systematic framework is developed to maximize the information extracted from experimental data while reducing overfitting and high parameter correlation. The framework is based on: building and calibrating steady-state models to propose candidate model structures for later model discrimination, characterizing the experimental setup to remove reactor and measurement effects and separate them from catalyst behavior, and an iterative workflow where quality indicators are monitored and analyzed to improve experiment design and parameter estimation.

Mass Transfer Relevance

Improve model validity in the transition regime between kinetics and diffusion.

Catalysts in emission after-treatment often operate in a transition regime where both reaction kinetics and mass transfer affect the measured response. In this regime, kinetic and mass transfer parameters can become strongly correlated, which makes parameter estimation and identification of a global optimum difficult. This thesis proposes two main approaches to improve model validity.

Firstly, by calibrating parameters in steady state, it becomes possible to use a more detailed mass transfer description in the dynamic model. This increases insight into how the porous structure affects NH_3 adsorption dynamics. Secondly, by using dimensionless criteria, Damköhler and Weisz–Prater numbers, it is possible to evaluate which mechanism is relevant based on heuristics if the system is in kinetic, mixed, or mass transfer limited regime. This increase the confidence of the parameters and reduce their correlation.

CHAPTER 2

Background

"We have created a civilization that runs on illusions about energy and resources"

— Vaclav Simil

2.1 The Transportation Sector Today

The transportation sector is the backbone of modern society: it enables the mobility of people and the circulation of goods through supply chains at local, regional, and global scales. Materials and industries are located in different places; therefore, the performance of the transportation sector shapes the current economy and its resilience. In terms of scale, the transportation sector accounts for around 30% of global energy demand, with road transport responsible for almost 90% of this total. Regarding CO_2 emissions, transport produces around 9.6 $GtCO_2$-eq per year, corresponding to about 20% of global energy-related CO_2 emissions. Despite ongoing decarbonization efforts, the sector remains highly dependent on fossil fuels, which account for around 90% of its energy use, followed by biofuels and natural gas (around 4%), and

electricity (around 2%) [28], [29], [30].

Heavy-duty transport, including buses and trucks, plays a critical role in society by enabling the movement of people and goods and by shaping the structure of cities and supply chains. However, its environmental impact is also significant. Although buses and trucks represent only around 10% of the total vehicle fleet on roads, they are responsible for approximately 35% of transport-related CO_2 emissions. Freight transport, mainly trucks, is the largest single source of diesel demand, consuming more than half of global diesel use. The global energy consumption for the road transportation sector in 2015 is shown in Fig. 2.1 [29], [31], [32].

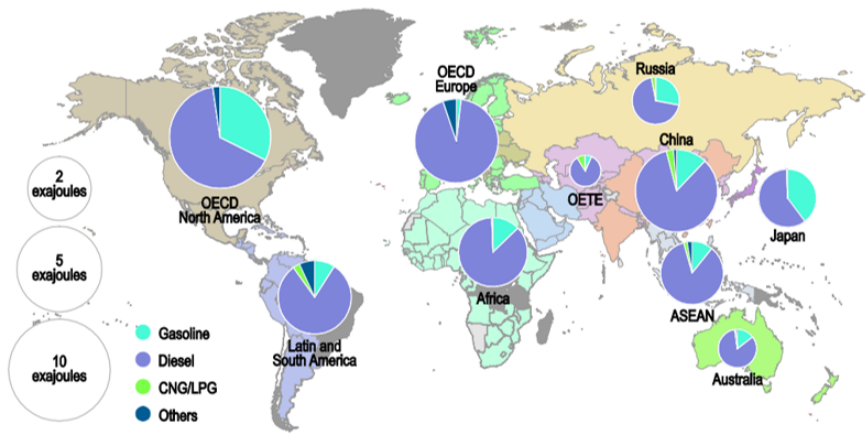

Figure 2.1: Energy consumption for the road transportation sector for 2015. ASEAN: Association of Southeast Asian Nations. OECD: Organization for Economic Cooperation and Development. OETE: Other European Transition Economies. Taken from [31].

The global heavy-duty vehicle fleet is difficult to quantify precisely, but studies suggest that the number of medium- and heavy-duty vehicles exceeded 180 million in 2023. This sector is growing at around 3% per year, with the largest shares in the United States, China, and Europe. In Europe alone, approximately 6 million trucks and 700,000 buses were registered in 2023. The scale of the heavy-duty sector highlights its strong influence on public transportation and logistics [31], [32], [33], [34].

However, the environmental impact of the heavy-duty segment depends not

only on its size, but also on the age and quality of the fleet. In the European Union, the average age of a truck is around 14 years, with older fleets, 20 years or more, common in Southern and Eastern Europe. In developing and low-income countries in Asia, Africa, and South America, fleet ages can exceed 25 years due to limited legislation, lack of financial support, and the absence of integrated sustainable transition programs. This long vehicle lifetime is reinforced by the second-hand market, where used trucks from Europe and the United States are exported once they no longer comply with emission regulations. While this practice improves affordability and access to vehicles, it also perpetuates the use of outdated emission control technologies [34], [35].

Within the transportation sector, air pollution is considered one of the most severe environmental impacts, alongside climate change and resource depletion. The World Health Organization (WHO) estimates that around 6.5 million premature deaths per year are linked to air pollution [36]. Road transport is a major source of nitrogen oxides (NO_x), contributing approximately 30–40% of total anthropogenic NO_x emissions worldwide [30], [37]. Heavy-duty vehicles account for more than one-third of transport-related NO_x emissions and about half of particulate matter emissions [6], [37].

At the same time, stricter emission standards, such as Euro 7 and EPA 27, and the introduction of modern exhaust after-treatment systems have reduced NO_x and particulate emissions from heavy-duty vehicles by more than 90% compared to vehicles from the early 2000s (Euro III–IV) [31], [36], [38]. The trend in emissions reduction over the last years for NOx and particle matter is shown in Fig. 2.2 as economic growth given by the increase on Gross Domestic Product (GDP). This highlights the key role of regulation in improving air quality, as these technologies increase vehicle cost and complexity and are therefore largely driven by legislation rather than market demand.

Over the last decade, the transportation sector has been characterized by both growth and vulnerability to disruptions. The COVID-19 pandemic revealed this vulnerability, as aviation and public transport came to a near halt, while global freight demand increased by around 25%, driven by rapid growth in e-commerce and last-mile deliveries. As restrictions were lifted, the sector recovered sharply, with energy demand increasing by around 5% per year [31], [33].

From a decarbonization perspective, the heavy-duty segment is considered

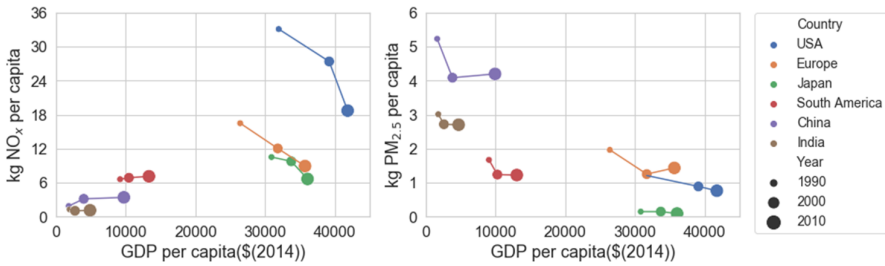

Figure 2.2: Emissions development at different countries/regions from different years or Gross domestic product (GDP) as an indicator of economic growth [36], [38]

.

"hard to abate," as it still relies on fossil fuels for around 90% of its energy demand. This is mainly due to requirements for long driving range, high payloads, and high vehicle utilization, which favor high-energy-density fuels supported by established refueling infrastructure. Even in scenarios with strict climate and energy policies, the heavy-duty segment is expected to account for around 40% of global oil demand and approximately 15% of transport-related CO_2 emissions by 2050 [28], [39], [40].

Decarbonization strategies are emerging more rapidly in segments that are concentrated and predictable, such as city buses and last-mile distribution. In 2021, the global electric bus fleet reached around 1 million vehicles, representing approximately 4% of the total bus fleet, while electric medium- and heavy-duty trucks reached around 66,000 units, or about 0.1% of the global fleet, with China as the dominant market. Sales have grown rapidly: in 2022, around 66,000 electric buses and 60,000 electric medium- and heavy-duty trucks were sold worldwide, with China accounting for around 70% of global sales. These trends suggest that electrification is a highly suitable solution for buses and distribution hubs, while long-haul freight will likely require a mix of solutions, including biofuels, hydrogen, e-fuels, and efficiency improvements [31], [34], [41], [42].

However, electrification requires dedicated infrastructure and can introduce new sustainability challenges. Fast charging for heavy-duty vehicles requires very high power levels, which can create sharp local peaks in electricity demand. This needs substantial upgrades to electricity infrastructure,

particularly in distribution networks, transformers, and generation capacity. Such investments are time-intensive and may take between 5 and 15 years to implement, but they are essential to avoid high electricity costs and grid reliability risks [30], [31], [41].

Hydrogen presents a different set of challenges. The cost of green hydrogen remains several times higher than that of fossil fuels and is highly dependent on electricity prices. In addition, hydrogen infrastructure is expected to be costly, as components such as compressors and electrolyzers are unlikely to experience rapid cost reductions and are often considered commodity technologies [43]. As an example, Fig. 2.3 presents a Life cycle assessment (LCA) for a 40-ton truck, using different fuels (Fig. 2.3A), and the sensitivity on different diesel types (Fig. 2.3B). This figure highlights the high sensitivity of GHG emissions, based on the fuel source, especially the grid mix and diesel production [44].

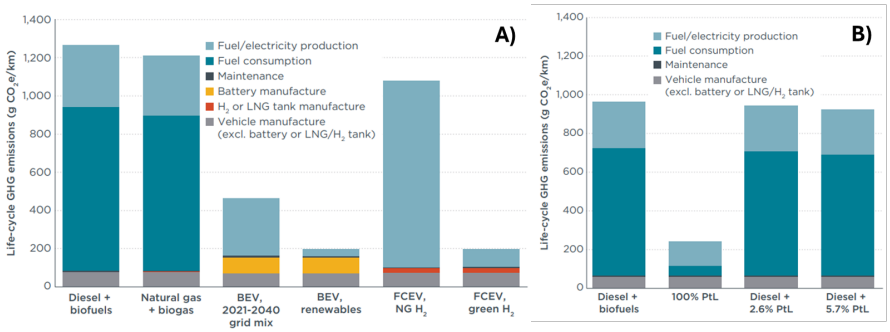

Figure 2.3: LCA analysis for a 40-ton truck for 2021. A) Based on fuel. B) Sensitivity analysis based on diesel type. PtL: Pure renewable power to Liquid. Taken from [44]

Both electrification and hydrogen technologies rely on critical minerals such as lithium, nickel, cobalt, and copper, whose production is concentrated in a small number of countries, sometimes affected by political instability or conflict. This concentration increases geopolitical risks and tensions. These pressures are further intensified by competition for resources driven by the rapid expansion of data centers supporting the AI revolution, which is itself a key pillar of modern society and also highly dependent on electricity and critical minerals [28], [43], [45].

Beyond the COVID-19 pandemic, several other disruptions have affected the transportation sector. Russia's full-scale invasion of Ukraine in 2022 triggered a global energy crisis, with oil prices briefly exceeding 100 US$ per barrel and commodity prices increasing by around 40–50%, driven by higher energy costs and risk premiums. Additional disruptions include maritime events such as the grounding of the M/S Ever Given in the Suez Canal in 2021 and the prolonged disruptions in the Panama Canal during 2023–2024. These events increase fuel consumption, CO_2 emissions, and system inefficiencies [6], [28], [39].

This broader geopolitical instability has redirected investments away from sustainable transitions toward defense and short-term security priorities. At the same time, international cooperation and financial support for developing and low-income countries have declined. Major oil and energy companies currently invest only around 5% of their capital in clean energy initiatives [30], [42]. As a result, long-term sustainability policies are increasingly replaced by short-term responses to security concerns. This shift poses a major challenge for developing countries, where emissions are growing rapidly. Delayed investment in low-carbon infrastructure risks locking these regions into affordable but volatile fossil-based systems, while developed countries move toward decarbonized transport. This divergence may further widen global inequalities during the energy transition.

2.2 Future transportation Pathways

Thinking about the future, especially a complicated future that involves society and the transport sector, comes with a lot of uncertainty. Relying on a single future scenario can lead to the wrong conclusions, which may result in poor investments and policies. The future needs to be reviewed regularly, and assumptions should stay flexible as our view of the world changes. For this kind of analysis, the Oxford Scenario Planning Approach (OSPA) is used to define multiple futures under deep uncertainty. This method is suitable for sectors characterised by turbulence, uncertainty, novelty, and ambiguity, such as transport [46], [47].

OSPA offers a strategic reframing rather than a forecast. It develops plausible but unfamiliar futures that are internally coherent for the sector. In a highly uncertain future, the past is not a reliable guide, so a flexible sense of the future

is needed. The OSPA method is iterative and involves framing, reframing, and re-perception of the scenario. In the framing step, boundaries and assumptions are set to make sense of the scenario. In the reframing step, the original scenario is challenged and the assumptions are changed. In the re-perception step, the updated scenario is examined to identify new threats and opportunities. The iterative nature of the OSPA method is described in Fig. 2.4 [46], [47].

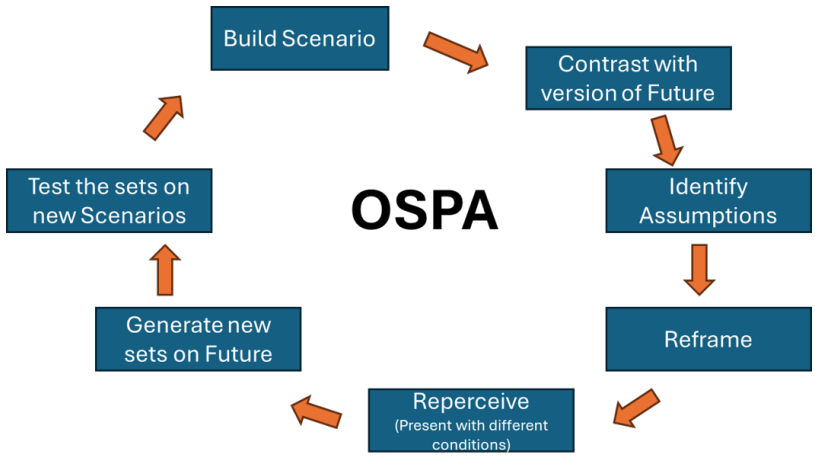

Figure 2.4: OSPA Methodology [46].

The OSPA method treats the future as a form of fiction: a strong narrative grounded in multidisciplinary research that helps us improve present choices. Usually, two or more scenarios are defined, often with contrasting outcomes. Companies in the transport and energy sectors use scenarios to guide their strategy. These companies have a strong influence on society and can shape policies, investments, and technological change [42], [48]. Their scenarios are plausible outlooks on how society and markets could develop. In the transport sector, based on the current state of society, the truck manufacturer Scania considers the following drivers: a more regionalised world, increasing digitalisation, climate change, and resource constraints [48].

In addition, uncertainties that can influence the future are defined in six main areas: geopolitics, climate change, the economy, the energy transition, society, and innovation. Some of the general trends for the future are described below based on the analysis of different reports and the current state of the

world [46], [48].

Natural Resources:

- Diversity loss is accelerated [29].
- Pandemics will be more often and severe [49].
- Loss of ice and warmer temperatures on polar regions will increase sea levels [2].
- Less opportunities to build climate change mitigation and remediation projects [28], [30].
- Increase of number and severity of climate disasters [4], [50].

Governance and Legislation:

- Accelerating speed for technological development [42].
- Increase on digitalization and access to data [28], [51].
- Environmental policy becomes a priority [29], [30].
- Policy and regulation do not synchronize and conflicts will arise [51].
- Fossil fuel system still a big player on policies, defending its role in the society [39], [42].
- More detailed and regulated world (Energy, pollution, AI, rights) [28].

Economic and Industrial System:

- Investment for climate change and clean energies is increased [30].
- Nations' growth rates will decline [39], [52], [53].
- The EU is expected to lose its global influence, in terms of GDP and technological capabilities [39], [54], [55], [56].
- Debt will be increased for most of the nations [51], [56], [57], [58].
- Resilience on supply chains will improve [28], [51].
- Unemployment will increase [56], [58], [59].

- Increase use of AI and robots to increase efficiency, production and fast development [41], [51].
- Business on circular economy are a reality and are scalable and part of the economy [5], [28].

Energy:

- Fossil energy production to remain stable [39], [42], [50].
- Low-carbon energy sources will increase [39], [42], [50].
- Demand for electricity will increase [28], [39], [42], [50].
- Green H_2 production will be limited by infrastructure [28], [39].
- Global battery production will reach over-capacity, consolidating main producers in China and restricted by environmental regulations [41], [45], [60], [61], [62].
- Electricity infrastructure to be expanded [39], [41].
- Hydrogen will play a role in different industries, but uncertainty remains in the transportation sector [28], [39], [43].

Transportation:

- Optimized transportation systems, with the creation of large-scale digital platforms for fleet control [31], [63].
- Autonomous vehicles on more complex applications [31], [41].
- Reduction of development cycles with the increase of software-define-vehicle (SDV) strategies [31], [48].
- Electrification will be conditioned by infrastructure but not supply [6], [41], [51].

Based on the future trends across these areas, the following scenarios are developed to be clearly different from each other.

Scenario 1: Coalition for Survival

Due to climate, political, and economic instability across major economies, several middle-income countries push for the creation of a global coalition to

address climate change and economic stability. In this scenario, heavy-duty vehicles move quickly away from diesel. Advanced biofuels and synthetic fuels are used selectively in segments that are hardest to electrify (aviation, maritime, and long-haul routes that are hard to decarbonise), while international climate finance is increasingly channelled into zero-emission buses, trucks, and public transport in rapidly growing cities. For long-haul transport, electric and hydrogen corridors expand.

Scenario 2: Competing Fortresses

Global polarisation intensifies as major economies adopt more confrontational trade and security postures [62], [64]. A shift toward selective alliance engagement and interstate conflict increases global fragmentation. Shared fiscal and policy mechanisms become difficult to sustain, and market distrust grows [65], [66]. This causes leading nations to pursue different solutions and pressures smaller countries to align with them, creating a few blocs that cooperate but distrust each other.

In this scenario, heavy-duty transport is still dominated by diesel, with some blocs deploying electric or Liquefied Natural Gas (LNG) trucks and buses. Divergent standards for charging, hydrogen refuelling, and digital platforms emerge, making cross-border operations costly and reducing economies of scale for cleaner technologies. In this world, transport decarbonisation is uneven and slower, with security-driven redundancy and regionalisation outweighing global efficiency gains.

Scenario 3: Patchwork Planet

In this scenario, states lose legitimacy, leading to a halt in policies and transitions. Coordination among allied countries is eroded due to budget disputes and lack of consensus [65], [66]. There is a shift from global institutions to local communities, cities, and companies that coordinate climate, technology, and trade progress. Production becomes local, modular, resilient, and self-sufficient.

As a consequence, leading cities and corporate logistics networks push hard for zero-emission mobility, with electric bus fleets and zero-emission urban freight zones. At the same time, many lagging regions with weak institutions continue to rely on ageing diesel trucks and buses and minimal

public transport, often buying second-hand vehicles from the leaders. The result is a very uneven transport landscape: pockets of clean, efficient electric freight and public transport coexist with large areas where oil dependency, local air pollution, and infrastructure gaps persist.

Fig. 2.5 presents the future scenarios based on the level of cooperation, high and low, and the governance level, global to local. Each scenario highlights the transportation mix based on energy use.

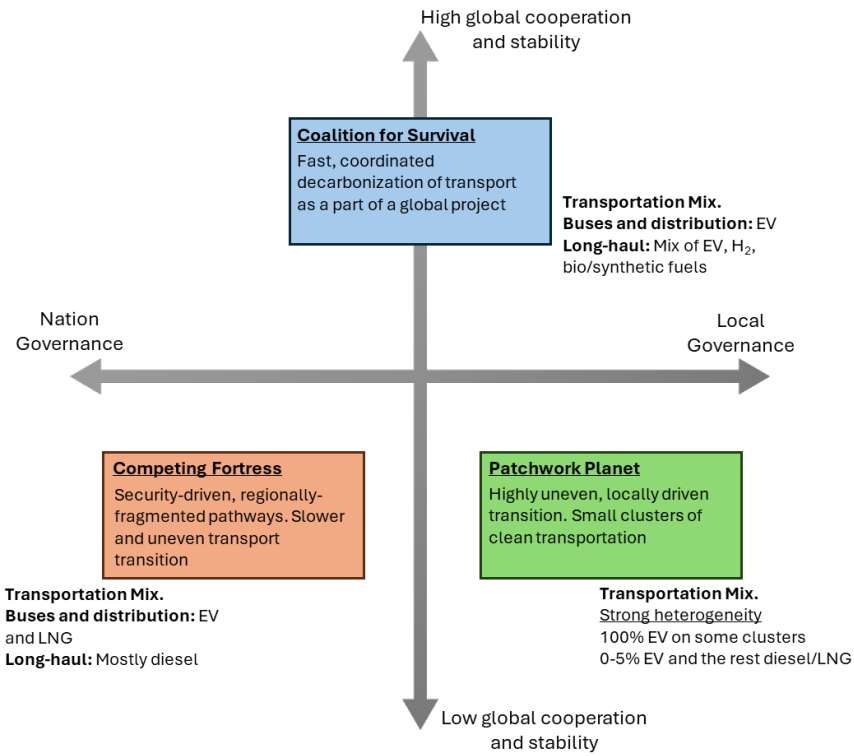

Figure 2.5: Future scenarios based on cooperation and governance level.

.

2.3 Evolving Emission Regulations: Challenges Ahead.

Emission legislation is defined by each region or country. The EU, China, and the USA are often used as references, since their legislation is also adopted or mirrored in regions such as India, Africa, and South America. In 2026, there is significant uncertainty because new legislation with tougher limits and monitoring is expected in the EU, USA, and China. In addition, emissions legislation is increasingly integrated with greenhouse gas (GHG) legislation to limit the amount of CO_2 a fleet can emit. This creates a strong push for higher fuel efficiency, electrification, and CO_2 offsetting through carbon capture and utilization (CCU) or e-fuels. Some organizations have suggested that this could be the last major emissions legislation before a full phase-out of the combustion engine in light-duty or heavy-duty vehicles [35], [67]. Emissions after-treatment systems are largely driven by legislation because they add cost to the vehicle. For a Euro III system, the cost was around US$400, while a Euro VI after-treatment system can cost around US$5,000 [33], [68].

The evolution of European legislation became noticeable in Euro V, where a stronger focus on combustion-related pollutants emerged, and the use of catalysts and engine strategies became necessary to meet the requirements. For a heavy-duty vehicle on an European Transient Cycle (ETC), the limits were 2.0 g/kWh for NO_x and 0.03 g/kWh for PM. Then, Euro VI represented a sharp step change, where particle number (PN; >23 nm) and NH_3 limits were introduced, together with a transient cycle more closely related to real operation. In a World Harmonized Transient Cycle (WHTC) cycle, the Euro VI limits are 0.46 g/kWh for NO_x, 0.01 g/kWh for PM, $6{\times}10^{11}$ #/kWh for PN, and 10 ppm for NH_3 [33], [68], [69].

The Euro 7 proposal makes the limits tighter and the scope broader. For NO_x, the limits are reduced to 0.2 g/kWh for both WHTC and World Harmonized Stationary Cycle (WHSC) tests. PM is proposed to be 0.008 g/kWh, while PN keeps the same limit value, but the monitored particle size is proposed to move from 23 nm down to 10 nm. NH_3 is moved to mass-based limits: 60 mg/kWh in lab tests and 85 mg/kWh in Real Driving Emission (RDE). In addition, a limit on N_2O is proposed at 200 mg/kWh in lab tests and 260 mg/kWh in RDE [33], [68], [70].

Besides the tighter limits, testing methodologies have also evolved across

legislations. In Euro V, only engine dynamometer testing was used, through the European Stationary Cycle (ESC)/ETC tests, together with a smoke test (ELR). There were basic durability and On-Board Diagnostics (OBD) requirements, but Portable Emissions Measurement System (PEMS) and in-service conformity were not applied systematically. In Euro VI, new test cycles were introduced (WHSC and WHTC), which are more representative of real engine operation. A brief description on the test cycles, WHSC and WHTC, is presented in Table 2.1. In-service conformity (ISC) using PEMS was introduced more systematically. Conformity factors above 1.0 are used to account for measurement variability, and PEMS evaluation typically considers operation above 10% of rated power [29], [68], [71].

World Harmonized stationary cycle (WHSC)	World Harmonized transient cycle (WHTC)
Sequence of steady-state engine modes with specific torque and speed. Duration: 1895s	World-wide real driving pattern for heavy-duty transport.
Loads vary between 25% to 100% rated (4 load points).	Duration: 1800s. It is divided into an urban (900s), rural (468s) and highway (432s) part.
Speeds vary between 25% to 75% rated (6 speed points).	

Table 2.1: Standard cycles on Euro VI for testing emission levels on engine bench [71], [72]

.

For Euro 7, the WHSC and WHTC cycles are still expected to be used, but the Real Driving Emissions (RDE) philosophy changes by applying on-road emission limits for most pollutants instead of using conformity factors. The minimum engine power threshold in PEMS is set to 6% to include more urban, low-load operating points. In the Euro 7 proposal, on-road limits are higher than lab limits by around 30% to reflect real-world variability [29], [35], [72].

Durability requirements have also increased to provide more value to customers (robustness) while meeting emissions targets. In Euro V, the durability requirement was 500,000 km or 7 years. In Euro VI, the requirement is 700,000 km or 7 years. For Euro 7, the proposal is 875,000 km or 10 years, with an extended range where emission limits are relaxed. Euro 7 also initiates the evaluation of emissions from brake and tire particulates [71], [72].

On-Board Diagnostic (OBD) requirements were introduced in Euro IV and

Euro V with an initial framework, and then improved in Euro VI. OBD focuses on component monitoring, but not necessarily on continuously meeting tailpipe emissions limits. Its goal is to monitor, diagnose, and notify when an essential component in the after-treatment system is not working properly, is tampered with, or is removed. In Euro V and Euro VI there is no continuous tailpipe emissions monitoring. In the Euro 7 proposal, On-Board Monitoring (OBM) is introduced and requires tailpipe monitoring of NO_x, PM, and NH_3. Emissions will be logged and levels above 2.5 times the legal limit can trigger warnings and inducements. OBM data could also be shared via the cloud for monitoring and fleet surveillance. This requires continuous emissions monitoring using sensors and models to identify deviations from healthy, normal system behavior [63], [68].

Legislation in the USA has followed a similar path compared to Europe, with parallel requirements regarding limits, tests, durability, and monitoring. However, some differences exist. In the USA, there is a more integrated focus on GHG emissions such as CO_2, CH_4, and N_2O (e.g., the EPA 2027 NO_x rule and HD GHG Phase 3). US durability requirements are strongly driven by warranty and compliance monitoring programs, which are extended in the EPA 2027 legislation. In this case, OBM is not added, but increased compliance requirements with PEMS and more component-driven OBD demands create a similar effect. US legislation also includes a special low-load cycle to reflect normal/idling conditions where NO_x control is challenging [73], [74], [75].

In China, China 6 has many similarities with Euro VI, with small differences in emission levels and test procedures. China 6 is the first legislation worldwide to introduce continuous OBM and reporting as an emissions surveillance tool for NO_x. For the future China 7 proposal, some similarities to Euro 7 and EPA 2027 are expected, since there is a common need to harmonize global legislation to benefit manufacturing. However, a stronger focus on low-load and cold-start emissions, and integration with CO_2/GHG management, is also expected. Among the main emissions legislations, China 7 is the least mature, and discussions between stakeholders are still ongoing [76], [77], [78].

Table 2.2 summarizes the main aspects for the Euro 7, EPA 27 and China 7 legislation.

	Euro 7 (EU)	EPA 2027 (US)	China 7 (CN)
Status	Final regulation	Diesel HD rule final	Draft, under development
HD start	HD types 2028; all HD 2029	MY 2027 engines/vehicles	Expected from 2027
Main NOx lab limit	0.20 g/kWh WHTC	0.035 g/bhp-hr FTP/SET	30–50% below China VI (TBD)
NH_3 regulation	Mass limit; 60 mg/kWh lab, 85 mg/kWh RDE	No explicit limit; controlled via SCR/OBD	New NH_3 controls
N_2O regulation	Mass limit; 0.20 g/kWh lab, 0.26 g/kWh RDE	0.10 g/hp-hr under GHG rules	Planned N_2O limit (TBD)
PEMS / on-road	RDE PEMS with Euro 7 limits (NO_x, PN10, NH_3, N_2O)	MAW-PEMS in-use NO_x (FTP/SET/LLC)	PEMS ISC strengthened from China VI
On-board monitoring	OBD + OBM + fuel/energy monitoring	Stronger HD OBD; no OBM	Remote OBD/telematics; expanded digital monitoring
Useful life	Up to ~875,000 km / 15 years for heavy HD	650,000 miles UL; 450,000 miles warranty	At least China VI level; likely extended (TBD)
GHG / CO_2 synergy	Separate HD CO_2 rules; in-vehicle CO_2/energy data	Separate HD GHG Phase 3 (CO_2, CH_4, N_2O)	Dual management: vehicle limits + corporate average intensity

Table 2.2: Summary of different emission legislations [68], [72], [73], [77].

2.4 Future Emission Aftertreatment Architectures.

Implementing new technologies to meet legislation can be difficult from a business perspective. The use of new technologies depends on the payback gap (how an investment is fully amortized through operating savings) and access to capital for large-scale investments. Aligning different stakeholders to match environmental needs with available industrialized technologies is complex in a sector that is diversifying and demanding resources for alternative fuels, electrification, digitalization, the circular economy, etc [34], [35]. To meet future emissions legislation, changes in the after-treatment system will be

needed. These changes will increase system complexity and cost, involving new catalysts, sensors, and control systems to meet requirements on emissions, durability, and monitoring (OBM/OBD).

Different proposals for Euro 7 and EPA 27, using state-of-the-art components, were developed to study the effects on cost and emission performance. The new systems are expected to be US$2,000–5,000 more expensive [33], [35], [67]. For Euro 7, the Advisory Group on Vehicle Emission Standards (AGVES) has two configurations that could meet the requirements, based on a mild or a tough scenario. The proposed system architecture is shown in Fig. 2.6 [72]. Both configurations require a close-coupled catalyst and a Diesel Oxidation Catalyst (DOC) to increase temperature quickly during cold start. The DOC oxidizes hydrocarbons and increases temperature due to the exothermic nature of the reaction.

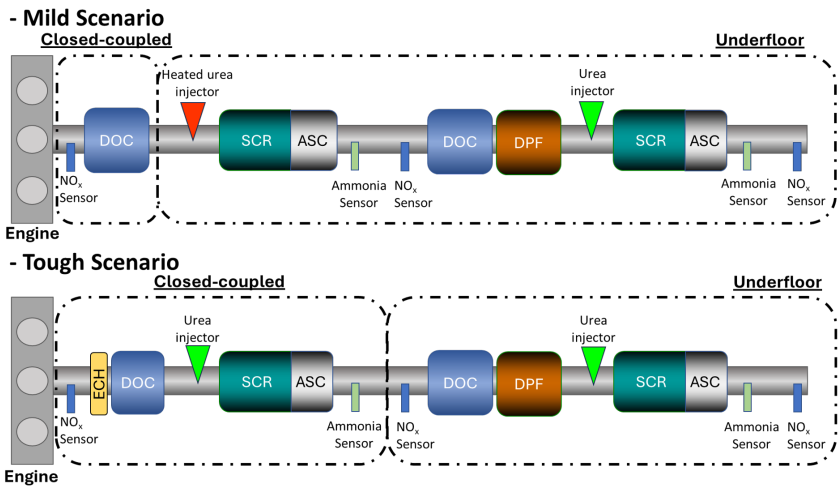

Figure 2.6: Proposed emissions after-treatment systems for Euro VII standard by AGVES [72].

In the tough scenario, the first Selective Catalytic Reduction catalyst + Ammonia Slip Catalyst (SCR+ASC) are placed in the close-coupled location to avoid heat losses, together with an electrical catalyst heater. This lowers the dosing temperature (130°C) and heats the system faster. In the mild scenario, the first SCR+ASC is placed in the underfloor location, and heated urea

injection could help start dosing earlier during cold start [29], [72].

The control system will become more complex because dosing can be controlled at two positions, and the best conditions (low NO_x, low urea consumption, and low NH_3 slip) will depend on engine operation and after-treatment temperature. After the system is heated, there is a transition to rely more on the underfloor SCR+ASC, since NO_x is needed in the Diesel Particle Filter (DPF) for NO_2-driven soot oxidation (passive regeneration). In addition, increasing the NO_2/NO ratio (up to 1) improves NO_x reduction due to the fast-SCR reaction mechanism [63], [72].

The underfloor system has a standard Euro VI-type configuration and allows larger volumes than the close-coupled location, which is beneficial at high speeds and high flow rates. Since NH_3 is regulated, NH_3 sensors are suggested in addition to NO_x sensors to monitor NO_x conversion and NH_3 slip, which can reduce undesired side reactions [63], [72].

The proposal for CARB 27, which is stricter than EPA 27 in the USA, considers a configuration similar to the ones proposed for Euro 7. However, the proposal, as shown in Fig. 2.7 tries to optimize functionality and volume, since a compact after-treatment system increases vehicle payload. This proposal considers a Catalytic Soot Filter (CSF) combining DOC and DPF functions. It also proposes dual-SCR catalysts using different technologies (Cu/Fe zeolites) to widen the operating region [75], [79]. A dual-branch SCR system maximizes space and robustness by using smaller monolith bricks (mechanically stronger), but it could create flow distribution issues. Therefore, more sensors are needed for better control. The control is suggested to be model-based, with real-time feedback and regulation of NH_3 storage capacity, as ahown in Fig. 2.8 [80].

The development of catalyst models for after-treatment systems is an active research field because optimal dosing control based on the current catalyst state is needed under stricter legislation for emissions limits and monitoring. A model-based system can also provide valuable information on catalyst condition for OBD purposes, such as aging, cracking, or other damage. The model can be complemented by sensors to identify anomalies, deviations, and improve estimation accuracy. Model-based approaches are easily scalable, can include relevant performance phenomena such as aging, and, because they include simplified mechanistic elements, provide detailed information about the system and its interactions with the engine [80].

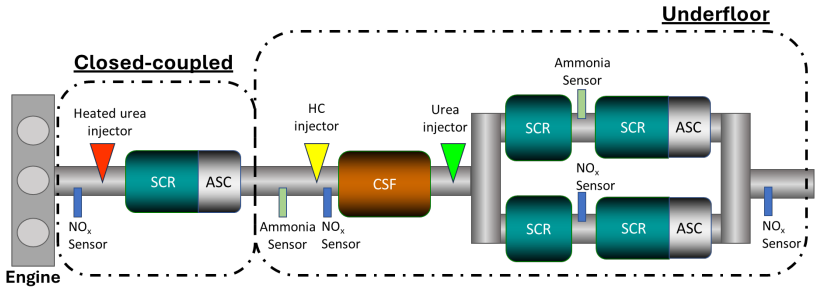

Figure 2.7: Proposed emissions after-treatment system for CARB 27 [75].

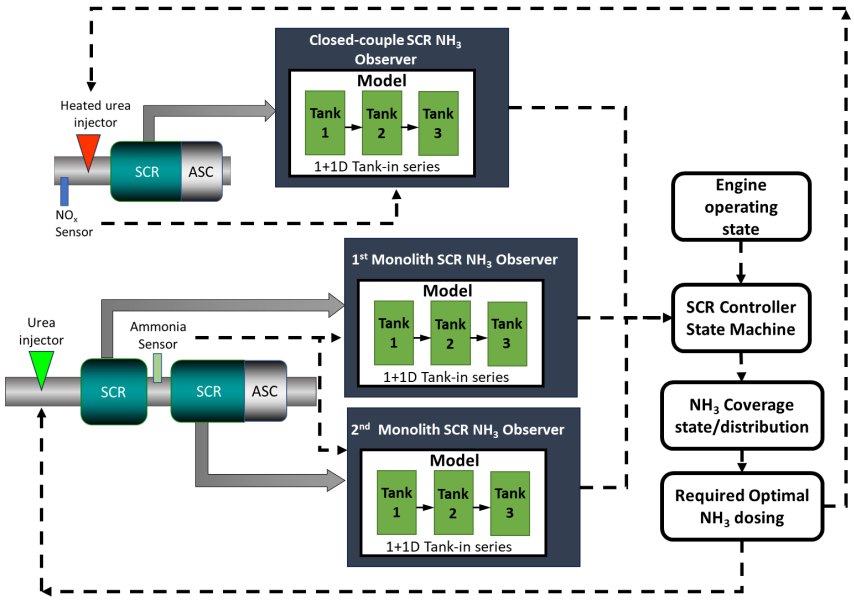

Figure 2.8: Proposed NH_3 model-based control system for CARB 27 [80].

Furthermore, new powertrains using alternative fuels, such as H_2, will require modifications to the after-treatment system. For an H_2 engine, NO_x is the main pollutant. Therefore, an NH_3-based after-treatment system could be used, or an H_2-based system. The NH_3-based system would have a similar

configuration to the Euro 7 or CARB 27 proposals for diesel engines, but optimized for lower temperature, higher water content, and smaller particle emissions [81].

An H_2-based system has the advantage of using H_2 slip from the engine, or using externally supplied H_2 for injection in the after-treatment system. Work by Unni et al. [82] considered an H_2 system with a TWC catalyst and suggested that additional H_2 injection could increase conversion. However, TWC catalysts are only suitable for engines operating under stoichiometric conditions ($\lambda = 1$). For lean engines, H_2-SCR with high selectivity is a more appropriate option. Different H_2-SCR technologies provide different NOx conversion levels and may require different configurations. In addition, these technologies could produce N_2O and NH_3, which would need to be mitigated or coupled with an NH_3-SCR catalyst. If H_2 slip is not sufficient, dual systems could be used with reduced urea injection, although this introduces a CO_2 penalty, depending on the NH_3 source for urea production. H_2-SCR catalysts can achieve NO_x conversion at lower temperatures than NH_3-SCR catalysts (around 150°C). In this system, model-based control can also optimize system operation, monitoring, and diagnostics [81], [83]. An aftertreatment configuration with a dual H_2 and NH_3-based catalysts is presented in Fig. 2.9.

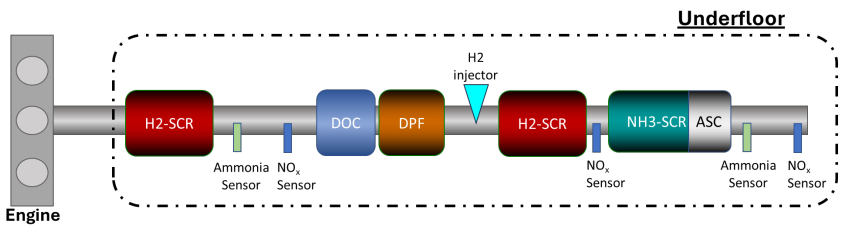

Figure 2.9: Proposed emission after-treatment system for hydrogen lean engines using a H_2-SCR [81], [83].

2.5 The H_2-SCR and NH_3-SCR Catalysts: A Brief Overview.

On H_2-SCR catalysts for hydrogen engine operation under lean conditions (excess oxygen), the exhaust contains high concentrations of oxygen and water.

Since NO_x is formed during combustion in the engine, the following reactions can occur under this exhaust gas composition (I to V).

$$\text{R1:} \quad 2\,NO + 2\,H_2 \longrightarrow 2\,H_2O + N_2 \tag{I}$$

$$\text{R2:} \quad 2\,NO + H_2 \longrightarrow N_2O + H_2O \tag{II}$$

$$\text{R3:} \quad 2\,NO + 5\,H_2 \longrightarrow 2\,NH_3 + 2\,H_2O \tag{III}$$

$$\text{R4:} \quad 2\,NO + O_2 \longleftrightarrow 2\,NO_2 \tag{IV}$$

$$\text{R5:} \quad 2H_2 + O_2 \longrightarrow 2H_2O \tag{V}$$

The desired pathway is NO reduction (Reaction I), but Reactions II and III are side reactions that form N_2O and NH_3. Reaction IV represents the NO_x oxidation equilibrium, and H_2 oxidation (Reaction V) is a competing reaction that reduces the availability of H_2 for the H_2-SCR reaction [84], [85].

For H_2-SCR catalysts, two technologies are being developed: Pd- or Pt-based active metals. Both technologies show two main reaction mechanisms. At low temperatures (100–150°C), NO dissociates on the active metal. At intermediate temperatures (150–200°C), NH_3 is formed and NO is reduced through the NH_3-SCR mechanism [85].

These mechanisms proceed in different ways depending on the active metal and the support. The most accepted and complete description is the bifunctional mechanism (Fig. 2.10, which suggests that reaction steps occur both on the active metal (NO + H_2 reactions with low selectivity) and on Brønsted sites of the support (NH_3-SCR) [86], [87].

This mechanism was later refined by a better description of the metal–support interface (Fig. 2.11, which explains two routes for N_2O formation. On Pd surfaces, H_2 dissociates, and at the Pd–support interface, H-spillover effects are enhanced [88].

NH_3-SCR catalysts are vanadium-based or zeolite-based. Vanadium-based catalysts provide the highest NO_x conversion in the 300–450 °C range and are resistant to poisoning by sulfur and alkali metals. Vanadium-based SCR catalysts contain different vanadium structures that interact with the support and promoters, and these structures are highly dynamic. The vanadium loading is typically low (3–7 wt%), below monolayer coverage, which tends to give high NO_x conversion while remaining stable under different operating conditions [89], [90].

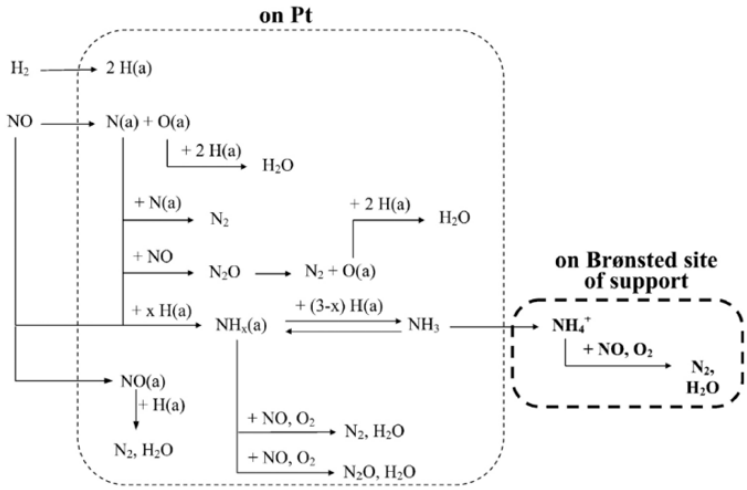

Figure 2.10: Bifunctional reaction mechanism for a H_2-SCR catalyst. Reproduced with permission from [86]. © 2026. American Chemical Society.

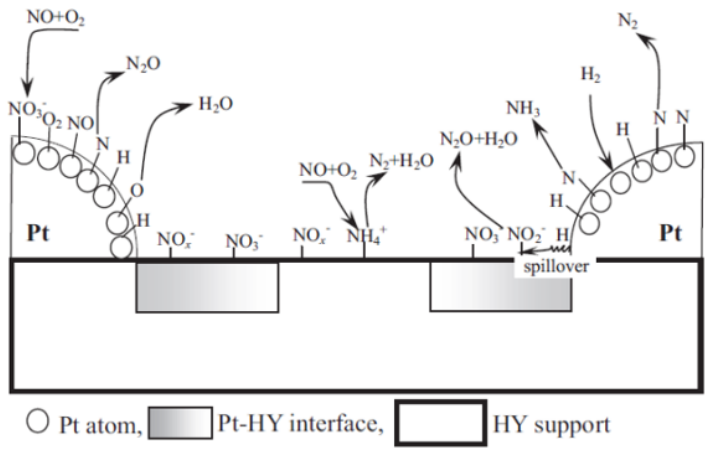

Figure 2.11: Reaction mechanism with a detailed metal-support interaction for a H_2-SCR catalyst. Reproduced with permission from [88]. © 2026. Elsevier.

The support for the vanadium-based SCR catalyst is usually titanium oxide

(TiO_2), since it enhances hydrogen mobility and provides NH_3 storage. TiO_2 is typically used in its anatase form, which is stable up to 500°C and has a high surface area (50–85 m^2/g). Tungsten (W) is a common promoter that increases surface acidity, increases NH_3 capacity, and delays sintering at high temperatures. It can also introduce sites with different properties, which broadens the operating window [89], [91].

The vanadium species in the catalyst are sensitive to oxidizing and reducing environments. The vanadium oxidation state can vary from $^{+5}$ to $^{+4}$ and $^{+3}$ under reducing conditions. In dry conditions and at high oxygen concentrations, vanadium can reach the highest oxidation state. Vanadium species can be monomeric or polymeric, with well-defined structures and properties. The effect of water depends on the temperature: at high temperatures, the vanadium species largely keep their structure and hydrolization can happen between H_2O and V=O groups forming $V(OH)_2$ sites, increasing Brønsted acidity. At low temperatures, a water layer can block active sites[89], [92], [93].

Different kinetic models have been developed to understand the main reaction steps and reaction dynamics in vanadium-based SCR catalysts. A power-law kinetic model for the overall SCR mechanism can give insight into how different species affect the SCR reaction rate. The following model and its parameters were reported for a vanadium-based catalyst based on different kinetic studies [94], [95].

$$\begin{aligned} \text{Overall SCR} \quad & 4\,NO + 4NH_3 + O_2 \longrightarrow 4\,N_2 + 6\,H_2O \\ & r_{NO} = Ae^{-\frac{E_{act}}{RT}}[NO]^{\alpha}[O_2]^{\beta}[NH_3]^{\lambda}[H_2O]^{\delta} \end{aligned} \tag{2.1}$$

	α	β	λ	δ	E_a **(kJ/mol)**	Ref.
$\mathbf{V_2O_5/TiO_2}$	0.5 - 1.0	0.2 - 0.5	0 - 1[a]	-0.10 - -0.14	41 - 50	[94], [95], [96]
[a] $\lambda = 0$ at high concentrations, $\lambda = 1$ at low concentrations or low NH_3 / NO ratios.						

Table 2.3: Reaction orders for the NO conversion rate power law kinetics for the vanadium-based SCR.

Oxygen has a reaction order close to zero since it is in excess in a lean diesel engine. However, it is relevant in the re-oxidation of vanadium sites and it can become the limiting step under low-temperature conditions [95], [97].

For NH_3, the reaction order depends on gas concentration: it is zero order when the maximum NH_3 adsorption capacity is reached. When the NH_3 concentration is low, NH_3 is mostly adsorbed on Brønsted sites which need to be actiavted and can be a limiting step with a reaction order close to one [96]. H_2O can have a negative reaction order since it competes for adsorption sites with NH_3 [97], [98]. The NO reaction order is positive but depends on the NH_3 level. It has also been reported that the apparent activation energy depends on catalyst preparation and vanadium content [95], [99].

A global reaction mechanism for vanadium-based SCR is challenging because it involves different vanadium species with different behavior and reaction pathways [100]. The most accepted mechanism was proposed by Topsoe et al. [101], [102], shown in Fig. 2.12, and it provides the basis for more complex mechanisms. In this redox mechanism, NH_3 is adsorbed on the catalyst and reacts with gas-phase or weakly adsorbed NO. Vanadium species are the active sites, but Ti and W can serve as reservoirs for NH_3. NH_3 adsorbed on a Brønsted vanadium acid site is activated by an adjacent redox site (V or Ti). When NH_3 is activated, it reacts with NO to form H_2O and N_2, reducing the vanadium site. The reduced site is then re-oxidized and the cycle can repeat [91], [103].

The fast-SCR reaction was added in a more complete mechanism by Arnanson et al. [104], which is a two-cycle mechanism. The main differences between these two cycles are how NO is activated and how re-oxidation occurs: the standard SCR cycle uses NO + O_2, while the fast-SCR cycle uses NO_2. The mechanism is shown in Fig. 2.13 [104], [105].

Another mechanism for a vanadium-based SCR catalyst was proposed by Lian et al. [106], which differentiates between polymeric and monomeric vanadium species, arguing that the former has higher activity. This is because polymeric vanadium species have more vanadium atoms close to each other, which can facilitate activation and re-oxidation. The mechanism also shows a role for the support as an NH_3 buffer and for NH_3 activation. The mechanism is shown in Fig. 2.14 [106], [107].

Transforming these reaction mechanisms into kinetic models is challenging. Several issues need to be addressed, such as NH_3 adsorption–desorption dynamics on Lewis and Brønsted sites, the activation and re-oxidation of active sites, and the rate-determining steps under different conditions. In addition, new reaction pathways and the role of compounds such as H_2O, O_2,

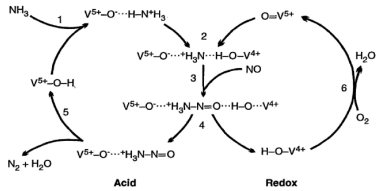

Figure 2.12: Standard SCR mechanism proposed by Topsoe et al. Reproduced with permission from [101]. © 2026. AAAS.

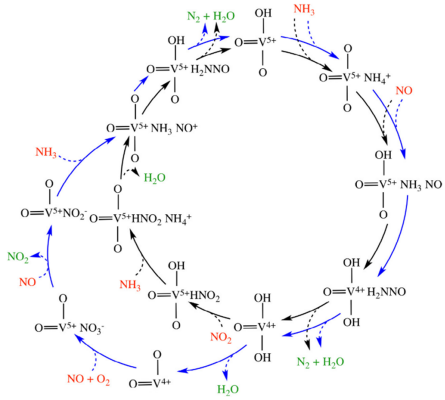

Figure 2.13: Two-cycles SCR mechanism proposed by Arnarson et al. Reproduced with permission from [104]. © 2026. Elsevier.

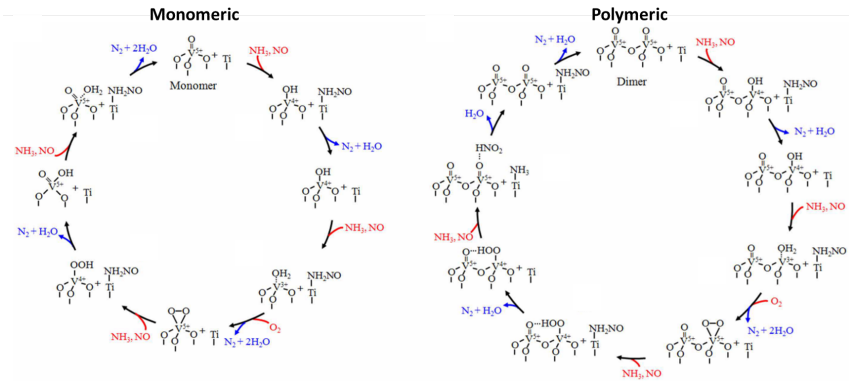

Figure 2.14: SCR mechanism for a monomer and dimer vanadium over a TiO_2 surface. Taken from [106].

and NO_2 still need to be investigated.

A kinetic model of these mechanisms is complex since it involves several parameters that are highly correlated and non-linear. One of the most basic kinetic models proposed for a vanadium-based SCR catalyst is an Eley–Rideal mechanism, where NH_3 is adsorbed on a Brønsted vanadium site (V^{5+}–OH)

and NO reacts from the gas phase or is weakly adsorbed. The Eley–Rideal model does not consider the re-oxidation step, which can be limiting under certain conditions (especially low temperature) [102], [108], [109]. This step is often described by a Mars–van Krevelen mechanism [109], [110].

An improvement to consider NH_3 inhibition at low temperature was proposed by Tronconi et al.[108]. This model involves two main sites: one acidic site and one redox site. The acidic site adsorbs NH_3, while the redox site activates NH_3 and adsorbs O_2 and NO. In the re-oxidation step, the O_2 dependence is simplified using a power-law expression. Furthermore, Tronconi et al.[109], [111] proposed a pathway for periods when NH_3 is not available. In this case, nitrate species can form at the vanadium active site from adsorbed NO or NO_2. When NH_3 is available, ammonium nitrate can form at low temperature and block reaction sites, but this is reversible at high temperatures where it decomposes into N2 and H_2O [108].

To account for NO_2, Cincidelli et al.[111], [112] integrated an NO_2 reaction mechanism into the kinetic model proposed by Tronconi et al.[108]. At the moment, this is one of the most complete kinetic models because it accounts for NH_3 inhibition at low temperatures, NH_3 adsorption on multiple sites through a Temkin adsorption mechanism, and NH_3 dynamics between redox and acid sites [112], [113]. However, deviations in the predicted NH_3 outlet concentration suggest a lack of fit in how NH_3 adsorption dynamics are assumed and modeled.

NH_3 adsorption is one of the most important steps to understand vanadium-based SCR catalysts and to develop more accurate models. However, it is challenging due to the diversity of sites in the catalyst and their interactions. These sites can be divided into two main types: molecular NH_3 adsorption on Lewis sites, or activated adsorption as NH_4^+ on a Brønsted acid site. A Lewis site (M=O) has an empty orbital that can accept an electron pair, while a Brønsted site (M–OH) can donate a proton [91], [92], [114]. In addition to this classification, adsorption sites in the vanadium-based SCR catalyst can differ due to local structure and how oxygen and vanadium atoms are distributed.

Different vanadium species have been identified that can adsorb NH_3: monomeric vanadium in a tetrahedral configuration, two-dimensional polymeric clusters (with dimers as the smallest cluster), and V_2O_5 clusters[91], [115], [116]. Additionally, Wachs et al.[89] reported Lewis sites on TiO_2 and Brønsted and Lewis sites on tungsten (W). They also reported that Lewis

sites can be transformed into Brønsted sites in the presence of water at high temperatures (>250°C).

The role of the support, TiO_2, in NH_3 adsorption was also mentioned by Topsoe et al.[91], since it can interact strongly with the vanadium active site (e.g., via Ti–OH groups), which can help with NH_3 activation. They found NH_3 still adsorbed at high temperatures (>300°C), since Lewis sites have a higher adsorption energy. This NH_3 buffer is relevant for NO_x conversion at high temperatures. Fig. 2.15 shows some of the vanadium species structures that are involved in NH_3 adsorption. These species have different properties, which helps explain the wide operating window of SCR catalysts. However, the identification of those sites for modeling purposes will depend on the accuracy needed and on the ability to discriminate between structures from experimental data, since their behavior can be similar and overlap.

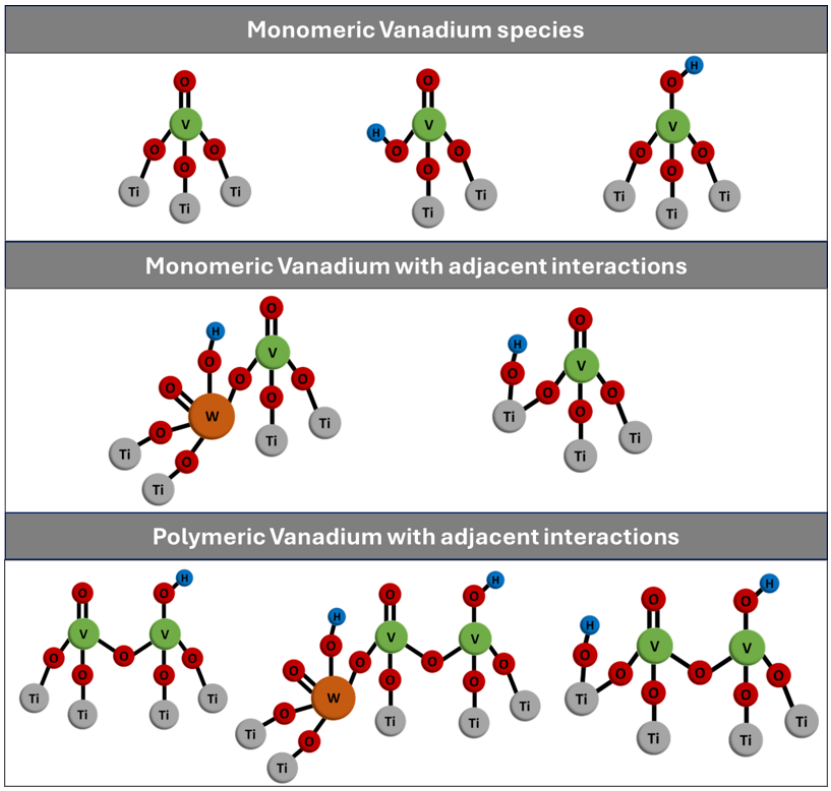

Figure 2.15: Multiple vanadium species present in vanadium-based SCR catalysts for NH_3 adsorption.

CHAPTER 3

Experimental Framework

"Facts do not cease to exist because they are ignored"

— Aldous Huxley

3.1 Gas Flow Reactor

A gas flow reactor is a setup used to measure catalytic activity and processes such as adsorption in a controlled environment, where flow, temperature, and gas composition are regulated with high accuracy and precision. This method is relevant for building a bridge between molecular insight into how the surface interacts with gas species and the highly dynamic application, since it emulates the same geometry and flow regime. A scheme on the main components of a gas flow reactor is presented in Fig. 3.1.

Some advantages include good resolution for capturing storage and kinetics under realistic conditions. It also provides information about mass transfer effects that are present in the application. The gas flow reactor allows dynamic experiments, which are vital for decoupling catalyst features such as storage and transient desorption. By using Fourier Transform Infrared (FTIR) spec-

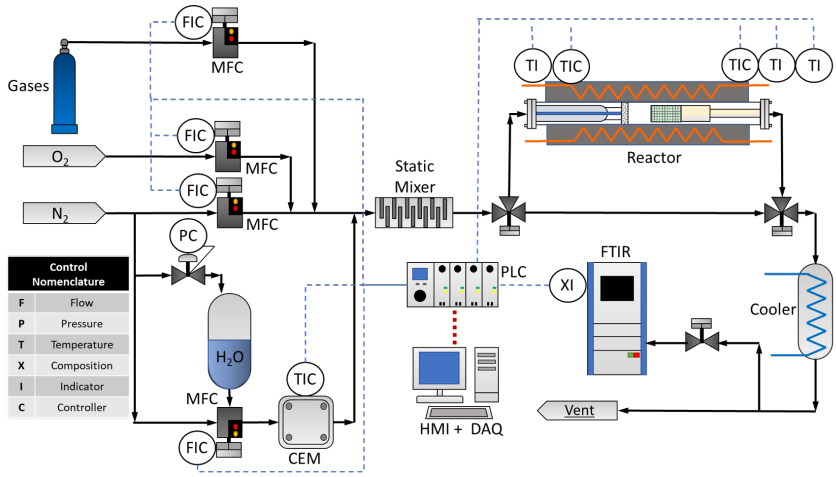

Figure 3.1: Gas flow reactor experimental setup scheme. CEM: Controlled Evaporator and Mixer module. FTIR: Fourier Transform Infrared Spectrometer Gas Analyzer. MFC: Mass Flow Controllers. HMI and DAC: Human Machine Interface and Data Adquisition.

trometer, which is a well-established technique for compound identification, it is possible to simultaneously identify gas concentrations.

A gas flow reactor is considered an integral reactor because the gas composition changes along the monolith length due to reaction, and the outlet composition is the cumulative effect of the whole catalyst sample. This response, driven by axial gradients, must be accounted for when developing models [117], [118].

For a gas species i, the mass balance of species i in a plug flow reactor is expressed as Eq. 3.1.

$$\frac{dF_i}{dz} = A_{geo} R(y(z), T, \theta(z)) \tag{3.1}$$

In a gas flow reactor, the integral over the catalyst sample is defined by the inlet concentration (set by the MFCs) and the outlet concentration (measured by the FTIR), Eq. 3.2.

$$F_i - F_{out} = \int_0^{z_{out}} A_{geo} R(y(z), T, \theta(z)) dz \tag{3.2}$$

Where F is molar flow, z is the catalyst axial length, A_{geo} is the catalyst surface area, and R includes the mass transfer and reaction terms which are dependent on gas concentration (y), temperature (T) and adsorbed species (θ), with parameters to be estimated through an optimization task. The integral reactor gives realistic axial gradients, which capture the interplay between transport and kinetic effects. In addition, the outlet time-series data provides dynamic information such as hysteresis, tailing, and breakthrough, which have clear mechanistic interpretations. However, proper experimental design is needed to capture these effects with good resolution and without artifacts.

For modelling purposes, the gas flow reactor is operated under experimental conditions, and it is designed to ensure the following assumptions [95], [108], [111], [119]:

- Plug flow in axial direction, so axial dispersion is negligible compared to convective flow.
- Uniform flow distribution accross the channels. Radial gradients are negligible.
- Isothermal or adibiatic reactor zone or well-controlled and monitored temperature to use in the model optimization.
- Ideal gas behavior with well-defined inlet composition.
- Usually no pressure drop effects are considered or effects are negligible on the reaction rates.
- Aging or deactivation effects are not occuring during the experiment, unless that was the purpose.
- FTIR measurements give the true outlet composition if delay and dispersion effects are corrected.

In this thesis, the gas flow reactor was the main experimental method to gain insight into NH_3 adsorption on a vanadium-based SCR catalyst and into support effects in the H_2-SCR reaction for a Pd-based catalyst. These experiments have different goals regarding the modelling needs and the research questions to be answered. However, the experimental workflow aimed to maximize the amount of information while using resources efficiently. A detailed explanation of the experiments is described below.

NH_3 Adsorption Experiments

NH_3 adsorption experiments were performed in the gas flow reactor using a state-of-the-art vanadium-based SCR catalyst from Umicore. The catalyst sample was a washcoated monolith with TiO_2 as support and tungsten (W) as promoter. To capture dynamic effects in NH_3 adsorption related to washcoat thickness, two washcoat loadings with the same formulation were tested. In addition, to capture NH_3 adsorption at low concentrations, a smaller sample and a low-concentration NH_3 gas bottle (1%) were used. The three samples in this campaign are described in Table 3.1.

ID	Description	Length (cm)	Diameter (cm)	Weight (g)	Nominal Washcoat Loading (g/L)
HC-LL	High Concentration, Low Loading	7.64	2.43	20.67	288
HC-HL	High Concentration, High Loading	7.68	2.48	23.77	371
LC-LL	Low Concentration, Low Loading	2.66	2.52	7.15	288

Table 3.1: Vanadium-based SCR sample properties.

Each sample was degreened to stabilize the catalyst and remove adsorbates from the surface. The sample was considered stabilized when two consecutive SCR activity measurements were identical. The degreening protocol is shown in Table 3.2.

Procedure	Step	Flow (NL/min)	Temp. (°C)	Composition	Time (min)
De-greening	Purging	30	450	5% H_2O	5
	SCR Activity	30	450	500ppm NO, 500ppm NH_3, 5% H_2O	5
	Stabilization	30	450	5% H_2O, 5% O_2	10, 20, 60
	Final Purging	30	450	N_2 only	5
	Oxidation	30	450	5% O_2	20

Table 3.2: Vanadium-based SCR Samples degreening protocol.

NH_3 adsorption experiments were performed for both the oxidized and reduced catalyst states. The catalyst state was set during the pre-treatment sequence. The oxidized state was obtained by O_2 oxidation, and the reduced state by subsequent NH_3 reduction at high temperature (500°C). The pretreatment protocol is described in more detail in Table 3.3.

Catalyst State	Step	Flow (NL/min)	Temp. (°C)	Composition	Time (min)
Oxidized State	Purging	50	500	N_2 only	3
	Oxidation	50	500	5% O_2	10
	Purging	50	500	N_2 only	3
Reduced State	Purging	50	500	N_2 only	3
	Oxidation	50	500	5% O_2	10
	Purging	50	500	N_2 only	3
	Reduction	50	500	500ppm NH_3	20
	Purging	50	500	N_2 only	2

Table 3.3: Vanadium-based SCR Samples pretreatment protocol.

.

After the pretreatment, the temperature and water concentration were set to the NH_3 adsorption conditions. The NH_3 adsorption experiment is described in Fig. 3.2. The experiment is based on desorption steps in which steady state is reached, and the dynamic response between steps is captured. The first step, an adsorption step, aims to saturate the catalyst, but it does not need to reach equilibrium. This is because the accumulation used to estimate the adsorption isotherms is evaluated by integrating the inlet and outlet concentration signals. In general, desorption reaches steady state faster than adsorption.

The experiments were performed at three different water concentrations: 0, 0.5, and 5%. For the low-concentration experiment, NH_3 ranged from 30 to 75 ppm, while for the high-concentration experiment it ranged from 75 to 450 ppm. The total gas flow was set to 50 NL/min. The temperature ranged from 100°C to 250°C for the oxidized sample (at temperatures above 250°C, NH_3 oxidation cannot be neglected), and from 100°C to 400°C for the reduced sample. Each experiment was repeated twice to assess repeatability and estimate measurement error.

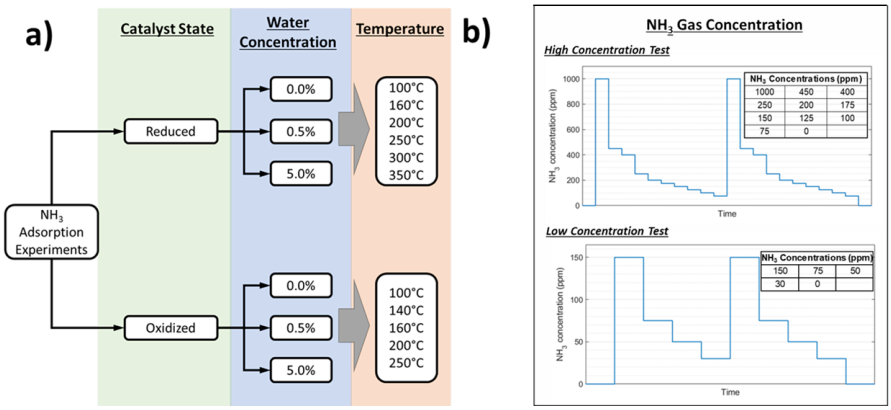

Figure 3.2: NH_3 adsorption experiments, (a) Conditions for the catalyst state, water concentration, and temperature, and (b) NH_3 concentration steps sequence for high concentration and low concentration experiments. Taken from [120].

H_2-SCR Experiments across Catalyst Supports

H_2-SCR activity tests to study support effects on Pd-based H_2-SCR catalysts were performed on samples synthesized and washcoated on cordierite monoliths. Four supports with the same PGM loading (1 wt% Pd) were studied: the metal oxides Al_2O_3 and TiO_2, and the zeolites BEA and SSZ-13. Each monolith had a diameter of 2.1 cm and a length of 2 cm. The gas flow was set to 15 NL/min, which was the lowest flow the experimental rig could achieve. To further reduce the space velocity (65,000 h^{-1}), two monoliths were placed in series in the reactor.

Each sample was degreened in a similar way to the vanadium-based SCR catalyst samples, but H_2 was used instead of NH_3. Table 3.4 presents the degreening procedure for these samples.

H_2-SCR activity tests were performed for a sample consisting of two monoliths in a row with the same catalyst washcoat. For each sample after a pretreatment sequence in which the sample was set to the highest oxidation state. Table 3.5 describes the pretreatment, performed at 500°C.

After the pretreatment, the temperature and water concentration were set for the H_2-SCR activity experiments, where different H_2 concentrations were studied. For all experiments, the oxygen concentration was set to 10% and NO

Procedure	Step	Flow (NL/min)	Temp. (°C)	Composition	Time (min)
De-greening	Purging	30	450	5% H_2O	5
	H_2-SCR Activity	30	450	500ppm NO, 500ppm H_2, 5% H_2O, 10%O_2	30
	Final Purging	30	450	N_2 only	5

Table 3.4: Pd-based H_2-SCR Samples degreening protocol.

Procedure	Step	Flow (NL/min)	Temp. (°C)	Composition	Time (min)
Pre-treatment	Purging	15	500	N_2 only	3
	Oxidation	15	500	5% H_2O, 10%O_2	30
	Purging	15	500	N_2 only	3

Table 3.5: Pd-based H_2-SCR Samples pretreatment protocol.

.

to 500 ppm. Water concentration was varied between 0, 5, and 10% to study water effects. Eight temperatures in the range 100–300°C were tested.

For each condition (temperature, water, and NO), H_2 steps were performed and steady state was reached at each step. The H_2 concentration was set to 7500, 5000, and 2500 ppm, corresponding to H_2/NO ratios of 15, 10, and 5, respectively. Each experiment was repeated twice to assess repeatability. The H_2-SCR activity experiment is described in Fig. 3.3.

In addition, washcoat characterization experiments were performed to obtain additional data on the porous structure, Pd oxidation state, and dispersion. These experiments are summarized in Table 3.6.

Experimental results on catalytic activity (NO reduction), for the H_2-SCR samples in this study, are presented in Fig. 3.4. The results cover a wide experimental region, which is a challenge on visualization strategies to give enough information about the experiment and at the same time easy to understand.

3.2 Maximizing Information from Experiments

For the experiments performed in the gas flow reactor, the conditions were chosen to maximize the information that can be extracted from the experimen-

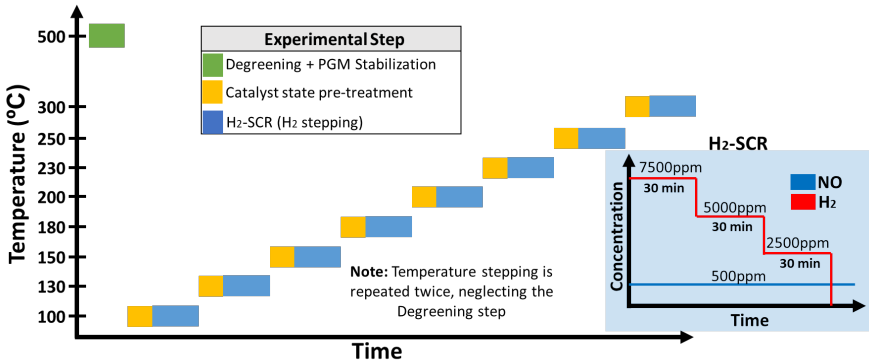

Figure 3.3: Experimental protocol for H_2-SCR catalysts samples

CO Chemisorption	Estimates Metal dispersion. Not suitable for TiO_2 supports dues to Strong Metal-Support Interaction (SMSI) effects
H_2 Physisorption	Provides surface area and pore volumes (BET and t-plot methods)
ICP-SEMS	Inductively coupled plasma sector field mass spectrometry. Estimate Pd content.
XRD	X-ray Diffraction. Evaluates crystalline structure.
XPS	X-ray Photoelectron spectroscopy. Studies oxidation states.
NH_3-TPD	NH_3 Temperature Programmed Desorption. Studies adsorption strength and capacity.

Table 3.6: Additional experiments performed to the H_2-SCR samples. [121], [122], [123]

tal data. This is important because using the experimental rig to test multiple conditions consumes time and resources.

In a gas flow reactor, many variables can be changed and will affect the catalyst sample, such as flow rate, temperature, and gas composition. First, a screening stage was carried out, where selected variables were varied at a few extreme values, guided by prior knowledge from previous research. This pre-screening had two objectives: (1) identify the variables that show the highest sensitivity for the features of interest (NH_3 adsorption and H_2-SCR reactions),

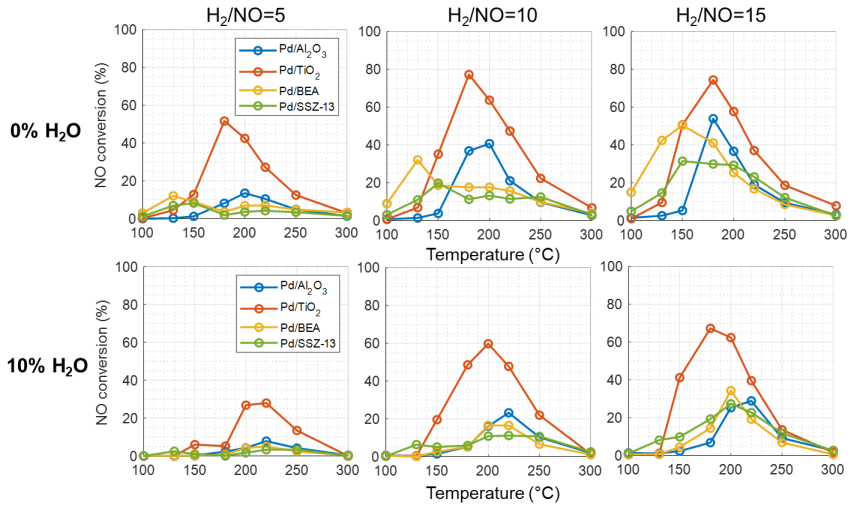

Figure 3.4: NO conversion as a function of temperature for the different H_2-SCR catalysts. Rows refer to different water concentrations; Columns refer to different H_2/NO. NO concentration is 500 ppm and O_2 concentration is 10%.

and (2) find a suitable resolution where changes are properly captured within an acceptable time range and operating window [124], [125].

During this screening stage, the system is approximated with a linear model to analyze the main effects and interactions of the variables, and to define the experimental region. The linear model is stated in Eq. 3.3, where $x_{i,j}$ is the value of variable j in experiment i. In matrix form, it can be expressed as Eq. 3.4 [126], [127].

$$y_i = \beta_o + \sum \beta_i x_{ij} + \varepsilon_i \tag{3.3}$$

$$y = X\beta + \varepsilon \tag{3.4}$$

The parameter vector, β, fitted to the linear model, is then found as shown in Eq. 3.5. The variance is expressed in Eq. 3.6, and the information matrix in Eq. 3.7, where σ^2 is the variance of the measurement error [125], [126].

$$\hat{\beta} = (X^T X)^{-1} X^T y \tag{3.5}$$

$$var(\hat{\beta}) = \sigma^2(X^T X)^{-1} \tag{3.6}$$

$$M = \frac{1}{\sigma^2}(X^T X) \tag{3.7}$$

In the screening phase, the columns in the X matrix should be as orthogonal as possible. This indicates reduced correlation between parameters and helps identify the most important variables. It is also possible to study how small changes in beta produce a relevant change in y by estimating sensitivities. For each experiment i, the sensitivities are defined as Eq. 3.8 [125], [128].

$$S(x_i, \beta) = \begin{pmatrix} \frac{\partial y(x_i,\beta)}{\partial \beta_1} \\ \vdots \\ \frac{\partial y(x_i,\beta)}{\partial \beta_p} \end{pmatrix} \tag{3.8}$$

This preliminary analysis helps explain how the response of the studied feature depends on the variables, and how the experimental data influences each parameter. From the sensitivity analysis, it is also clear why experimental conditions where catalyst conversion is 100% are not useful for modelling. In these conditions, the response lies on a plateau, meaning that $\partial y/\partial \beta$ and $\partial y/\partial x$ are small, so the sensitivities are close to zero. These conditions are mainly interesting from a performance point of view.

Based on this analysis, the experimental conditions were then specified by increasing the number of levels for the variables with the highest sensitivities and expected non-linearities: temperature and gas composition.

Replication runs are also important because they provide a diagnostic tool to identify and estimate pure experimental error (the noise level of the system), test lack-of-fit of the model, and monitor anomalies in the experimental setup and sample.

Pretreatment analysis is included in the replication process, since the pretreatment is intended to stabilize the catalyst sample in a well-defined state before the experiment. This could relate to oxidation state, coverage of adsorbed species, etc. If the pretreatment is not stable across conditions, this will be reflected in poor repeatability. That can increase the pure experimental error or lead to wrong conclusions about the catalyst sample.

3.3 Processing of Experimental Data

For studying catalyst activity in a gas-flow reactor, and the dynamic and steady effects of catalytic materials in a gas mixture, two signals must be processed to properly capture the features of interest. The gas inlet composition is determined by the gas flow rates on the mass flow controllers (MFCs), q_{MFC}, and the outlet gas concentration is measured by the FTIR, y_{FTIR}.

These signals are used to define activity under steady-state conditions, dynamic effects when inlet conditions change, and accumulation, which reflects adsorption or storage effects on the catalyst sample. For all of these analyses, both signals must be preprocessed to remove artifacts from the experimental setup and to correct for dispersion and delay effects. A real reactor has a defined volume that separates measurement points, and the gas becomes dispersed due to axial diffusion (both forward and backward) relative to the average flow velocity.

Fig. 3.5 shows the preprocessing method and the steps used to obtain steady-state, dynamic, or accumulation data for the features studied in the experiment.

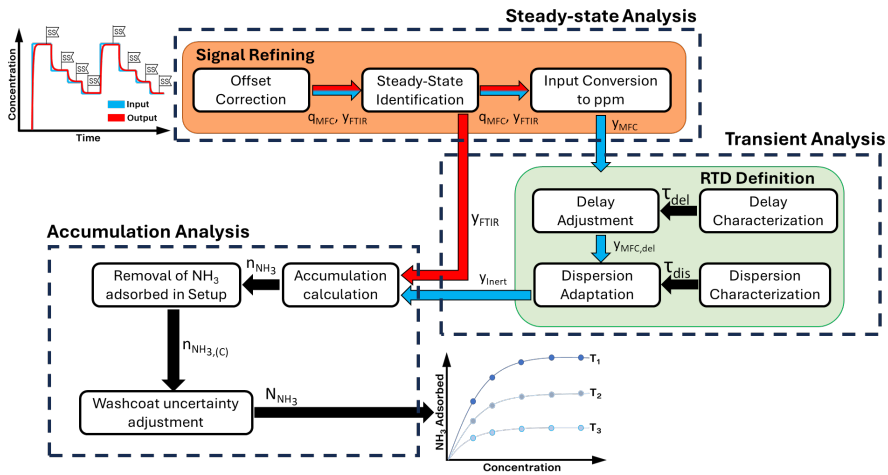

Figure 3.5: Data processing proposed method gas flow reactors data analysis.

Each step is described below in more detail.

Signal refining: In this step, reference values from the FTIR are used to

perform the following calculations: the y_{FTIR} offset is corrected; steady-state periods are identified using q_{MFC} and a statistical criterion ($\sigma < 5$ ppm); and q_{MFC} inlet flow rates are converted to an inlet gas concentration, y_{MFC}, using FTIR reference values.

RTD definition: In this step, the delay and dispersion effects of the experimental setup are characterized using a residence time distribution (RTD) model. The inlet composition, y_{MFC}, is matched to a signal obtained from an inert tracer measured at the outlet, which is the same location where the FTIR measures the outlet gas composition, y_{FTIR}.

Accumulation calculation: For NH_3 adsorption studies, the accumulated NH_3 on the catalyst is estimated using Eq. 3.9 in this thesis for each desorption step, based on the processed input and output signals, y_{MFC} and y_{FTIR}.

$$n_{\mathrm{NH_3}} = F_{total} \int_0^{t_{int}} (y_{inert} - y_{FTIR})\, dt \tag{3.9}$$

Removal of NH_3 adsorbed in the setup: For gas species that can adsorb in the experimental setup, such as NH_3, a correction is applied by estimating the amount of NH_3 adsorbed in the setup using similar experiments performed without a catalyst sample. The setup adsorption is represented using a two-site Langmuir adsorption model and is removed from the outlet signal (both steady and dynamic) across different experimental conditions (temperature, water, and NH_3 concentration). This avoids overestimating NH_3 stored on the catalyst.

Washcoat uncertainty adjustment: When testing different samples with varying washcoat loading, the results are normalized by washcoat loading to increase the effective sample size. Some deviations in the data trend (for example, adsorption isotherms) may be explained by small deviations in sample production relative to the nominal washcoat loading. An optimization algorithm was developed to vary the nominal washcoat loading within a +/- 10% range to make the adsorption isotherm trend continuous and smooth.

Fig. 3.6 shows the contribution of the experimental setup and its artifacts to the NH_3 adsorption measurements for a vanadium-based SCR catalyst. The data-processing method proposed in this study enables quantification of this impact, providing greater control over the experimental data. The magnitude of the contribution differs between the reduced and oxidized catalyst, since the reduced catalyst state has lower NH_3 storage capacity.

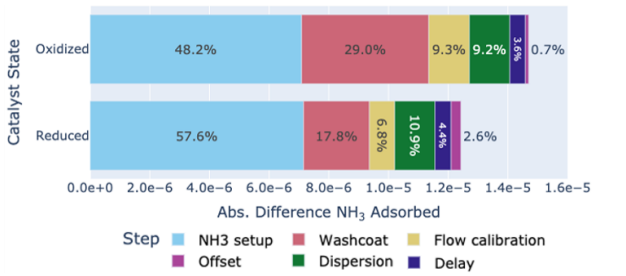

Figure 3.6: Contribution of each preprocessing step in the overestimation magnitude between unprocessed and processed data for the NH_3 adsorption on a vanadium-based SCR catalyst. Taken from [120]

CHAPTER 4

Modelling Framework

"Man is so fond of systems and abstract deductions that he is ready to distort the truth intentionally"

— Fyodor Dostoevsky

4.1 The 1+1D Single-Channel Catalyst Model

There are different methods for catalyst modelling in after-treatment systems. The methods can be grouped by the number of dimensions included and by whether they are steady-state or transient. Increasing the number of dimensions usually results in more accurate models, but it can be computationally expensive or even unfeasible even with current advances in computing, especially when simulating complex transient experiments or full driving cycles. 3D models are mostly used for steady-state studies, or they require simplifications of the reaction mechanism and mass-transfer phenomena to handle transient data.

An adequate level of detail, while still being able to handle transient data with reasonable computing effort, which is relevant to automotive applications,

is the 1+1D single-channel catalyst model (SCM). In this model, the gas-phase flow is solved along the channel axis in one dimension, while transport through the washcoat and surface reaction are solved in an additional dimension (1+1D) [108], [129], [130], [131]. External mass and heat transfer are included through a film model using Sherwood and Nusselt empirical correlations, which have been studied extensively for catalyst monoliths with different channel geometries [132], [133]. Some improvements include allowing a non-uniform washcoat thickness, since the washcoat does not lead to perfectly square channels. Instead, the corners become rounded and more washcoat tends to accumulate there [134], [135].

The main assumptions in this modelling approach are isobaric conditions, diluted gas species, and a homogeneous gas composition (no radial gradients). Depending on the complexity of the mass and heat balances, the resulting ordinary differential equations (ODEs) can be solved analytically, by a numerical method (ODE solver), or by a discretisation scheme. Since the mass balances usually include several adsorbed species, reactions, and compounds with non-linear behaviour, a discretisation scheme is most commonly used. In this scheme, the channel is divided into a series of continuous stirred-tank reactors (CSTRs). For each tank, a pseudo-steady-state is often assumed for the gas-phase species, because the adsorption dynamics are slower and gas accumulation can be neglected [136].

Within each tank, there is an additional discretisation of the washcoat by dividing it into layers. In each layer, the gas-phase mass balance is coupled with diffusion and surface reaction in the porous washcoat [112], [137], [138]. For the calculation of effective diffusivity, the parallel pore model is used, which accounts for both molecular and Knudsen diffusion[139], [140]. The mass balance from the gas phase to the washcoat is described in Eq. 4.1a, and diffusion within the washcoat in Eq. 4.1b. As noted, the tanks interact through Eq. 4.1a, since axial transport within the washcoat is negligible. In the equations, i refers to gas species, k to the tank in the axial discretization, n the layer in the washcoat discretization, m is the reaction index, and j is the site index. F is the molar flow, C is the concentration, Γ is the overall mass transfer coefficient, r is the reaction rate and w is the washcoat mass for each discretization volume [112], [129], [141].

$$Fy_{i,k-1} - Fy_{i,k} - \Gamma_{i,k,0}(C_{i,k,0} - C_{i,k,1}) = 0 \tag{4.1a}$$

$$\Gamma_{i,k,n-1}(C_{i,k,n-1} - C_{i,k,n}) - \Gamma_{i,k,n}(C_{i,k,n} - C_{i,k,n+1}) + \sum^{m} r_{i,k,n,m} w_{k,n} = 0 \tag{4.1b}$$

The mass-transfer coefficients are calculated with Eq. 4.2 where A is the mass transfer area, k_c the external mass transfer coefficient, Δz is the washcoat layer thickness and D_{eff} is the effective diffusivity. The adsorbed species, θ are described by Ordinary Differential Equations (ODEs), and they define the catalyst dynamics. Each ODE includes the reactions involved for each adsorbed species, and it is solved at each washcoat layer for each tank (Eq. 4.3), with N as the total amount of sites in the discretization volume.

$$\Gamma_{i,k,0} = \frac{A_{w,k}}{1/k_{c,k} + 0.5\Delta z_{k,1}/D_{\text{eff},k,1}} \tag{4.2a}$$

$$\Gamma_{i,k,n} = \frac{D_{\text{eff},k,n} A_{w,k}}{0.5\Delta z_{k,n} + 0.5\Delta z_{k,n+1}} \tag{4.2b}$$

$$N_j \frac{d\theta_{i,k,n,j}}{dt} = \sum^{m} r_{i,k,n,m} \tag{4.3}$$

The heat balance follows a similar scheme to the mass balance (Eq. 4.4). It includes heat transfer from the gas phase to the catalyst surface and heat accumulation in the monolith due to convection, conduction, and the heat of reactions. However, for the heat balance, the washcoat is not discretised, which helps convergence and reduces computing time. In Eq. 4.4, C_p is the gas heat capacity, h is the convective heat transfer coefficient, q is the conductive heat transfer coefficient, m_s is the catalyst mass, and ΔH is the heat of reaction.

$$FC_p T_{g,k-1} - FC_p T_{g,k} - h_k A_{k,0}(T_{g,k} - T_{s,k}) = 0 \tag{4.4a}$$

$$m_{s,k} C_{p,s} \frac{dT_{s,k}}{dt} = h_k A_{k,0}(T_{g,k} - T_{s,k}) - A_s(q_{k+1} - q_k) + \sum^{m} r_{i,k,n,m} w_{k,n}(-\Delta H_m) \tag{4.4b}$$

A schematic of how the discretisation is handled in the 1+1D SCM method is shown in Fig. 4.1.

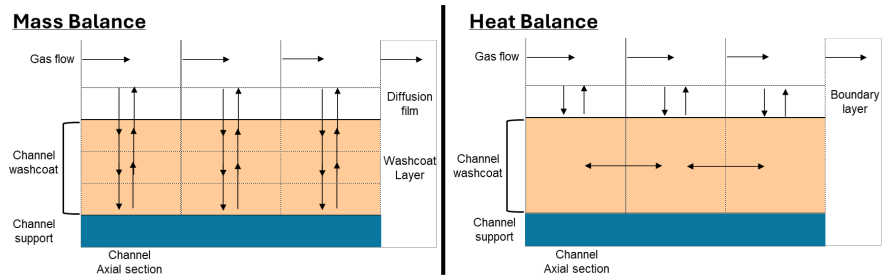

Figure 4.1: Discreatization scheme for the mass and heat balance on the 1+1D SCM method.

4.2 Overview of Kinetic Modelling Approaches

Kinetic models are needed when reactions are involved, which is the case for catalysts used in emission after-treatment systems. These models must be fast to evaluate when running transient simulations, but they also need to describe surface chemistry accurately across a wide operating range. Kinetic models can be as simple as power-law expressions (global kinetics) or as detailed as mechanistic models that include the relevant reaction steps. Both approaches are useful for understanding catalyst behavior.

The simplest kinetic model, the power-law model, can be expressed as Eq. 4.5.

$$r = k(T) \prod_i a_i^{n_i} \tag{4.5}$$

Where a is an activity-based variable such as concentration, pressure, or molar fraction, n_i is the reaction order, and k is the temperature-dependent reaction rate constant. Power-law models lump multiple reactions in a mechanism into a single global expression, and in some cases they can be a good first approximation for modeling [117], [142].

The reaction order can be seen as the local log-sensitivity of the reaction rate with respect to species i, as shown in Eq. 4.6.

$$n_i = \left(\frac{\partial \ln r}{\partial \ln a_i}\right)_{T_{cte}} \tag{4.6}$$

The reaction orders can be non-integer or negative (inhibition), capturing effects such as adsorption, oxidation, and competition for surface coverage, which are not reflected by stoichiometry. Additionally, the reaction rate constant $k(T)$ accounts for temperature dependence through the Arrhenius law, as in Eq. 4.7.

$$k(T) = A \exp\left(\frac{-E_a}{RT}\right) \tag{4.7}$$

where A is the pre-exponential factor, related to collision frequency and entropic effects at the molecular scale, and E_a is the activation energy (energy barrier) for the reaction to occur, which makes the rate sensitive to temperature [117], [118].

In power-law kinetics, inhibition can be included in two ways: by using a negative reaction order ($r \propto C^{-n}$), or by adding an inhibition factor in the denominator, as in Eq. 4.8. The former becomes problematic at zero concentration because the expression is not defined, while the latter is continuous and often more realistic, since the reaction rate is highest when the inhibitor concentration is zero.

$$r = \frac{k(T) \prod_i a_i^{n_i}}{1 + K_{inh} C_{inh}^{m_i}} \tag{4.8}$$

Because power-law kinetics lump reaction steps, they hide the dynamics of surface species. If an adsorbed species accumulates, its surface coverage becomes a state variable that governs catalyst dynamics. In mechanistic models, detailed kinetics explicitly describe the mass balance for adsorbed species using steady-state equations or ODEs [129], [143].

Beyond power-law models, two common kinetic forms are Langmuir –Hinshelwood (LH) and Eley–Rideal mechanisms. These typically represent inhibition through terms in the denominator, which is often more realistic. In a LH model, the reaction occurs between two adsorbed species, while in the Eley–Rideal mechanism the reaction occurs between one adsorbed species and one gas-phase species [143]. Table 4.1 shows the reactions involved for both models.

Langmuir-Hinshelwood	Eley-Rideal
$A(g) + * \rightleftharpoons A*$	$A(g) + * \rightleftharpoons A*$
$B(g) + * \rightleftharpoons B*$	$A* + B(g) \rightleftharpoons AB*$
$A* + B* \rightleftharpoons AB* + *$	$AB* \rightleftharpoons AB(g) + *$
$AB* \rightleftharpoons AB(g) + *$	
$r \propto \theta_A \theta_B$	$r \propto \theta_A C_B$

Table 4.1: LH and Eley-Rideal Reaction mechanisms [143], [144]

For these models, several assumptions can simplify the formulation: a fixed site density ($\sum \theta_j = 1$), the surface reaction is the rate-limiting step, and adsorption/desorption can be assumed to be at equilibrium. Even with these assumptions, LH and Eley–Rideal models are more detailed than power-law kinetics because they include adsorption/desorption steps that define catalyst dynamics. Still, some important behavior may be missing, for example, the redox nature of an active site involved in the reaction.

A redox (oxidation–reduction) cycle includes changes in the catalyst oxidation state. A reaction step can consume oxygen from an active site, and a regeneration step is then needed to re-oxidize the site using oxygen from the gas phase [142]. This concept is captured by the Mars–van Krevelen mechanism, which is described in Table 4.2.

Redox reaction scheme	Redox reaction rate
Cat_{ox}+reductant $\rightarrow$ product +Cat_{red}	$r_{red} = k_{red} C_{red} \theta_{ox}$
$\text{Cat}_{red} + 0.5\text{O}_2 \rightarrow \text{Cat}_{ox}$	$r_{ox} = k_{ox} C_{ox} \theta_{red}$
With $\theta_{ox} = \frac{S_{ox}}{S_{tot}}$, $\theta_{red} = 1 - \theta_{ox}$	

Table 4.2: Redox Reaction mechanisms. [142]

The redox cycle has similarities to adsorption, since the oxidized and reduced catalyst states can be treated as sites that interconvert under a fixed total site density. In the simplest case, only two site states are considered on the catalyst surface.

Additionally, kinetic models can include features that increase the level of detail in how catalyst behavior is described. These features are listed below:

Multi-site kinetics: The catalyst have sites with different properties that have parallel reaction pathways, like adsorption/desorption (Table 4.3) [145].

Site 1	Site 2
$1 = \theta^{(1)}_{free} + \sum \theta^{(1)}_i$	$1 = \theta^{(2)}_{free} + \sum \theta^{(2)}_i$
$r^{tot} = r^{(1)} + r^{(2)}$	

Table 4.3: Multi-site kinetics

Non-Langmuir adsorption: This is used when adsorption is not ideal Langmuir, with coverage dependent properties, lateral interactions or surface heterogeneity). These models provide new definitions on the energy of desorption. Some of the non-Langmuir adsorption models are [144], [146], [147]:

- Freundlich: Used for multilayer adsorption with non-homogenous distribution of adsorption energies. However, it has a limited range of application since does not have a plateau at high gas concentrations. The activation energy for desorption is estimated as $E_d = E^o_d \exp(-\alpha\theta_i)$.
- Temkin: The desorption energy decreases linearly as the coverage increases due to increased interaction on adjacent species. It is commonly used for NH_3 adsorption on vanadium-based SCR catalysts. However, the empirical parameter, α, lacks physical significance when the vanadium concentrations are low. For the standard Temkin model, the desorption energy is estimated as $E_d = E^o_d(1 - \alpha\theta_i)$, while for the modified Temkin model, the desorption energy is estimated as $E_d = E^o_d.(1 - \alpha\theta^{\beta}_i)$. Table 4.4 shows parameters for NH_3 adsorption in a vanadium-based SCR catalyst using a Temkin model [148].

	V_2O_5/TiO_2	V_2O_5-WO_3/TiO_2	Commercial
k_a^o (m^3/mol.s)	0.820	0.487	33.870
k_d^o (1/s)	3.67E+06	2.67E+05	2.20E+06
E_d^o (kcal/mol)	25.8	22.9	23.0
α	0.310	0.405	0.256

Table 4.4: NH_3 adsorption Temkin model parameters for a vanadium-based SCR catalyst. [148]

- Empirical dual site coverage: An empirical description on the des-

orption energy, Ed, is given by Lietti at. al. [148], which considers a coverage dependency on the desorption energy with the existence of two adsorption sites with different desorption energies. This description gives better estimation on NH_3 adsorption for a vanadium-based SCR on low temperatures and fast transients. The desorption energy is estimated as $E_d = E_d^o + B\tanh(-\alpha\theta_i + A)$.

Lattice/ kinetic Monte Carlo (kMC) surface kinetics: Stochastic simulation of surface events on a lattice to capture spatial correlations, site ensembles, etc, where the mean-field theory fails. This is a key framework to reduce the scale gap between molecular behavior and application, since it is coupled with first-principle calculations. However, it is computing expensive for deployment in automotive applications [149].

Apparent kinetics with reaction-diffusion: In catalyst monoliths, internal diffusion and external mass transfer could control the observed reaction rate. This can be accounted by an effectiveness factor correction, Eq. 4.9, where η is an effectiveness factor based on the Thiele (ϕ) modulus, or by coupling mass transfer into the catalyst mass balance [134].

$$r_{obs} = \eta(\phi) r_{\text{intr}} \tag{4.9}$$

Deactivation / aging kinetics: Introduce an activity factor evolving on time to account for catalyst aging which reduce activity or increase side reactions (Eq. 4.10a and 4.10b) [150].

$$r = a(t) r_{\text{fresh}} \tag{4.10a}$$

$$\frac{da}{dt} = -k_d(T, \text{exposure}) a^m \tag{4.10b}$$

This set of tools can be combined to describe reaction mechanisms. The appropriate level of complexity depends on the goals of the model and the level of detail required, while still using assumptions that simplify the formulation without losing the main features that define catalyst dynamics. Complex models are challenging to calibrate because reactions are often correlated, and adsorbed species are typically inferred indirectly from gas-phase measurements in a flow reactor. This usually requires careful design of experiments

to isolate key information for each step and allow parameter estimation with narrow confidence intervals.

Power-law Kinetics for H_2-SCR Catalysts

In this thesis, studies on support effects for Pd-based H_2-SCR catalysts were performed by measuring H_2-SCR activity under different H_2/NO ratios and water concentrations. Four supports were considered: metal oxides such as Al_2O_3 and TiO_2, and zeolites such as BEA and SSZ-13. Experiments in a gas flow reactor at temperatures between 130 and 250°C showed the formation of N_2 and N_2O for the Al_2O_3, BEA, and SSZ-13 supports, and N_2, N_2O, and NH_3 for the TiO_2 support. In addition, a water inhibition effect was observed under the experimental conditions. Based on these results, a simplified reaction scheme was proposed (Reactions VI to IX).

$$\text{R1:} \quad \mathrm{NO + H_2 \longrightarrow H_2O + 0.5\,N_2} \tag{VI}$$

$$\text{R2:} \quad \mathrm{H_2 + 0.5\,O_2 \longrightarrow H_2O} \tag{VII}$$

$$\text{R3:} \quad \mathrm{2\,NO + H_2 \longrightarrow N_2O + H_2O} \tag{VIII}$$

$$\text{R4:} \quad \mathrm{2\,NO + 5\,H_2 \longrightarrow 2\,NH_3 + 2\,H_2O} \tag{IX}$$

To gain insight into the relationship between concentration, temperature, and reaction rate, the reactions were modelled using power-law kinetics with an Arrhenius-type temperature dependence for the reaction rate constant. Water inhibition was included as a power-law term in the denominator. The kinetic expressions for these reactions are presented in Table 4.5. The reaction order with respect to oxygen was assumed to be one, and the reaction for N_2O formation was assumed not to be inhibited by water, based on the experimental data.

This kinetic model was coupled to a single-channel catalyst model (SCM) with external mass transfer, as presented in Eq. 4.15, where v is the superficial gas velocity, $\bar{c}$ is the bulk gas concentration, C is the surface concentration, a_p is the washcoat surface per catalyst volume, and ν is the stoichiometric coefficient.

Table 4.5: Rate expressions for Reaction (I) to (IV).

$$r_1 = \frac{A_1 \exp\left(\frac{-E_{a,1}}{RT}\right) C_{\mathrm{NO}}^{\alpha_1} C_{\mathrm{H_2}}^{\alpha_2}}{1 + A_1^I \exp\left(\frac{-E_{a,1}^I}{RT}\right) C_{\mathrm{H_2O}}^{\alpha_3}} \tag{4.11}$$

$$r_2 = \frac{A_2 \exp\left(\frac{-E_{a,2}}{RT}\right) C_{\mathrm{H_2}}^{\beta_1} C_{\mathrm{O_2}}}{1 + A_2^I \exp\left(\frac{-E_{a,2}^I}{RT}\right) C_{\mathrm{H_2O}}^{\beta_2}} \tag{4.12}$$

$$r_3 = A_3 \exp\left(\frac{-E_{a,3}}{RT}\right) C_{\mathrm{NO}}^{\delta_1} C_{H_2}^{\delta_2} \tag{4.13}$$

$$r_4 = \frac{A_4 \exp\left(\frac{-E_{a,4}}{RT}\right) C_{\mathrm{NO}}^{\gamma_1} C_{\mathrm{H_2}}^{\gamma_2}}{1 + A_4^I \exp\left(\frac{-E_{a,4}^I}{RT}\right) C_{\mathrm{H_2O}}^{\gamma_3}} \tag{4.14}$$

$$v \frac{d\overline{c}_{\mathrm{NO}}}{dz} = r_{\mathrm{NO}} = -r_1 - 2r_3 - 2r_4 \tag{4.15a}$$

$$v \frac{d\overline{c}_{\mathrm{H_2}}}{dz} = r_{\mathrm{H_2}} = -r_1 - r_2 - r_3 - 5r_4 \tag{4.15b}$$

$$v \frac{d\overline{c}_{\mathrm{N_2O}}}{dz} = r_3, \quad v \frac{d\overline{c}_{\mathrm{NH_3}}}{dz} = 2r_4 \tag{4.15c}$$

$$a_p k_{m,i}(\overline{c}_i - C_i) = -\sum_j \nu_{i,j} r_j, \quad i = \mathrm{NO}, \mathrm{H_2} \tag{4.15d}$$

The catalyst model was assumed to be isothermal, radially homogeneous, and solved under steady-state conditions, since the evaluation of species concentrations along the length of the catalyst sample is the objective of this study. External mass transfer was considered using the Sherwood correlation given in Eq. 4.16 [132], with an asymptotic Sherwood number for squared channels, $Sh_a = 3$, and a dimensionless axial coordinate, z_{Sh} defined as $z_{Sh} = zD_i/(vd_o^2)$ with D_i as molecular diffusivity, and d_o as the open channel width.

$$Sh = Sh_a + 6.874(1000 z_{Sh})^{-0.488} \exp(-57.2 z_{Sh}) \tag{4.16}$$

The parameter estimation workflow was performed using an objective function that minimizes the difference between the experimental and modelled outlet concentrations. These differences were normalized by the variance and adjusted for the number of data points for each gas, as shown in Eq. 4.17. This approach ensures equal contribution from all species and experiments, facilitating convergence and improving the use of experimental information.

$$\min(F) = \min\left(\sum_{i=1}^{G} \frac{N_i - 1}{N_i} \sum_{j=1}^{N_i} \frac{(y_{i,j}^{exp} - y_{i,j}^{mod})^2}{\sigma_i^2} \right) \tag{4.17}$$

The optimization workflow used in this study is described in Fig. 4.2.

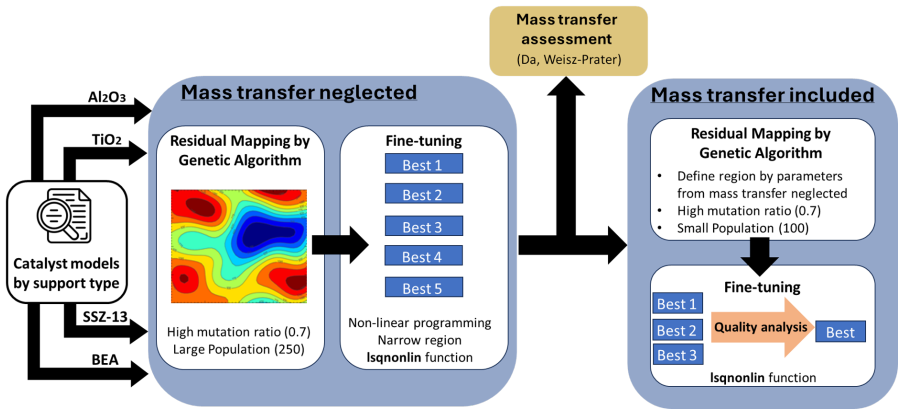

Figure 4.2: Parameter optimization workflow developed for this study.

Initially, a genetic algorithm was used to map the residual space and avoid convergence to local optima. The genetic algorithm was specified with a high mutation ratio, ensuring that each generation includes a population of random candidates outside the current best solutions tracked by the algorithm.

Table 4.6 presents the kinetics parameters for the catalyst models developed for each H_2-SCR sample.

Table 4.6: Kinetic parameters for catalyst models for all the studied H_2-SCR samples.

	Pd/Al_2O_3	Pd/TiO_2	Pd/BEA	Pd/SSZ-13
A_1 (*)	2.13E+09	1.22E+10	1.02E+16	4.11E+13
Ea_1 (J/mol)	62100	56100	107000	79700
α_1	1.0	2.1	0.8	1.7
α_2	1.2	0.4	1.3	1.6
A_1^I (**)	3.9	1.1	0.8	0.5
Ea_1^I (J/mol)	5850	227	209	255
α_3	1.1	0.9	2.5	1.0
A_2 (*)	1.29E+16	2.41E+18	3.38E+17	2.25E+21
Ea_2 (J/mol)	128000	146000	121000	150000
β_1	1.5	1.3	1.1	2.8
A_2^I (**)	3.1	0.3	0.1	6.2
Ea_2^I (J/mol)	7070	1310	83100	14300
β_2	0.4	2.0	0.2	3.5
A_3 (*)	1.26E+18	2.46E+13	1.30E+16	1.36E+10
Ea_3 (J/mol)	127000	87000	119000	63400
δ_1	1.6	2.1	0.8	1.8
δ_2	2.7	0.6	1.2	1.1
A_4 (*)		3.11E+11		
Ea_4 (J/mol)		97300		
γ_1		0.1		
γ_2		1.2		
A_4^I (**)		138		
Ea_4^I (J/mol)		26200		
γ_3		2.2		
adj-R^2	**0.93**	**0.96**	**0.98**	**0.93**
AIC	**-964**	**-974**	**-1190**	**-1040**

REMARKS:
(*) Units of pre-exponential $[m^3]^{\sum z-1}[mol]^{1-\sum z}[s]^{-1}$ z=Rxn order
(**) Units of inhibition pre-exponential $[m^3]^{\sum z}[mol]^{-\sum z}$

NH_3 Adsorption Model on Vanadium-based SCR Catalysts

NH_3 adsorption models for a vanadium-based SCR catalyst were defined using steady-state data, represented by the adsorption isotherms. Under these

conditions, the system is at equilibrium, so mass transfer does not need to be considered. This allowed the development of a modelling framework to evaluate several NH_3 adsorption model structures. The framework is based on adsorption mechanisms aimed at capturing the complexity and diversity of a vanadium-based SCR catalyst.

This catalyst is known to have multiple NH_3 adsorption sites with different dynamics, and a model should be able to capture this diversity and its effect on NH_3 storage. As a result, the total NH_3 storage in the catalyst is the sum of the contributions from all adsorption sites, as shown in Eq. 4.18.

$$q_{\mathrm{NH_3}} = \sum_{j=1}^{M} N_j \theta_j \tag{4.18}$$

Each site can follow different mechanisms depending on its interaction with NH_3 and water. For this study, the mechanisms are presented in Table 4.7, which shows how NH_3 and water may affect each adsorption site. In total, five mechanisms were considered in the Langmuir adsorption models.

- **Simple Adsorption:** Only NH_3 adsorbs on the site.
- **Site Activation:** The site is activated before adsorbing NH_3. The activation follows an Arrhenius-type dependence on temperature.
- **Competitive Adsorption:** Water and NH_3 compete for adsorption sites.
- **Water Activation:** For NH_3 adsorption to occur, the site needs to be activated by water.
- **Site Duplication:** Water duplicates adsorption sites for NH_3.

To evaluate all possible adsorption models that can result from combining mechanisms across adsorption sites, a systematic procedure was used. Candidate models were created by combining adsorption mechanisms ($r = 5$) and assuming the catalyst could have up to six types of adsorption sites (M=1,...,6). This results in 461 possible adsorption models from the combinations in Eq. 4.19.

$$C_{M,r} = \binom{M + r - 1}{r - 1} = \frac{(M + r - 1)!}{(M - 1)! r!} \tag{4.19}$$

Table 4.7: Site specific adsorption mechanisms forming the building blocks of the adsorption model.

Mechanism			Coverage
A	Simple adsorption	$S + NH_3 \rightleftarrows S-NH_3$	$\theta = \frac{K_c C_{NH_3}}{1+K_c C_{NH_3}}$
B	Site activation	$S \rightleftarrows S^*$ $S^* + NH_3 \rightleftarrows S^*-NH_3$	$\theta = \frac{K_{c1}K_{c2}C_{NH_3}}{1+K_{c1}+K_{c2}C_{NH_3}}$
C	Competitive adsorption	$S + NH_3 \rightleftarrows S-NH_3$ $S + H_2O \rightleftarrows S-H_2O$	$\theta = \frac{K_{c1}C_{NH_3}}{1+K_{c2}C_{H_2O}+K_{c1}C_{NH_3}}$
D	Water activated adsorption	$S + H_2O \rightleftarrows S^*$ $S^* + NH_3 \rightleftarrows S^*-NH_3$	$\theta = \frac{K_{c1}K_{c2}C_{NH_3}C_{H_2O}}{1+K_{c1}C_{H_2O}+K_{c1}K_{c2}C_{NH_3}C_{H_2O}}$
E	Site duplication by water	$S + H_2O \rightleftarrows 2\,S^*$ $2\,S^* + 2\,NH_3 \rightleftarrows 2\,S^*-NH_3$	$\theta = \frac{K_{c1}K_{c2}C_{NH_3}C_{H_2O}}{1+2K_{c1}C_{H_2O}+2K_{c1}K_{c2}C_{NH_3}C_{H_2O}}$

Fig. 4.3 shows the concept of how the model structures are generated, and the parameters to be estimated are defined for the optimization task.

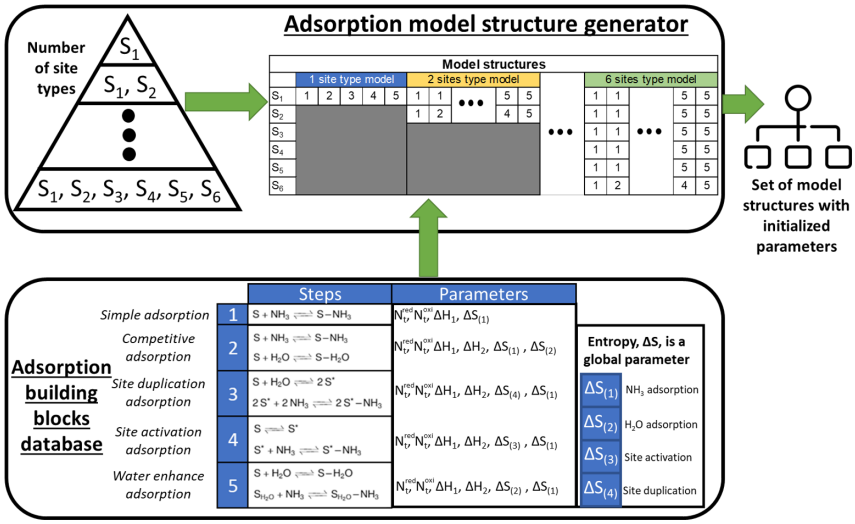

Figure 4.3: Adsorption model structure generator.

The modelling framework for model creation and parameter estimation is shown in Fig. 4.4. Two workflows were used depending on the catalyst state, which allows parameter estimation for both the oxidized and reduced datasets. At each step in the workflow, objective functions with increasing complexity were used. In the first step, around 33,000 scenarios were evaluated based on the objective function in Eq. 4.20. Then, the best 18,000 models (about 50%) were chosen for the second step using Eq. 4.21, and in the third step, 9,000 scenarios were evaluated using the objective function in Eq. 4.22.

$$LSS = \sum_{i=1}^{n} (q_{mod,i} - q_{exp,i})^2 \tag{4.20}$$

$$MSD = \frac{1}{n-p} \sum_{i=1}^{n} \left[\frac{q_{exp,i} - q_{mod,i}}{q_{exp,i}} \right]^2 \tag{4.21}$$

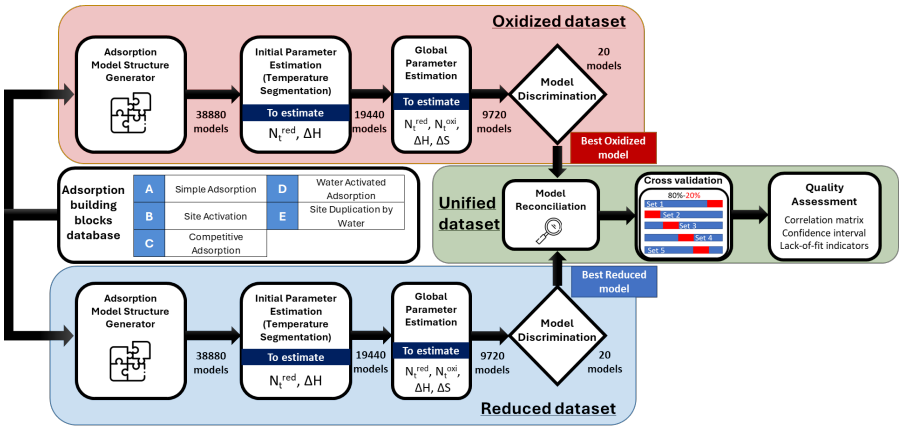

Figure 4.4: Data-driven modeling framework for evaluation and discrimination of NH_3 adsorption models.

$$MST = \frac{1}{n-p}\left[\lambda \sum_{i=1}^{n} \frac{\left[q_{exp,i} - q_{mod,i})\right]^2}{q_{exp,i}^2} + (1-\lambda) \sum_{j=1}^{m} \frac{\left[\alpha_{exp,j} - \alpha_{mod,j})\right]^2}{\alpha_{exp,j}^2}\right] + \ln\left[\lambda \sum_{i=1}^{n} \frac{\left[q_{exp,i} - q_{mod,i})\right]^2}{q_{exp,i}^2} - (1-\lambda) \sum_{j=1}^{m} \frac{\left[\alpha_{exp,j} - \alpha_{mod,j})\right]^2}{\alpha_{exp,j}^2}\right]^2 \tag{4.22}$$

Finally, model discrimination and unification of oxidized and reduced parameters were performed using the Akaike Information Criterion (AIC) as the objective function, with fine-tuning by cross-validation, Eq. 4.23. In these equations, n is the dataset size, p is the number of parameters, α is the slope of the adsorption isotherm.

$$AIC = n * \log\left(\frac{1}{n}\sum_{i=1}^{n}\left[\frac{q_{exp,i} - q_{mod,i}}{q_{exp,i}}\right]^2\right) + 2(p+1) \tag{4.23}$$

The result from this workflow is a five-site NH_3 adsorption model with the following mechanisms: one site with simple NH_3 adsorption, three sites with competitive adsorption with water, and one site where water activates the site

Table 4.8: NH_3 adsorption model mechanisms structure and parameters.

	S_j-N^{red} (mol/g_{wash})	S_j-N^{oxi} (mol/g_{wash})	Mechanism		ΔH_{ads} (kJ/mol)	ΔS_{ads} (J/mol.K)
Site 1	3.26E-05 +/- 6.86E-07	2.92E-05 +/- 5.94E-07	A	$S + NH_3 \rightleftharpoons S-NH_3$	-109.91 +/- 7.6	-173.58 +/- 2.8
Site 2	2.03E-05 +/- 5.10E-07	4.85E-05 +/- 1.05E-06	C	$S + NH_3 \rightleftharpoons S-NH_3$	-155.25 +/- 1.2	-173.58 +/- 2.8
				$S + H_2O \rightleftharpoons S-H_2O$	-91.73 +/- 1.2	-100.59 +/- 1.7
Site 3	2.90E-05 +/- 5.54E-07	2.58E-05 +/- 1.08E-06	C	$S + NH_3 \rightleftharpoons S-NH_3$	-127.98 +/- 9.4	-173.58 +/- 2.8
				$S + H_2O \rightleftharpoons S-H_2O$	-130.08 +/- 4.9	-100.59 +/- 1.7
Site 4	4.29E-05 +/- 8.20E-07	4.18E-05 +/- 5.94E-07	C	$S + NH_3 \rightleftharpoons S-NH_3$	-95.56 +/- 6.3	-173.58 +/- 2.8
				$S + H_2O \rightleftharpoons S-H_2O$	-49.03 +/- 1.0	-100.59 +/- 1.7
Site 5	1.89E-05 +/- 4.46E-07	4.80E-05 +/- 1.05E-06	D	$S + H_2O \rightleftharpoons S-H_2O$	-60.96 +/- 2.3	-100.59 +/- 1.7
				$S_{H_2O} + NH_3 \rightleftharpoons S_{H_2O}-NH_3$	-153.56 +/- 6.4	-173.58 +/- 2.8

for NH_3 to adsorb. Table 4.8 shows the parameters for the selected model.

Fig. 4.5 shows the fitting performance for the adsorption isotherms under different experimental conditions.

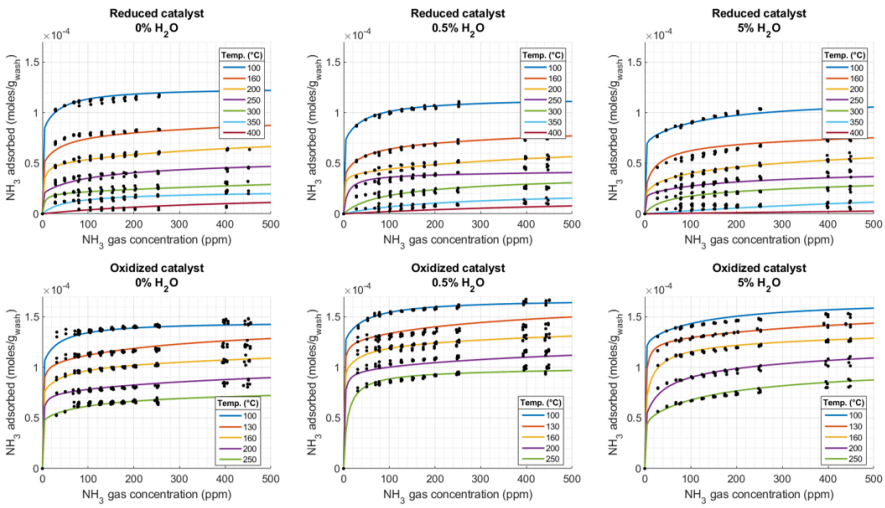

Figure 4.5: NH_3 adsorption model fitting performance for the experimental adsorption isotherms. Model values (continuous line) and experimental data (black circles).

4.3 Steady-state Formulation and Thermodynamic Aspects

The adsorption isotherms extracted from experiments under proper steady-state conditions represent an equilibrium state where the adsorption and desorption rates are balanced, together with mass-transfer effects inside the catalyst. This equilibrium is influenced by temperature, concentration, and the catalyst material. It can be described thermodynamically through the enthalpy and entropy changes of adsorption, ΔH_{ads} and ΔS_{ads}. These parameters have strong physical meaning because they relate to the adsorption strength of the molecule and how the molecules are arranged on the surface [151].

For a simple adsorption system where the gas compound A is adsorbed on a surface site S, the adsorption kinetics and its steady-state are defined in Fig. 4.6.

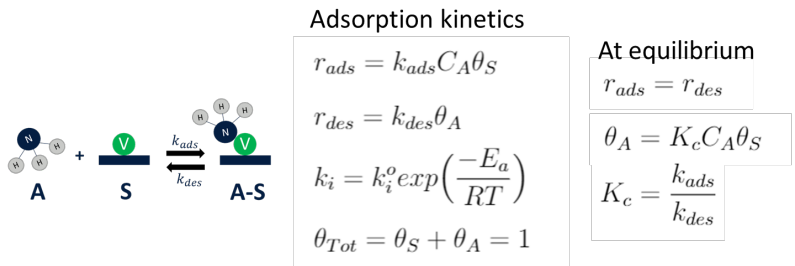

Figure 4.6: Adsorption kinetics and equilibrium model. Taken from [152]

At equilibrium, the equilibrium constant, K_c, can be defined as the ratio between the adsorption and desorption rate constants, which are related to the gas concentration and reaction orders, as shown in Eq. 4.24.

$$K_c = \prod_{i=1}^{n} C_i^{\gamma_i} \tag{4.24}$$

The equilibrium constant, K_c, can be related to the thermodynamic equilibrium constant,K, as shown in Eq. 4.25, assuming ideal gases, with γ as reaction order.

$$K = K_c\left(\frac{RT}{P_{ref}}\right)^{\delta}$$
$$\delta = \sum \gamma_i \tag{4.25}$$

This allows us to relate the thermodynamic equilibrium constant to the Gibbs free energy (Eq. 4.26), which can be expressed in terms of the enthalpy and entropy changes of adsorption, ΔH_{ads} and Δs_{ads}, as presented in Eq. 4.27 and 4.28.

$$RT\ln(K) = -\Delta G \tag{4.26}$$

$$K = exp\left(\frac{-\Delta H_{ads} + T\Delta S_{ads}}{RT}\right) \tag{4.27}$$

$$\Delta G = \Delta H - T\Delta S \tag{4.28}$$

Therefore, a steady-state NH_3 adsorption model can be estimated from adsorption isotherm experiments and thermodynamic parameters that have physical meaning and can be compared to experiments or molecular-scale simulations (DFT). However, this model is not sufficient for transient data, and one step, either adsorption or desorption, needs to be estimated to fully describe the NH_3 adsorption dynamics. This reduces the effort in parameter estimation for transient data because fewer parameters must be fitted. It also narrows the confidence intervals, increasing the relevance of the estimated parameters.

Fig. 4.7 shows how the thermodynamic parameters found in the model compare with values obtained from DFT studies. For NH_3 adsorption, the enthalpies of adsorption vary from -155 to -95 kJ/mol, and for water from -130 to -49 kJ/mol. The values obtained from the model are within the range reported in other studies for vanadium and TiO_2 [105], [116], [153], [154], [155], [156], [157], [158].

4.4 Mass Transfer Analysis and Definition

In catalyst monoliths used in emission after-treatment systems, measurements are typically taken in the bulk gas, not directly at the catalyst surface or inside

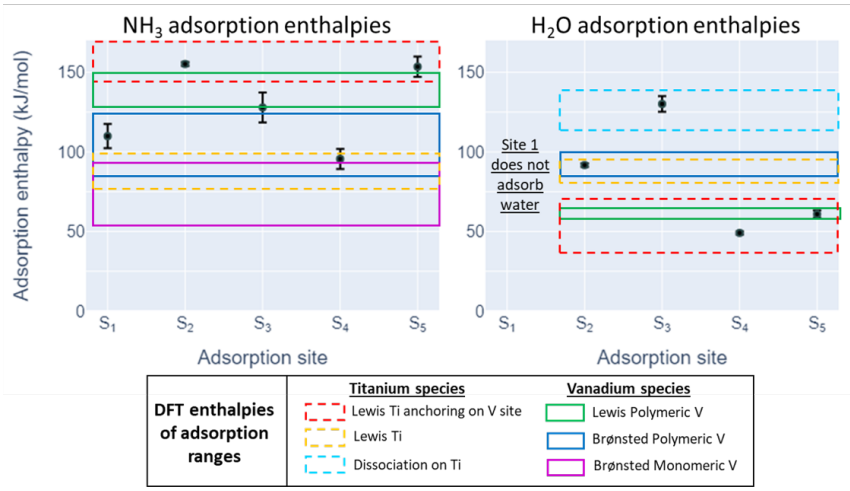

Figure 4.7: Adsorption enthalpy, ΔH_{ads}, comparison between DFT studies for vanadium and titanium clusters, and the model values [105], [116], [153], [154], [155], [156], [157], [158].

the washcoat. Because of this, concentration gradients can exist across the external gas film and/or within the porous washcoat structure. Therefore, the catalytic activity that is measured is often an apparent activity, influenced by mass transfer limitations rather than only by intrinsic reaction kinetics.

There are different ways to evaluate mass transfer effects in a catalyst and to understand how important they are for the model. This can help add simplifications while still maintaining accuracy.

The dimensionless criterion for external mass transfer is the Damköhler number (Da), which relates the observed reaction rate to the external mass transfer, as shown in Eq. 4.29 [117].

$$Da_i = \frac{r_i^{\text{obs}}}{a_p k_{m,i} \overline{c}_i} \tag{4.29}$$

For $Da > 10$, external mass transfer becomes dominant and affects the overall conversion. In this case, the bulk-gas concentration, $\overline{c}_i$, is higher than the surface concentration, C_i, $(\overline{c}_i >> C_i)$. If $Da << 1$, external mass transfer

is negligible and reaction kinetics govern conversion. Values between 1 and 10 suggest a mixed regime where both external mass transfer and reaction kinetics are relevant and should be considered in the model.

The criterion for internal mass transfer is the Weisz–Prater number (N_{WP}), which compares the overall reaction rate with internal diffusion in the porous washcoat, as presented in Eq. 4.30 [117], [142].

$$N_{WP,i} = \frac{r_i^{\text{obs}} d_a^2}{D_{\text{eff},i} C_i} \tag{4.30}$$

For $N_{WP} >> 1$, internal diffusion is limiting and should be included in the model, while for $N_{WP} << 1$, internal diffusion can be neglected. Internal resistance increases as the washcoat thickness increases, so for thinner washcoats, internal diffusion may be neglected.

Mass Transfer limitations in H_2-SCR Catalysts.

For the H_2-SCR catalyst study in this thesis, mass-transfer limitations were evaluated by estimating the Damköhler number for external mass transfer and the Weisz–Prater criterion for internal mass transfer. A reduced kinetic model was used, where NO_x and H_2 conversions were used to calculate the observed reaction rate (r_{obs}). Fig. 4.8 shows these criteria for all catalyst samples under the most severe experimental conditions (H_2/NO = 15, 10% H_2O). For each catalyst, the figure reports the highest value as a function of temperature. In the plot, the Damköhler values are well above 1, while the Weisz–Prater values remain below 1. This indicates that external mass transfer should be included in the model, while internal mass-transfer limitations can be neglected.

Additionally, the full catalyst model was used to evaluate the catalyst regime for all samples based on the bulk concentration (C_b) and the surface concentration (C_s). A C_b/C_s ratio below 1.1 indicates a kinetic regime, values between 1.1 and 10 suggest a mixed regime, and ratios above 10 indicate external mass-transfer limitations [133]. Fig. 4.9 shows the different regimes for H_2/NO = 15 for all samples. At low temperatures, all samples operate in the kinetic regime. As temperature rises, mass transfer resistance becomes increasingly important, shifting the system into a mixed regime where reaction and mass transfer rates are of the same order of magnitude. At the highest temperatures,

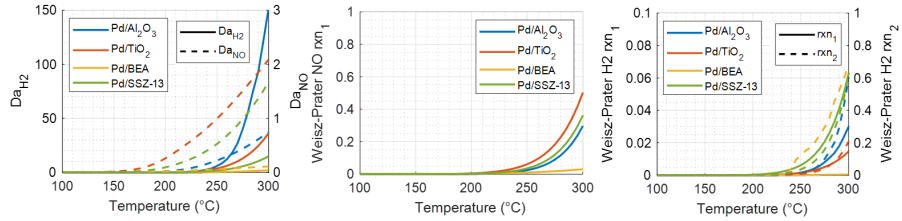

Figure 4.8: Damkohler number (Da) and Weisz-Prater criterion ($N_{WP,i}$) from the apparent reaction rate r_{NO}^{obs} and $r_{H_2}^{obs}$. Left: Da for H_2 (solid line) and NO (dashed line). Middle: N_{WP} for NO. Right: N_{WP} for H_2 from reaction I (solid line) and reaction II (dashed line). The panels show the highest values of Da and $N_{WP,i}$ across the catalyst length as a function of temperature for all catalyst samples. H_2/NO = 15 (H_2 7500 ppm) and 10% H_2O.

mass transfer becomes the dominant limitation. The results also indicate low catalyst utilization because H_2 is largely consumed near the inlet section of the catalyst bed.

Then, focusing on the Pd/TiO_2 sample, an additional study was performed by varying the mass-transfer coefficient to evaluate the effect on NO conversion. Fig. 4.10 shows the results of these simulations. When the mass-transfer coefficient decreases, NO conversion increases at higher temperatures (above 250°C) because more H_2 remains available along the catalyst. Moreover, reduced mass transfer lowers the NH_3 yield while increasing N_2 and N_2O yields. In this case, catalyst utilization improves since H_2 is more evenly available throughout the bed. Overall, mass transfer limitations preferentially suppress faster reactions, which gives an advantage to slower reactions such as NO reduction.

4.5 Improved Mass Transfer Descriptions

The conventional 1+1D single-channel catalyst model (SCM) includes internal mass transfer in the mass balance for the washcoat layer in each discretized tank. Porous diffusion is lumped into a parallel-pore model, including molecular and Knudsen diffusion. This approach is robust and computationally inexpensive. However, it treats diffusion in a generic, global way by assuming homogeneous washcoat properties and that the washcoat is evenly distributed

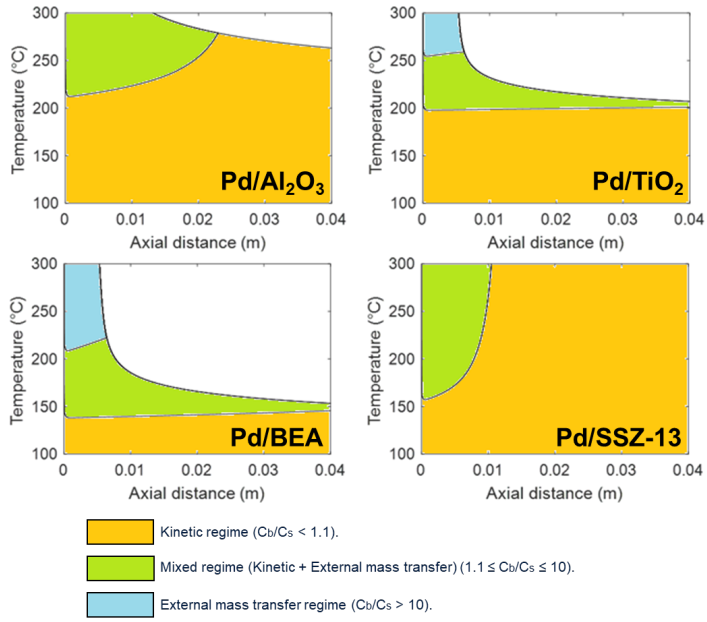

Figure 4.9: Catalyst regimes based on H_2 concentration at different temperatures along the catalyst sample length for all H_2-SCR samples. Inlet gas composition NO=500ppm, H_2=7500ppm, H_2O=5%, O_2=10%. Yellow area = kinetic regime, green = mixed regime, blue = external mass transfer regime, blank = no reactions (H_2 fully consumed).

in the channels. Any deviation from this assumption will be absorbed (or "lumped") into the kinetic parameters, which reduces their physical meaning and validity. This becomes critical when the catalyst has a thick washcoat, has layered functions, operates in strongly diffusion-limited regimes (high temperatures), or when the dynamics are affected by how active sites are distributed.

Monolith catalysts do not have a uniform washcoat distribution in the channels. There are variations in thickness, cracks, and accumulation at the corners, which affect diffusion locally. The effective diffusivity is linked to the pore-size distribution: macro- and mesopores enable gas transport, while micropores increase surface area. Moreover, the properties used to describe the washcoat include mean pore size, tortuosity, and porosity, which are often estimated

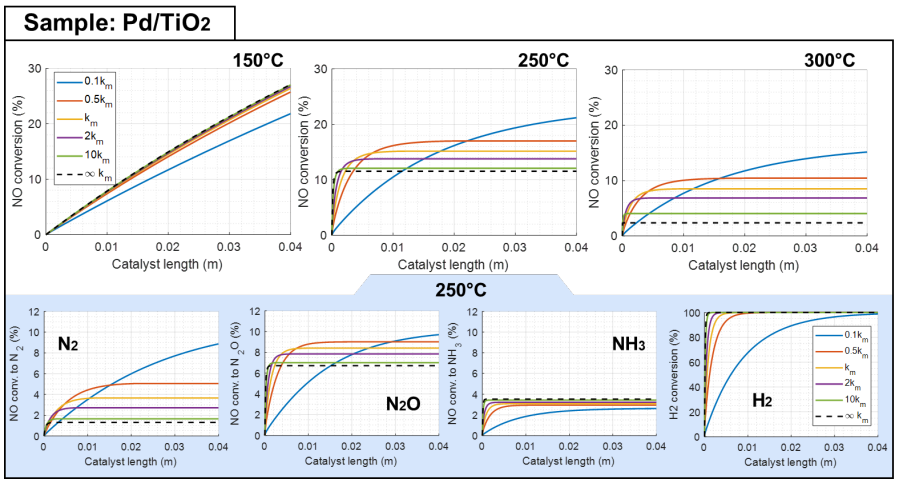

Figure 4.10: Simulated NO conversion on Pd/TiO_2 at 150, 250 and 300°C, and different external mass transfer coefficients, k_m. Inlet gas composition NO=500ppm, H_2=7500ppm, H_2O=5%, O_2=10%. Top row: Total NO conversion. Bottom row: Gas compound conversion at 250°C.

through an optimization task [134], [159], [160]. However, this still does not capture the detailed pore structure of the catalyst.

For the NH_3 adsorption model of a vanadium-based catalyst, internal mass transfer is estimated using Eq. 4.31 [117], where ϵ is washcoat porosity, τ is tortuosity, D is molecular diffusion and D_k is the Knudsen diffusion.

$$D_{\text{eff},i} = \frac{\epsilon/\tau}{D_i^{-1} + D_{k,i}^{-1}} \tag{4.31}$$

Non-squared Channels and Porous Structure

N_2 physisorption and optical microscopy were used to gain more information about the washcoat on the vanadium-based SCR catalyst, where NH_3 adsorption was studied. Fig. 4.11 summarizes the results of the N_2 physisorption experiments. All samples have the same mean pore size (180–190 Å), but they also have a high standard deviation (80–90 Å), which indicates a wide pore size distribution. This is confirmed by the incremental pore size distribution

as a function of pore width (Fig. 4.11(C)). This suggests that using a single mean pore size to estimate internal mass diffusion is an oversimplification, and it can influence NH_3 adsorption dynamics.

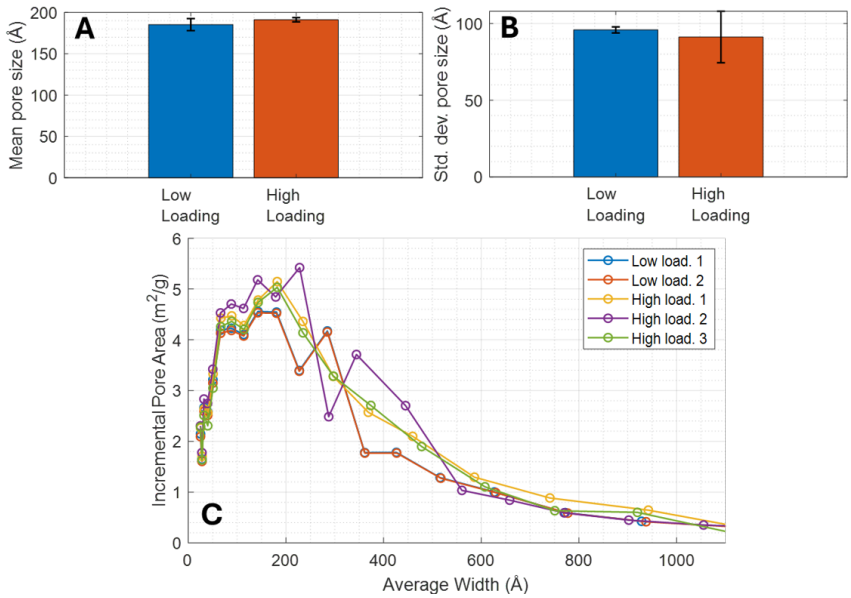

Figure 4.11: Pore characterization by N_2 physisorption. A) Mean pore size, B) Standard deviation for the low and high washcoat loading, C) Incremental pore area (m^2/g) as a function of average width for different samples.

Optical microscopy results (Fig. 4.12) show that the washcoat does not deposit in a way that creates perfectly squared channels. Instead, it forms rounded corners, where the washcoat accumulates at high loadings, and it creates a wavy, square-like pattern at low loading. In addition, cracks are visible at the surface, which could affect the pore size distribution. These effects can help explain the lack-of-fit of the NH_3 adsorption model under specific experimental conditions.

The non-homogeneous nature of the washcoat is proposed to be addressed using two approaches. The first approach considers a variable pore size as a function of washcoat thickness, where the largest pores occur near the surface due to cracks. The second approach introduces two porous regions: a macro-

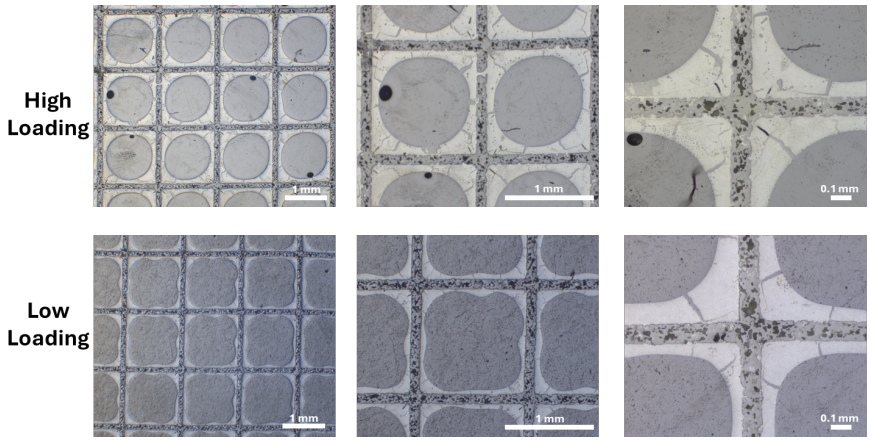

Figure 4.12: Optical microscopy images for the catalyst samples used in this study under different magnification levels.

pore region where gas diffuses and a micropore region where adsorption occurs.

For the first approach, the functions in Eq. 4.32 to 4.34 are proposed to describe the pore size dependence on washcoat thickness. Since a change in pore size also changes the density of adsorption sites, the adsorption and desorption rates are corrected accordingly. In the equations, d_{po}, δ_i, and δ_b are parameters to be found, while $\dot{z}$ is the dimensionless washcoat thickness.

$$\text{Lineal} \quad d_p = d_{po} - d_{po}\delta_i\dot{z} \tag{4.32}$$

$$\text{Exponential} \quad d_p = d_{po}\exp(\delta_i\dot{z}^{\delta_b}) \tag{4.33}$$

$$\text{Plateau} \quad d_p = d_{po} - \frac{\delta_i d_{po}}{1+\exp(-\delta_b(\dot{z}-0.5))} \tag{4.34}$$

For the second approach, the washcoat mass balance is expanded into two coupled equations, as shown in Eq. 4.35a for the macropore region, Γ, and Eq. 4.35b for the micropore region, φ. These two equations are applied to each washcoat layer in the catalyst model.

$$\Gamma_{NH_3,k,n-1}(C_{NH_3,k,n-1}-C_{NH_3,k,n})-\Gamma_{NH_3,k,n}(C_{NH_3,k,n}-C_{NH_3,k,n+1})+\varphi_{NH_3,k,n}(C_{NH_3,k,n}-C^{micro}_{NH_3,k,n})=0 \tag{4.35a}$$

$$\varphi_{NH_3,k,n}(C_{NH_3,k,n}-C^{micro}_{NH_3,k,n}) + \sum^{m} r_{NH_3,k,n,m} w_{k,n} = 0 \tag{4.35b}$$

To include the non-squared geometry in the 1+1D Single Channel Model (SCM) framework, a new discretization scheme is proposed. In this scheme, one tank is split into three sub-tanks with different washcoat thicknesses. All sub-tanks interact through the gas-phase mass balance, and a parameter, α, is defined as a weighting factor between the three sub-tanks. This parameter distributes the total washcoat loading while fulfilling the overall washcoat balance across the catalyst. One sub-tank uses the nominal thickness calculated from the overall washcoat loading, while the other two use a +/- 10% variation around the nominal washcoat thickness.

$$Fy_{NH_3,k-1} - Fy_{NH_3,k} - \sum^{i} \alpha_i \Gamma_{NH_3,k,0}(C_{NH_3,k,0} - C_{NH_3,k,1}) = 0 \tag{4.36}$$

The discretization scheme, including the three sub-tanks and their interactions, is shown in Fig. 4.13. This approach increases the number of mass balance equations by a factor of three, but it is still a small modification to the conventional 1+1D SCM framework.

A modelling framework was developed to estimate the parameters of the proposed catalyst models. The framework is shown in Fig. 4.14 and includes three stages. In the first stage, a genetic algorithm was used to explore the objective function region. The Genetic Algorithm (GA) used a high mutation rate, few generations, and a large population. In this stage, the model was first calibrated using the dry dataset, excluding parameters related to water. Then, the wet datasets (0.5% and 5% water) were used to calibrate the water-related parameters.

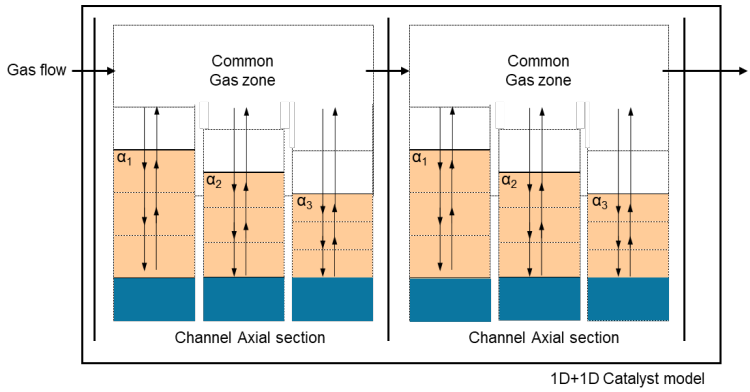

Figure 4.13: Discretization scheme for the 1D+1D catalyst model with three different washcoat thicknesses distributed by the parameter α_i at each axial section.

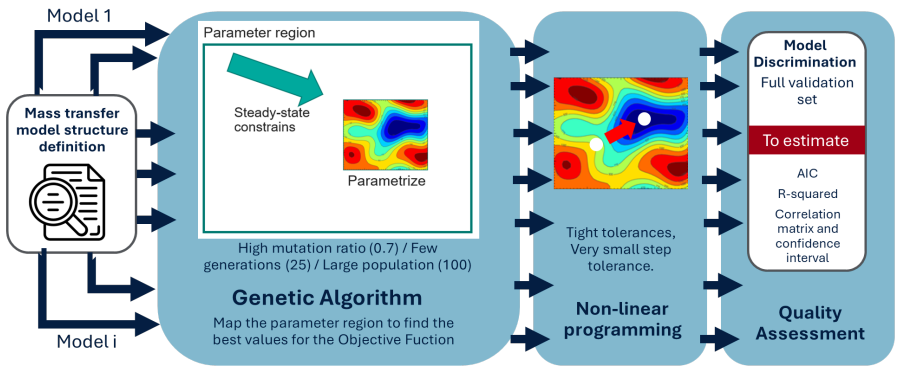

Figure 4.14: Parameter optimization workflow developed for this study.

The second stage is a global optimization step, where fine-tuning is performed under tight constraints using the combined dataset. The third stage uses a similar optimization approach, but with a different objective function to improve convergence and fitting performance. The objective function is given in Eq. 4.37 and includes normalized residuals and normalized cumulative residuals. These are weighted (w) by three factors: measurement uncertainty, increased weight during transient periods, and a dynamic weighting where the weight increases as a function of time.

$$res_{comp} = \frac{y_{exp} - y_{mod}}{\max(y_{exp}) - \min(y_{exp})} \tag{4.37a}$$

$$acc_{exp} = \int (y_{in} - y_{exp})dt \tag{4.37b}$$

$$acc_{mod} = \int (y_{in} - y_{mod})dt \tag{4.37c}$$

$$res_{acc} = \frac{acc_{exp} - acc_{mod}}{\max(acc_{exp}) - \min(acc_{exp})} \tag{4.37d}$$

$$\min(F) = \min\left(\sum \omega res_{comp}^2 + \sum \omega res_{acc}^2\right) \tag{4.37e}$$

Model parameters for the different models (pore size definitions and non-squared channels) are presented in Table 4.9.

Fig. 4.15 shows the NH_3 outlet concentration during the adsorption experiments at different water concentrations at 100°C for the oxidized catalyst. A zoomed view is provided in Fig. 4.16 to highlight differences in fitting performance between the models. It is worth mentioning how the single d_p model, which is the conventional 1+1D SCM model, differs from the other models with the lowest fitting performance.

Fig. 4.17 shows pore size as a function of washcoat thickness for the catalyst models. All models produced results of the same order of magnitude, which, given the unconstrained nature of the optimization, supports the validity of the new strategies for describing non-homogeneous washcoats.

The effect of including non-squared channels is shown in Fig. 4.18, where the best-performing model (Plateau d_p) is compared for squared and non-squared channel geometries. This improvement is smaller than the improvement from the pore size definition. Nevertheless, it is relevant at high temperatures and low NH_3 concentrations. As a result, the model improves its fitting performance over a wider experimental range.

To compare model fitting performance, Table 4.10 presents the quality indicators R-squared and AIC for the different models. The conventional 1+1D model (single d_p) has the lowest R-squared and the highest AIC. The other models show similar performance, with the plateau model giving the best overall results.

Table 4.9: Model parameters (kinetic and mass transfer) for all the proposed models including quality indicators. In the lower part of the table, the parameters for the non-squared channels are presented.

			Single dp	Lineal dp	Exp dp	Plateau dp	Dual Pore
Kinetic parameters	Site1	kao(1,1)	5.99E+04	6.72E+04	2.32E+04	8.87E+04	4.77E+04
	Site 2	kao(2,1)	6.46E+04	6.20E+04	8.56E+06	8.14E+04	6.95E+04
		kao(2,2)	5.57E+05	1.12E+09	1.89E+12	1.51E+09	5.57E+07
	Site 3	kao(3,1)	7.26E+03	2.46E+04	4.24E+04	3.19E+04	5.90E+04
		kao(3,2)	5.57E+04	1.44E+09	3.65E+12	6.61E+08	1.22E+08
	Site 4	kao(4,1)	1.17E+04	8.58E+02	5.58E+04	5.14E+04	5.20E+04
		kao(4,2)	5.57E+04	5.52E+08	4.51E+12	1.38E+09	1.05E+08
	Site 5	kao(5,1)	5.56E+04	7.76E+08	2.66E+12	3.77E+09	5.72E+09
		Ed(5,1) (J/mol)	6.59E+04	6.08E+04	6.47E+04	6.01E+04	6.30E+04
		kao(5,2)	8.57	3.01	4.02	3.23	3.09
Mass balance parameter		dpo (m)	5.18E+07	6.75E-07	3.93E-07	2.85E-07	1.05E+06
		δi		0.59	0.97	0.74	1.01
		δb			9.61	36.8	
		fd	0.58	0.49	0.51	0.53	0.38
		dpmicro (m)					4.53E-09
		φ					9.02E+03
Quality Indicators		R2	0.836	0.910	0.922	0.943	0.933
		AIC	-293569	-420000	-422380	-429000	-472527
		Non-square channnels					
Section distribution		α 10%	0.29	0.37	0.35	0.34	0.31
		α -10%	0.41	0.25	0.27	0.31	0.34
Quality Indicators		R2	0.88	0.933	0.948	0.961	0.939
		AIC	-309020	-386000	-456000	-481000	-497000
Remarks: Units of kao are (m3/kg.s)							

	Square channels			*Non-square channels*		
	R-sqrt	**# pars**	**AIC**	**R-sqrt**	**# pars**	**AIC**
Single dp	0.836	12	-293569	0.880	13	-309020
Lineal dp	0.910	13	-420000	0.933	14	-386000
Exp. dp	0.922	13	-422380	0.948	14	-456000
Plateau dp	0.943	13	-429000	0.961	14	-481000
Dual pore	0.933	14	-472527	0.939	15	-497000

Table 4.10: Quality indicators for all the proposed models.

4.6 Model Quality and External Validity

Assessing the quality of a catalyst model used in emission after-treatment systems requires more than visual comparisons between modelled and experimental data. Figures are useful tools for communication and quick checks, but

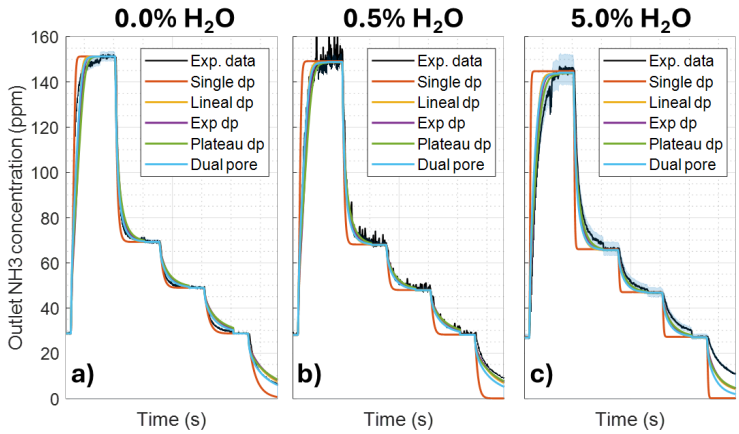

Figure 4.15: NH_3 outlet concentration for adsorption experiments on low NH_3 concentrations for an oxidized catalyst, at 100°C, for different water concentrations. Experimental data is the black solid line and the light blue area represents the error range calculated for the FTIR.

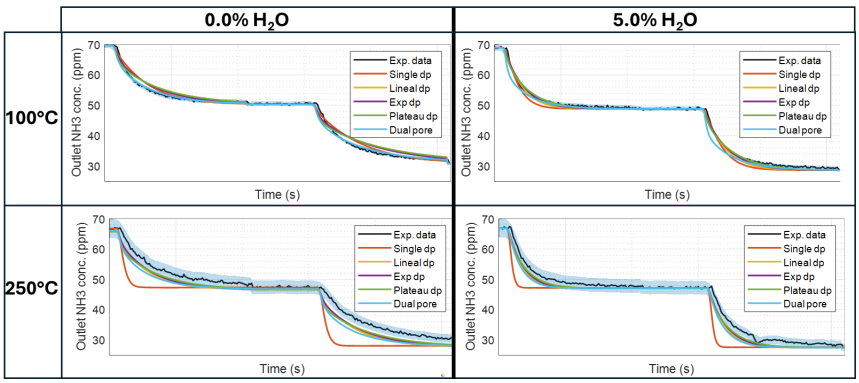

Figure 4.16: NH_3 outlet concentration for adsorption experiments (zoomed) on low NH_3 concentrations for a reduced catalyst at different temperatures and water concentrations. Experimental data is the black solid line and the light blue area represents the error range calculated for the FTIR.

they can be biased because the perception of the model is influenced by aesthetics such as scaling, style, data selection, and the tendency to focus on zones

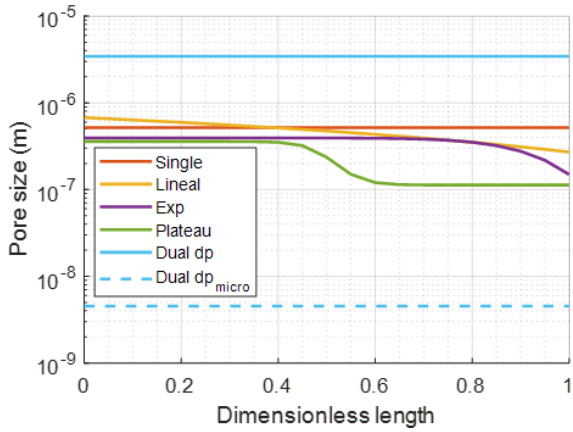

Figure 4.17: Mean pore size change as a function of washcoat dimensionless thickness. For the dual pore model, the macropore (solid line) and the micropore (dashed line) sizes are reported.

where the fit looks good. This can hide systematic deviations, which require a more quantitative assessment using goodness-of-fit indicators, parameter quality metrics, and a detailed residual analysis.

For model performance evaluation, several indicators can be estimated. These indicators evaluate how well the modelled data fits the experimental data. Indicators to be used include the coefficient of determination (R-squared) to describe explained variance, and AIC to balance lack of fit while penalizing model complexity. Other indicators include Marquardt's standard deviation and the Average Relative Error (ARE). Table 4.11 shows how these indicators are calculated [146], [161], [162], [163], [164], [165]. Moreover, using local estimations rather than only global ones helps identify zones where the fitting performance is poor. As an example Fig. 4.19 shows the accumulated ratio y_{mod}/y_{exp} for the NH_3 adsorption models evaluated with a detailed internal mass transfer definition. Some of the models tend to overestimate at low NH_3 concentrations and low temperatures (100°C), which is a sign of lack-of-fit.

However, a good fit is not always achieved with reliable parameters. This can indicate overfitting, which happens when some parameters do not actually describe the experimental data, so the model output becomes insensitive to changes in those parameters. Therefore, evaluation of parameter quality is

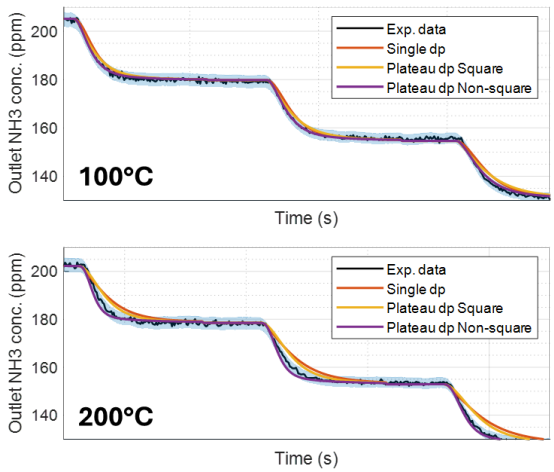

Figure 4.18: NH_3 outlet concentration for adsorption experiment (zoomed). Oxidized catalyst at 0% water, 100°C and 200°C. Comparison between the Single pore model and the best model (plateau), assuming squared and non-squared channels.

needed. This can be done by estimating the correlation matrix, which identifies pairwise correlations between parameters, and by estimating confidence intervals using a local covariance approximation from the Jacobian matrix. Wide confidence intervals and correlation values close to one indicate that the experimental data do not contain enough information to provide an independent estimation of that number of parameters and that parameter reduction or a revised model may be needed. For instance, the confidence intervals for the parameters on the catalyst models developed to study support effects on a Pd-based H_2-SCR catalysts is shown in Fig. 4.20. Most of the parameters are within the 95% confidence interval, with some exceptions on NO reaction orders and water inhibition parameters, suggesting that more information is needed from the experimental data. Also, Fig. 4.21 is a correlation matrix for the proposed NH_3 adsorption kinetic model developed at steady-state conditions. Some high values are explained as interactions in non-linear models.

A detailed residual analysis is important to detect systematic model deficiencies. It helps identify bias and structure, which can indicate missing physics in the model. From the residual structure, it is also possible to identify which

Quality Indicator	Indicator Equation
R-squared	$R^2 = 1 - \frac{\sum_{i=1}^{n}(y_{exp,i} - y_{mod,i})}{\sum_{i=1}^{n}(y_{exp,i} - \bar{y})}$
AIC	$AIC = n * \log\left(\frac{1}{n}\sum_{i=1}^{n}\left[\frac{y_{exp,i} - y_{mod,i}}{y_{exp,i}}\right]^2\right) + 2(p+1)$
ARE	$ARE = \frac{100}{n}\sum_{i=1}^{n}\left\lvert\frac{y_{mod,i} - y_{exp,i}}{y_{exp,i}}\right\rvert$
MSD	$MSD = \sqrt{\frac{1}{n-p}\sum_{i=1}^{n}\left[\frac{y_{exp,i} - y_{mod,i}}{y_{exp,i}}\right]^2}$

Table 4.11: Quality Indicators

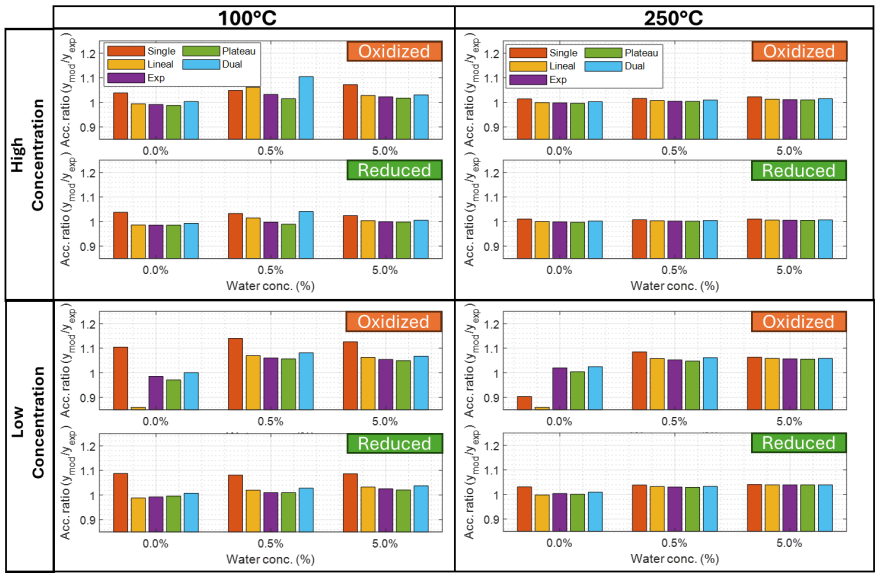

Figure 4.19: Accumulated ratio (y_{mod}/y_{exp}) for experiments at different NH_3 and H_2O concentration levels, oxidation states and temperatures [146], [161], [162], [163], [164], [165].

variables are most affected (flow, temperature, concentration, etc.). Residual analysis can also reveal autocorrelation, meaning the residuals are correlated in time, which violates the assumption that the error should be random and normally distributed [162], [163].

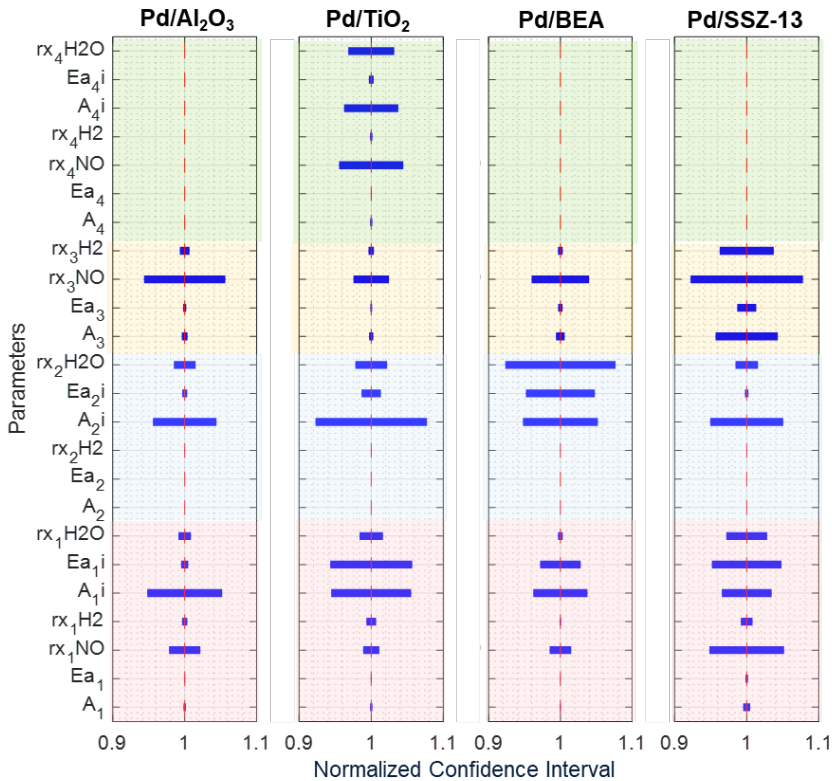

Figure 4.20: Normalized 95% confidence interval for the model parameters for the catalyst models developed for the studied H_2-SCR samples (The confidence interval is divided by the actual value of each parameter).

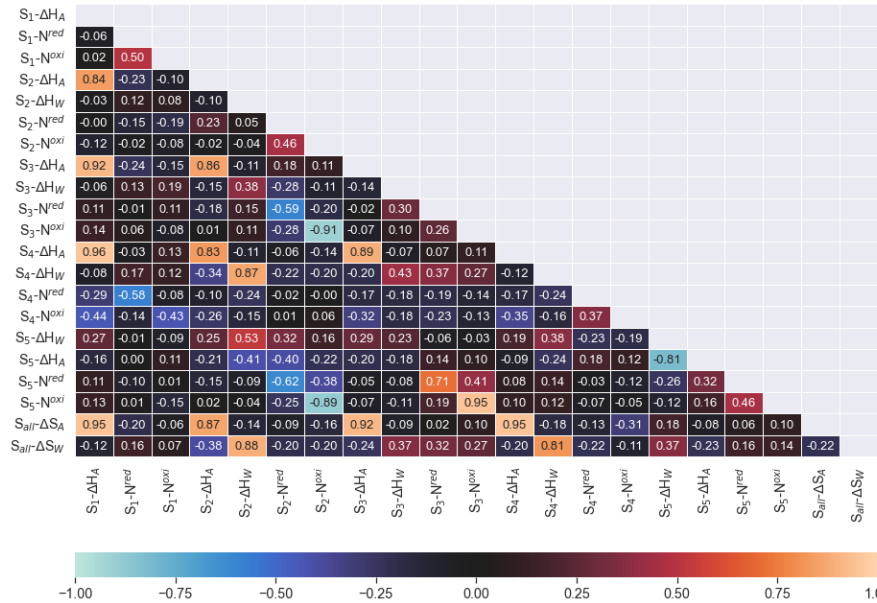

Figure 4.21: Correlation matrix for the selected NH_3 adsorption model. Taken from [166].

External validation refers to the capability to predict outside the region covered by the data used for parameter estimation, or to extrapolate beyond the experimental conditions. Mechanistic models can have stronger external validity because they are based on physics, but that validity depends on parameter estimation so that the parameters have physical meaning. This validity can be evaluated using a validation set that is not used in the parameter estimation task. The experimental data is divided into one set for parameter estimation and one for validation. A common split is 75% of the data for parameter estimation and 25% for validation, randomly selected [164], [167].

In addition, robust parameter estimation can be performed using cross-validation techniques, where model parameters are estimated using different partitions of the experimental dataset [167], [168], [169]. The average value from all runs for each parameter is then used as the final estimate. However, this process is computationally expensive and is mainly used for models that can be solved quickly and robustly. That is the case for the modelling workflow

for the NH_3 adsorption case at steady-state. Fig. 4.22 shows the results of the cross-validation for a k-fold (5-fold) evaluation. The parameters from the cross-validation are more robust since they account for data uncertainties.

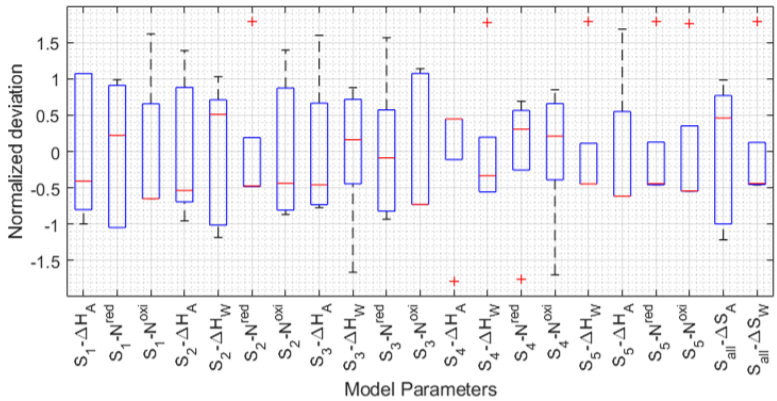

Figure 4.22: Cross-validation results with the parameter variation at each scenario. The red line represents the mean value used as the final value for the robust model. Taken from [166].

CHAPTER 5

Conclusions

"Our knowledge can only be finite,
while our ignorance must necessarily be infinite"

— Karl Popper

The transition to sustainable transportation will rely on the development of a wide technology portfolio, including the combustion engine, which is an attractive choice for long-haul and marine applications. Also, this technology will be used on an uneven transition: some regions can move faster toward low-carbon solutions, while others will depend longer on affordable systems and existing infrastructure. In this situation, emissions reduction in the coming years should come by the improvement of existing systems, such as the emission aftertreatment. The requirement for low emissions is reinforced by new legislation, such as Euro 7 and EPA 27, with stricter limits and monitoring strategies.

Meeting these demands and improving the emission aftertreatment system composed by sophisticated catalysts and control strategies will require the development of mechanistic models that can describe catalyst behaviour under realistic conditions. Mechanistic models are transparent, give insight without

losing physical meaning, and are the basis to more complicated modelling strategies using Machine Learning (ML) or Artificial Intelligence (AI).

This thesis proposed a modelling approach where mechanistic model structure, experimental data quality, and mass transfer effects are treated as one connected challenge. The work demonstrates that reliable mechanistic models are achievable when experiments are designed to maximize information, the experimental setup is characterized and artifacts are removed, and model structures are tested systematically instead of being assumed from the start. This is shown first through the development of high-quality NH_3 adsorption datasets for a monolith catalyst, where delay and dispersion are handled with a Residence Time Distribution (RTD) model and setup artifacts are identified and removed (**Paper A**). This data processing step is not optional and increase data quality. This work shows that artifacts can strongly distort adsorption values, especially at high temperature where storage is lower and the data is most sensitive. The proposed processing and normalization also enable integration of datasets from different samples, increasing the experimental region and supporting more robust parameter estimation (**Paper A**).

Building on this foundation, the thesis confirms that NH_3 storage on vanadium-based SCR catalysts is inherently multi-site and affected by different conditions on water concentration, temperature, and catalyst state (**Paper A**). The proposed NH_3 adsorption model considers 5 Langmuir-type adsorption sites where site characteristics differ (simple NH_3 adsorption, water-competitive adsorption, and water-activated adsorption), allowing the model to reproduce the main trends with temperature, water concentration, and catalyst state (**Paper B**). Linking steady-state parameters to adsorption enthalpy and entropy provides physical meaning and improves parameter validity beyond a single dataset, while the data-driven framework for model discrimination and sequential parameter estimation reduce the risk of overfitting and improve robustness (**Paper B**). Together, these results support the conclusion that mechanistic models can remain compact and still explain the observed behavior, as long as structure selection is done systematically and guided by data.

Another central conclusion is that mass transfer effects are relevant in SCR catalysts, and it must be represented with enough detail to avoid biased kinetics and misleading parameters. By extending a state-of-the-art 1+1D single channel model (SCM) framework, the thesis shows that describing washcoat

non-uniformity (variable pore size and macro/micropore regions) improves model performance more than adding geometric details such as non-square channels, with the largest fitting improvement at low NH_3 concentration and high temperature and water levels, regions that are important for automotive operation (**Paper D**). The work also shows that changing the mass transfer definition shifts estimated kinetic parameters, especially for adsorption steps involving water, highlighting the coupling between mass transfer and kinetics in the transition regime (**Paper D**). A practical outcome is that partial calibration using steady-state data can reduce parameter correlation and keep confidence intervals narrow while still benefiting from an improved mass transfer description (**Paper D**). At the same time, the results point to an improvement potential: the water-activated storage site is essential at low water concentrations, but its parameter indicate that a more detailed activation description is still required (**Paper D**).

For H_2-SCR catalysts, the thesis shows that H_2-SCR performance is strongly support dependent and characterized by the balance between NO reduction and competing H_2 oxidation. Activity testing and material characterization demonstrate that Pd/TiO_2 gives the highest NO conversion and N_2 yield and maintains good activity under wet conditions, consistent with reduced Pd states and support effects that suppress the fast hydrogen oxidation pathway (**Paper C**). A kinetic model coupled with internal and external mass transfer reproduces trends and levels across all supports for NO reduction to N_2, N_2O, and NH_3, together with H_2 oxidation (**Paper C**). Two selectivity findings are especially important for system design: NH_3 formation is observed only on Pd/TiO_2, while N_2O formation appears across supports (**Paper C**). The model also clarifies the role of mass transfer: as temperature increases, the system shifts from kinetic control toward mass transfer influence, and external mass transfer can indirectly improve H_2-SCR performance by restricting fast H_2 oxidation and leaving more H_2 available for NO reduction (**Paper C**).

Overall, the thesis advances catalyst modelling in a way that is relevant for the transportation sector: it delivers methods to obtain higher quality, more comparable experimental datasets (**Paper A**), a structured and data-driven framework to select mechanistic model structures with physical meaning (**Paper B**), improved washcoat and mass transfer descriptions that extend validity into challenging operating regions without increasing computational cost (**Paper D**), and a combined experimental, modelling framework for Pd-based

H_2-SCR that links support properties, kinetics, and mass transfer limitations (**Paper C**). Together, these outcomes strengthen the basis for aftertreatment analysis, catalyst design, and control strategies needed to meet strict emission limits during the years where combustion engines will still be a major part of heavy-duty transport.

CHAPTER 6

Future Outlook

Future work should focus on the main results from this thesis and how it will be possible to advance catalyst modelling for after-treatment purposes. Model quality improves the most when experiments, experimental setup characterization, model structure selection, and mass transfer descriptions are developed together. Modelling specific catalysts with different goals will lead to steps, within the frameworks, that can be improved to increase model quality. First, model validity should extend to more transient experiments and include more reaction steps to close the NH_3-SCR mechanism. This will allow to perform validation on heavy-duty application. Heavy-duty legislation demands accurate estimation under real, transient conditions to support control and OBD/OBM strategies. This shifts the focus to model properties such as robustness outside the model calibration set, sensitivity to disturbances, and estimation on real-time. In a vanadium-based NH_3-SCR catalyst, the high temperature and low NH_3 storage region is challenging from a model development perspective, since reactor artifacts, and delay and dispersion effects could dominate the experimental data if not handled carefully (**Paper A**).

Furthermore, the adsorption framework and mass transfer descriptions developed here for a vanadium-based SCR catalyst provide a strong base

(**Papers B and D**), but application-level prediction requires identifying and validating the parameters for the main SCR reactions as well as relevant competing pathways, including NH_3 oxidation and other side reactions that affect NH_3 selectivity. Completing this kinetic network will also make it possible to test the model under richer transient scenarios where storage, reaction rates, and transport limitations interact at the same time. In parallel, the modelling can be improved by refining the description of the water-activated storage behavior: the multi-site model captures the key trends and provides physically meaningful parameters through thermodynamic relations (**Paper B**), but the washcoat modelling study indicates that the water-activated site remains the most uncertain element and may require a more detailed activation mechanism (**Paper D**). Targeted experiments designed to isolate water effects, such as controlled water pulses, conditioning sequences, and step changes under carefully chosen temperatures, would help isolate this feature and narrow the confidence intervals of the parameter.

The improved model quality obtained by representing washcoat non-uniformity also shows that porous structure needs to be included in more detail, i.e. adding more features. Future work should strengthen the link between measured structure (gradients in pore size, macro/micropore regions, and defects) and modelling assumptions, so mass transfer parameters are less correlated with kinetic parameters (**Paper D**). Across both catalyst systems, identifiability in the kinetics–diffusion transition regime remains a core challenge, since kinetics and mass transfer act together and can create strong parameter correlation. The thesis shows that partial calibration strategies and careful quality assessment can control this problem (**Paper D**), but the next step is to investigate the requirements for deployment on application. In practice, it will involve the analyzing the different time scales and sensitivities between the gas flow reactor and application. Additionally, external validity will involve a more pragmatic approach: cross-validation across the operation regions (not only overall), and stress tests where input data degrade (noise, offset, bias, delays, etc.), and acceptance criteria to define when a parameter can be transferred to application.

For H_2-SCR, the support comparison and the kinetic model already show how strongly performance depends on the balance between NO reduction and competing reactions, and how external mass transfer can shift hydrogen availability (**Paper C**). However, a clear next step is to move from a power-law

description toward a more mechanistic model that includes key adsorbed species and captures support–metal interactions in more detail. This would help explain why certain supports (such as TiO_2) enable unique behaviour, and it would improve predictions in the difficult region where water and low H_2 concentration challenge simplified kinetics (**Paper C**). In the same direction, experiments and modelling with different washcoat thicknesses and cell densities (CPSI) would provide more information on internal and external mass transfer effects on hydrogen utilization.

Finally, for models to be relevant in the transportation sector, they require accounting for aging. Hydrothermal effects, and poisoning can change site density, storage behaviour, and mass transfer properties, so extending the workflow to aged samples would improve lifetime prediction and strengthen the connection to real fleets. At the same time, the models developed here are adequate for control strategies, since they give mechanistic insight into onboard monitoring and control actions aligned with stricter regulations. Moreover, in a broad perspective, mechanistic models should also be seen as the backbone for hybrid modelling with AI, where machine learning improves calibration efficiency, or residual prediction while the mechanistic core preserves mass balance, thermodynamic consistency, and interpretability, an advantage that becomes critical when operating conditions change and trust in the model is required (**Papers A–D**).

References

[1] G. H. Brundtland, "Our common future—call for action," *Environmental Conservation*, vol. 14, no. 4, pp. 291–294, 1987.

[2] R. Costanza et al., "The value of the world's ecosystem services and natural capital," *Nature*, vol. 387, no. 6630, pp. 253–260, 1997.

[3] W. V. Reid, *Millennium ecosystem assessment*. 2005.

[4] K. Richardson et al., "Earth beyond six of nine planetary boundaries," *Science advances*, vol. 9, no. 37, eadh2458, 2023.

[5] IEA, "World energy outlook 2022," *International Energy Agency (IEA)*, 2022.

[6] International Energy Agency. "Transport – energy system." Retrieved from the IEA website, Accessed: Dec. 15, 2025. [Online]. Available: `https://www.iea.org/energy-system/transport`.

[7] D. Banister, "The sustainable mobility paradigm," *Transport policy*, vol. 15, no. 2, pp. 73–80, 2008.

[8] P. K. Das, M. Y. Bhat, and S. Sajith, "Life cycle assessment of electric vehicles: A systematic review of literature," *Environmental Science and Pollution Research*, vol. 31, no. 1, pp. 73–89, 2024.

[9] D. B. Agusdinata and W. Liu, "Global sustainability of electric vehicles minerals: A critical review of news media," *The Extractive Industries and Society*, vol. 13, p. 101 231, 2023.

[10] F. Rouhana, J. Zhu, D. Chacon-Hurtado, S. Hertel, and A. C. Bagtzoglou, "Ensuring a just transition: The electric vehicle revolution from a human rights perspective," *Journal of Cleaner Production*, vol. 462, p. 142 667, 2024.

[11] A. J. Ojeda-Diaz, R. Krueger, A. F. Jensen, and S. Haustein, "The (un-) intended consequences of transport electrification: A scoping review of rebound and spillover effects," *Transport Reviews*, pp. 1–32, 2025.

[12] D. Font Vivanco, J. Freire-González, R. Kemp, and E. van der Voet, "The remarkable environmental rebound effect of electric cars: A microeconomic approach," *Environmental science & technology*, vol. 48, no. 20, pp. 12 063–12 072, 2014.

[13] B. Guan, R. Zhan, H. Lin, and Z. Huang, "Review of state of the art technologies of selective catalytic reduction of NO_x from diesel engine exhaust," *Applied Thermal Engineering*, vol. 66, no. 1-2, pp. 395–414, 2014.

[14] Z. Chen, Q. Liu, H. Liu, and T. Wang, "Recent advances in scr systems of heavy-duty diesel vehicles—low-temperature NO_x reduction technology and combination of SCR with remote OBD," *Atmosphere*, vol. 15, no. 8, p. 997, 2024.

[15] A. Bamberg, L. Urbas, S. Bröcker, M. Bortz, and N. Kockmann, "The digital twin–your ingenious companion for process engineering and smart production," *Chemical Engineering & Technology*, vol. 44, no. 6, pp. 954–961, 2021.

[16] L. Peterson, I. V. Gosea, P. Benner, and K. Sundmacher, "Digital twins in process engineering: An overview on computational and numerical methods," *Computers & Chemical Engineering*, vol. 193, p. 108 917, 2025.

[17] C. M. Rebello and I. B. Nogueira, "Digital twins in chemical engineering: An integrated framework for identification, implementation, online learning, and uncertainty assessment," *Computers & Chemical Engineering*, p. 109 178, 2025.

[18] J. Mädler, J. Rahm, I. Viedt, and L. Urbas, "A digital twin-concept for smart process equipment assemblies supporting process validation in modular plants," in *Computer Aided Chemical Engineering*, vol. 51, Elsevier, 2022, pp. 1435–1440.

[19] Hexagon AB, *Digital twin industry report*, https://aliresources.hexagon.com/digital-twin/digital-twin-industry-report, White paper, 2024.

[20] E. H. Stitt, J. Emerson, C. Jackson, and R. Gallen, "Demystifying and debunking ML part 1: Foundations of machine learning in ChemEng," *The Chemical Engineer*, 2025, Online series.

[21] E. H. Stitt, J. Emerson, C. Jackson, and R. Gallen, "Demystifying and debunking ML part 2: Foundations of machine learning in chemeng," *The Chemical Engineer*, 2025, Online series.

[22] E. Casillo, T. Scattolin, and S. P. Nolan, "Catalysis meets machine learning: A guide to data-driven discovery and design," *Chemical Communications*, vol. 61, no. 93, pp. 18 247–18 272, 2025.

[23] H. M. Cartwright, *Machine learning in chemistry: the impact of artificial intelligence*. Royal Society of Chemistry, 2020, vol. 17.

[24] A. Thebelt, J. Wiebe, J. Kronqvist, C. Tsay, and R. Misener, "Maximizing information from chemical engineering data sets: Applications to machine learning," *Chemical Engineering Science*, vol. 252, p. 117 469, 2022.

[25] D. H. Wolpert and W. G. Macready, "No free lunch theorems for optimization," *IEEE transactions on evolutionary computation*, vol. 1, no. 1, pp. 67–82, 2002.

[26] A. Speck-Planche, V. Kleandrova, and H. Cartwright, *Machine learning in chemistry: The impact of artificial intelligence*, 2020.

[27] H. Narayanan, M. von Stosch, F. Feidl, M. Sokolov, M. Morbidelli, and A. Butté, "Hybrid modeling for biopharmaceutical processes: Advantages, opportunities, and implementation," *Frontiers in Chemical Engineering*, vol. 5, p. 1 157 889, 2023.

[28] International Energy Agency (IEA), "World energy outlook 2025," International Energy Agency, Paris, France, Tech. Rep., Nov. 2025.

[29] ICCT. "ICCTs comments and technical recommendations on future Euro 7/VII emission standards," Accessed: Sep. 1, 2024. [Online]. Available: https://theicct.org/sites/default/files/eu-commission-euro-7-and-VI-may2021.pdf.

[30] P. Jaramillo et al., "Transport," in *Climate Change 2022: Mitigation of Climate Change. Contribution of Working Group III to the Sixth Assessment Report of the Intergovernmental Panel on Climate Change*, Cambridge, UK and New York, NY, USA: Cambridge University Press, 2022.

[31] International Energy Agency (IEA), "The future of trucks: Implications for energy and the environment," International Energy Agency, Paris, France, Tech. Rep., 2017.

[32] European Automobile Manufacturers' Association (ACEA). "Average age of the EU vehicle fleet, by country."

[33] Association for Emissions Control by Catalyst (AECC), "Heavy-duty Euro 7 update and AECC demonstration programmes," AECC, Chengdu, China, Presentation at the International Symposium of Low Emissions and Fuel Efficient Technologies to Meet China 7 Requirements, Mar. 2024, Accessed: 2025-01-19.

[34] J. Teter et al., "The future of trucks: Implications for energy and the environment," 2017.

[35] F. Rodriguez and F. Posada, "Future heavy-duty emission standards," *International Council for Clean Transportation*, 2019.

[36] OECD, "Energy and air pollution: World energy outlook special report 2016," 2016.

[37] IEA. "World energy outlook 2019," Accessed: Sep. 1, 2012. [Online]. Available: `https://www.iea.org/reports/world-energy-outlook-2019`.

[38] W. F. Lamb et al., "A review of trends and drivers of greenhouse gas emissions by sector from 1990 to 2018," *Environmental Research Letters*, 2021.

[39] BP, "BP energy outlook 2025," BP, London, United Kingdom, Tech. Rep., Sep. 2025.

[40] BP, *BP energy outlook 2019*, 2020.

[41] International Energy Agency, "Global EV outlook 2024," International Energy Agency (IEA), Paris, France, Tech. Rep., 2024.

[42] Shell, "The 2025 energy security scenarios: Energy and artificial intelligence," Shell, The Hague, Netherlands, Tech. Rep., Feb. 2025.

[43] Hydrogen Council and McKinsey & Company, "Hydrogen insights december 2023: The state of the global hydrogen economy, with a deep dive into renewable hydrogen cost evolution," Hydrogen Council, Geneva, Switzerland, Tech. Rep., 2023.

[44] A. O'Connell, N. Pavlenko, G. Bieker, and S. Searle, "A comparison of the life-cycle greenhouse gas emissions of european heavy-duty vehicles and fuels," *International Council on Clean Transportation: Washington, DC, USA*, pp. 1–36, 2023.

[45] International Energy Agency (IEA), "Global critical minerals outlook 2025," International Energy Agency, Paris, France, Tech. Rep., 2025.

[46] R. Ramirez and A. Wilkinson, *Strategic reframing: The Oxford scenario planning approach*. Oxford University Press, 2016.

[47] G. Lyons, C. Rohr, A. Smith, A. Rothnie, and A. Curry, "Scenario planning for transport practitioners," *Transportation Research Interdisciplinary Perspectives*, vol. 11, p. 100 438, 2021.

[48] Scania Group. "Modelling the future: Three scenarios for transport." Accessed: 2024-12-01. [Online]. Available: `https://www.scania.com/group/en/home/about-scania/scania-in-brief/a-strategy-to-drive-the-shift/modelling-the-future-three-scenarios-for-transport.html`.

[49] D. Sperling and J. S. Cannon, *Reducing climate impacts in the transportation sector*. Springer, 2009.

[50] DNV AS, "Energy transition outlook 2025: A global and regional forecast to 2060," DNV AS, Høvik, Norway, Tech. Rep., Oct. 2025.

[51] McKinsey & Company, "Global energy perspective 2025," McKinsey & Company, New York, NY, USA, Tech. Rep., Oct. 2025.

[52] M. A. Kose and F. Ohnsorge, *Falling long-term growth prospects: trends, expectations, and policies*. World Bank Publications, 2024.

[53] W. B. Group, *Global Economic Prospects*. World Bank Publications, 2026.

[54] D. Luhnow, T. Fairless, and A. Barnett, "How Europe is losing the global tech race, in five charts," *The Wall Street Journal*, Jun. 2025, Accessed: 2026-01-04.

[55] A. Berg, "Europe and the global economic order," Centre for European Reform, London, Policy Brief, Jan. 2025.

[56] Y. Guillemette and J. Château, "Long-term scenarios: Incorporating the energy transition," *OECD Economic Policy Papers*, 2023.

[57] F. Monitor, *Putting a lid on public debt. International Monetary Fund (IMF).(ct. 2024)*.

[58] M. A. Martin-Valmayor, N. Carmona-Gonzalez, M.-P. Sánchez-Martín, and L. A. Gil-Alana, "Persistence in sovereign debt during the past two centuries: Evidence for the US and the largest european economies," *Economic Analysis and Policy*, vol. 83, pp. 390–403, 2024.

[59] T. Leopold, A. Di Battista, X. Jativa, S. Sharma, R. Li, and S. Grayling, "Future of jobs report 2025," in *World Economic Forum. https://www. weforum. org/reports/the-future-ofjobs-report-2025*, 2025.

[60] C. McKerracher, "China already makes as many batteries as the entire world wants," *Bloomberg*, Apr. 2024.

[61] T. Lombardo, L. Paoli, A. Fernandez Pales, and T. Gül, *The battery industry has entered a new phase*, IEA Commentary, Mar. 2025.

[62] M. F. Cancian, M. Cancian, and E. Heginbotham, *The First Battle of the Next War*. Washington, DC: Center for Strategic & International Studies, 2023.

[63] ACEA. "ACEA position paper views on proposals for Euro 7 emission standard," Accessed: Sep. 1, 2024. [Online]. Available: `https://www.acea.auto/files/ACEA_Position_Paper-Views_on_proposals_for_Euro_7_emission_standard.pdf`.

[64] M. T. Fravel, "Power shifts and escalation: Explaining China's use of force in territorial disputes," *International Security*, vol. 32, no. 3, pp. 44–83, 2007.

[65] S. Gänzle, B. Leruth, and J. Trondal, "Differentiation, differentiated integration and disintegration in a 'post-Brexit-era'," in *Differentiated integration and disintegration in a post-Brexit era*, Routledge, 2019, pp. 1–18.

[66] H. Dijkstra and M. J. Debre, "The death of major international organizations: When institutional stickiness is not enough," *Global Studies Quarterly*, vol. 2, no. 4, ksac048, 2022.

[67] CARB. "Zero emission vehicle (ZEV) program," Accessed: Sep. 1, 2012. [Online]. Available: https://ww2.arb.ca.gov/our-work/programs/zero-emission-vehicle-program.

[68] European Commission, Directorate-General for Internal Market, Industry, Entrepreneurship and SMEs (DG GROW) / Advisory Group on Vehicle Emission Standards (AGVES), "On-board monitoring of emissions – focus on heavy-duty issues, off-board data communication and environmental vehicle passport (EVP)," European Commission, Brussels, Belgium, AGVES Meeting Presentation, 2024.

[69] United Nations Economic Commission for Europe, "Euro 7: New proposal for vehicle emissions type approval in europe," UNECE – Working Party on Pollution and Energy (GRPE), Geneva, Switzerland, Informal document, GRPE-87-37/Rev.1, 2023, Presented at the eighty-seventh session of GRPE (10–13 Jan 2023), Working Party on Pollution and Energy (WP.29/GRPE).

[70] TE. "Road to zero: The last EU emission standard for cars, vans, buses and trucks," Accessed: Sep. 1, 2024. [Online]. Available: https://www.transportenvironment.org/wp-content/uploads/2021/06/2020_04_Road_to_Zero_last_EU_emission_standard_cars_vans_buses_trucks.pdf.

[71] ICCT. "Transportpolicy.net," Accessed: Sep. 1, 2021. [Online]. Available: https://www.transportpolicy.net/?title=Main_Page.

[72] AGVES. "Preliminary findings on possible Euro 7 emission limits for LD and HD vehicles," Accessed: Sep. 1, 2024. [Online]. Available: https://circabc.europa.eu/sd/a/fdd70a2d-b50a-4d0b-a92a-e64d41d0e947/CLOVE%5C%20test%5C%20limits%5C%20AGVES%5C%202020-10-27%5C%20final%5C%20vs2.pdf.

[73] U.S. Environmental Protection Agency (EPA), "EPA's heavy-duty 2027 final rule: An overview for NACAA mobile source fuels committee," National Association of Clean Air Agencies (NACAA), Washington, D.C., USA, Tech. Rep., Mar. 2023.

[74] EPA/NHTSA, "Final rule for greenhouse gas emissions and fuel efficiency standards for medium- and heavy-duty engines and vehicles - phase 2," 2016.

[75] C. Sharp, G. Neely, B. Zavala, and S. Rao, "CARB low NO_X Stage 3 program-final results and summary," SAE Technical Paper, Tech. Rep., 2021.

[76] P. Li and L. Lü, "Evaluating the real-world NO_x emission from a China VI heavy-duty diesel vehicle," *Applied Sciences*, 2021.

[77] Z. Ge et al., "Real-road NO_x and CO_2 emissions of city and highway China VI heavy-duty diesel vehicles," *Journal of Environmental Sciences*, 2023.

[78] Tengyuntruck.com. "Euro 7's impact: A preview of China VII." Accessed: 2025-01-19. [Online]. Available: `https://www.tengyuntruck.com/info/euro-vii-s-impact-a-preview-of-china-vii-for-103045700.html`.

[79] B. Zavala, C. Sharp, G. Neely, and S. Rao, "CARB low NO_X stage 3 Program-Aftertreatment evaluation and final demonstration system results," *SAE Technical Paper*, pp. 01–1402, 2020.

[80] S. Rao, J. Sarlashkar, S. Rengarajan, C. Sharp, and G. Neely, "A controls overview on achieving ultra-low NO_X," SAE Technical Paper, Tech. Rep., 2020.

[81] J. Kim, "Exhaust emissions and aftertreatments of hydrogen internal combustion engines: A review," *International Journal of Automotive Technology*, vol. 24, no. 6, pp. 1681–1690, 2023.

[82] J. K. Unni, D. Bhatia, V. Dutta, L. M. Das, S. Jilakara, and G. Subash, "Development of hydrogen fuelled low NO_x engine with exhaust gas recirculation and exhaust after treatment," *SAE International Journal of Engines*, vol. 10, no. 1, pp. 46–54, 2017.

[83] C. Özyalcin, S. Sterlepper, S. Roiser, H. Eichlseder, and S. Pischinger, "Exhaust gas aftertreatment to minimize NO_x emissions from hydrogen-fueled internal combustion engines," *Applied Energy*, vol. 353, p. 122 045, 2024.

[84] S. M. Farhan, W. Pan, C. Zhijian, and Y. JianJun, "Innovative catalysts for the selective catalytic reduction of NO_x with H_2: A systematic review," *Fuel*, vol. 355, p. 129 364, 2024.

[85] Y. Guan, Y. Liu, Q. Lv, B. Wang, and D. Che, "Review on the selective catalytic reduction of NO_x with H_2 by using novel catalysts," *Journal of Environmental Chemical Engineering*, vol. 9, no. 6, p. 106 770, 2021.

[86] J. Shibata, M. Hashimoto, K.-i. Shimizu, H. Yoshida, T. Hattori, and A. Satsuma, "Factors controlling activity and selectivity for SCR of NO by hydrogen over supported platinum catalysts," *The Journal of Physical Chemistry B*, vol. 108, no. 47, pp. 18 327–18 335, 2004.

[87] G. Qi, R. T. Yang, and F. C. Rinaldi, "Selective catalytic reduction of nitric oxide with hydrogen over Pd-based catalysts," *Journal of Catalysis*, vol. 237, no. 2, pp. 381–392, 2006.

[88] X. Zhang, X. Wang, X. Zhao, Y. Xu, H. Gao, and F. Zhang, "An investigation on N_2O formation route over Pt/HY in H_2-SCR," *Chemical Engineering Journal*, vol. 252, pp. 288–297, 2014.

[89] I. E. Wachs and B. M. Weckhuysen, "Structure and reactivity of surface vanadium oxide species on oxide supports," *Applied Catalysis A: General*, vol. 157, no. 1-2, pp. 67–90, 1997.

[90] R. M. Heck, R. J. Farrauto, and S. T. Gulati, *Catalytic air pollution control: commercial technology*. John Wiley & Sons, 2016.

[91] N.-Y. Topsøe, M. Anstrom, and J. Dumesic, "Raman, FTIR and theoretical evidence for dynamic structural rearrangements of vanadia/titania $DeNO_X$ catalysts," *Catalysis letters*, vol. 76, no. 1, pp. 11–20, 2001.

[92] R.-M. Yuan, G. Fu, X. Xu, and H.-L. Wan, "Brønsted-NH^{4+} mechanism versus nitrite mechanism: New insight into the selective catalytic reduction of NO by NH_3," *Physical Chemistry Chemical Physics*, vol. 13, no. 2, pp. 453–460, 2011.

[93] I. E. Wachs et al., "Selective catalytic reduction of NO with NH_3 over supported vanadia catalysts," *Journal of Catalysis*, vol. 161, no. 1, pp. 211–221, 1996.

[94] M. Turco, L. Lisi, R. Pirone, and P. Ciambelli, "Effect of water on the kinetics of nitric oxide reduction over a high-surface-area V_2O_5/TiO_2 catalyst," *Applied Catalysis B: Environmental*, vol. 3, no. 2-3, pp. 133–149, 1994.

[95] G. Busca, L. Lietti, G. Ramis, and F. Berti, "Chemical and mechanistic aspects of the selective catalytic reduction of NO_X by ammonia over oxide catalysts: A review," *Applied Catalysis B: Environmental*, vol. 18, no. 1-2, pp. 1–36, 1998.

[96] W. Wong and K. Nobe, "Kinetics of nitric oxide reduction with ammonia on" chemical mixed" and impregnated vanadium (V) oxide-titanium (IV) oxide catalysts," *Industrial & engineering chemistry product research and development*, vol. 23, no. 4, pp. 564–568, 1984.

[97] T. Komatsu, M. Nunokawa, I. S. Moon, T. Takahara, S. Namba, and T. Yashima, "Kinetic studies of reduction of nitric oxide with ammonia on Cu^{2+}-exchanged zeolites," *Journal of Catalysis*, vol. 148, no. 2, pp. 427–437, 1994.

[98] H.-G. Lintz and T. Turek, "Intrinsic kinetics of nitric oxide reduction by ammonia on a vanadia-titania catalyst," *Applied Catalysis A: General*, vol. 85, no. 1, pp. 13–25, 1992.

[99] S. Xiong, X. Xiao, Y. Liao, H. Dang, W. Shan, and S. Yang, "Global kinetic study of NO reduction by NH_3 over V_2O_5–WO_3/TiO_2: Relationship between the SCR performance and the key factors," *Industrial & Engineering Chemistry Research*, vol. 54, no. 44, pp. 11 011–11 023, 2015.

[100] F. J. Janssen, F. M. Van den Kerkhof, H. Bosch, and J. R. Ross, "Mechanism of the reaction of nitric oxide, ammonia, and oxygen over vanadia catalysts. 2. Isotopic transient studies with oxygen-18 and nitrogen-15," *Journal of Physical Chemistry*, vol. 91, no. 27, pp. 6633–6638, 1987.

[101] N.-Y. Topsøe, "Mechanism of the selective catalytic reduction of nitric oxide by ammonia elucidated by in situ on-line Fourier transform infrared spectroscopy," *Science*, vol. 265, no. 5176, pp. 1217–1219, 1994.

[102] N. Topsoe, H. Topsoe, and J. Dumesic, "Vanadia/titania catalysts for selective catalytic reduction (SCR) of nitric-oxide by ammonia: I. Combined temperature-programmed in-situ FTIR and on-line mass-spectroscopy studies," *Journal of Catalysis*, vol. 151, no. 1, pp. 226–240, 1995.

[103] M. Takagi, T. Kawai, M. Soma, T. Onishi, and K. Tamaru, "The mechanism of the reaction between NO_X and NH_3 on V_2O_5 in the presence of oxygen," *Journal of Catalysis*, vol. 50, no. 3, pp. 441–446, 1977.

[104] L. Arnarson, H. Falsig, S. B. Rasmussen, J. V. Lauritsen, and P. G. Moses, "A complete reaction mechanism for standard and fast selective catalytic reduction of nitrogen oxides on low coverage VO_X/TiO_2 (001) catalysts," *Journal of catalysis*, vol. 346, pp. 188–197, 2017.

[105] L. Arnarson L., H. Falsig, S. B. Rasmussen, J. V. Lauritsen, and P. G. Moses, "The reaction mechanism for the SCR process on monomer V^{5+} sites and the effect of modified Brønsted acidity," *Physical Chemistry Chemical Physics*, vol. 18, no. 25, pp. 17 071–17 080, 2016.

[106] G. He et al., "Polymeric vanadyl species determine the low-temperature activity of V-based catalysts for the SCR of NO_X with NH_3," *Science advances*, vol. 4, no. 11, eaau4637, 2018.

[107] S. Soyer, A. Uzun, S. Senkan, and I. Onal, "A quantum chemical study of nitric oxide reduction by ammonia (SCR reaction) on V_2O_5 catalyst surface," *Catalysis today*, vol. 118, no. 3-4, pp. 268–278, 2006.

[108] E. Tronconi, I. Nova, C. Ciardelli, D. Chatterjee, B. Bandl-Konrad, and T. Burkhardt, "Modelling of an SCR catalytic converter for diesel exhaust after treatment: Dynamic effects at low temperature," *Catalysis Today*, vol. 105, no. 3-4, pp. 529–536, 2005.

[109] I. Nova, C. Ciardelli, E. Tronconi, D. Chatterjee, and B. Bandl-Konrad, "NH_3-SCR of NO over a V-based catalyst: Low-t redox kinetics with NH_3 inhibition," *AIChE Journal*, vol. 52, no. 9, pp. 3222–3233, 2006.

[110] J. Dumesic, N.-Y. Topsøe, H. Topsøe, Y. Chen, and T. Slabiak, "Kinetics of selective catalytic reduction of nitric oxide by ammonia over vanadia/titania," *Journal of catalysis*, vol. 163, no. 2, pp. 409–417, 1996.

[111] C. Ciardelli, I. Nova, E. Tronconi, D. Chatterjee, T. Burkhardt, and M. Weibel, "NH_3 SCR of NO_X for diesel exhausts aftertreatment: Role of NO_2 in catalytic mechanism, unsteady kinetics and monolith converter modelling," *Chemical Engineering Science*, vol. 62, no. 18-20, pp. 5001–5006, 2007.

[112] I. Nova, L. Lietti, E. Tronconi, and P. Forzatti, "Transient response method applied to the kinetic analysis of the $DeNO_X$–SCR reaction," *Chemical Engineering Science*, vol. 56, no. 4, pp. 1229–1237, 2001.

[113] M. Colombo, I. Nova, and E. Tronconi, "Detailed kinetic modeling of the NH_3–NO/NO_2 SCR reactions over a commercial Cu-zeolite catalyst for diesel exhausts after treatment," *Catalysis Today*, vol. 197, no. 1, pp. 243–255, 2012.

[114] M. Zhu, J.-K. Lai, U. Tumuluri, Z. Wu, and I. E. Wachs, "Nature of active sites and surface intermediates during SCR of NO with NH_3 by supported V_2O_5–WO_3/TiO_2 catalysts," *Journal of the American Chemical Society*, vol. 139, no. 44, pp. 15 624–15 627, 2017.

[115] X. Yin, H. Han, and A. Miyamoto, "Active site and mechanism of the selective catalytic reduction of NO by NH_3 over V_2O_5: A periodic first-principles study," *Physical Chemistry Chemical Physics*, vol. 2, no. 18, pp. 4243–4248, 2000.

[116] A. Vittadini, M. Casarin, and A. Selloni, "First principles studies of vanadia- titania monolayer catalysts: Mechanisms of NO selective reduction," *The Journal of Physical Chemistry B*, vol. 109, no. 5, pp. 1652–1655, 2005.

[117] H. S. Fogler, *Elements of chemical reaction engineering*. Pearson Educacion, 1999.

[118] O. Levenspiel, *Chemical reaction engineering*. John wiley & sons, 1998.

[119] I. Nova and E. Tronconi, *Urea-SCR technology for deNO$_x$ after treatment of diesel exhausts*. Springer, 2014, vol. 5.

[120] A. F. Suarez-Corredor, M. U. Babler, L. Olsson, M. Skoglundh, and B. Westerberg, "Characterization method for gas flow reactor experiments— NH_3 adsorption on vanadium-based SCR catalysts," *Industrial & Engineering Chemistry Research*, vol. 60, no. 30, pp. 11 399–11 411, 2021.

[121] A. Bueno-López, D. Lozano-Castelló, I. Such-Basáñez, J. García-Cortés, M. Illán-Gómez, and C. S.-M. de Lecea, "Preparation of beta-coated cordierite honeycomb monoliths by in situ synthesis: Utilisation as Pt support for NO_x abatement in diesel exhaust," *Applied Catalysis B: Environmental*, vol. 58, no. 1-2, pp. 1–7, 2005.

[122] A. Cybulski and J. A. Moulijn, "Monoliths in heterogeneous catalysis," *Catalysis Reviews—Science and Engineering*, vol. 36, no. 2, pp. 179–270, 1994.

[123] T. A. Nijhuis, A. E. Beers, T. Vergunst, I. Hoek, F. Kapteijn, and J. A. Moulijn, "Preparation of monolithic catalysts," *Catalysis Reviews*, vol. 43, no. 4, pp. 345–380, 2001.

[124] V. V. Fedorov and P. Hackl, *Model-oriented design of experiments*. Springer, 1997, vol. 125.

[125] G. E. Box, J. S. Hunter, and W. G. Hunter, *Statistics for experimenters: design, innovation, and discovery*. John Wiley & Sons, 2005.

[126] G. E. Box and N. R. Draper, "Response surfaces," *Mixtures, and Ridge Analyses*, vol. 649, 2007.

[127] G. E. Box and H. L. Lucas, "Design of experiments in non-linear situations," *Biometrika*, vol. 46, no. 1/2, pp. 77–90, 1959.

[128] B. P. Duarte and A. C. Atkinson, "Algorithms for optimal design of experiments," in *International Encyclopedia of Statistical Science*, Springer, 2025, pp. 46–51.

[129] D. Chatterjee, T. Burkhardt, M. Weibel, I. Nova, A. Grossale, and E. Tronconi, "Numerical simulation of zeolite-and V-based SCR catalytic converters," SAE technical paper, Tech. Rep., 2007.

[130] A. Åberg, A. Widd, J. Abildskov, and J. K. Huusom, "Estimation of kinetic parameters in an automotive SCR catalyst model," *Topics in Catalysis*, vol. 59, no. 10, pp. 945–951, 2016.

[131] A. Åberg, A. Widd, J. Abildskov, and J. K. Huusom, "Parameter estimation and analysis of an automotive heavy-duty SCR catalyst model," *Chemical Engineering Science*, vol. 161, pp. 167–177, 2017.

[132] E. Tronconi and P. Forzatti, "Adequacy of lumped parameter models for SCR reactors with monolith structure," *AIChE Journal*, vol. 38, no. 2, pp. 201–210, 1992.

[133] S. Y. Joshi, M. P. Harold, and V. Balakotaiah, "Overall mass transfer coefficients and controlling regimes in catalytic monoliths," *Chemical Engineering Science*, vol. 65, no. 5, pp. 1729–1747, 2010.

[134] M. Walander et al., "Modelling of mass transfer resistances in non-uniformly washcoated monolith reactors," *Emission Control Science and Technology*, vol. 7, no. 2, pp. 153–162, 2021.

[135] C. Zhong, J. Gong, L. Tan, W. Liu, G. Liu, and Z. Zhang, "Modeling intraphase and interphase mass transfer limitations for NH_3-SCR over Cu-ZSM-5," *Chemical Engineering Science*, vol. 207, pp. 479–489, 2019.

[136] A. Güthenke et al., "Current status of modeling lean exhaust gas aftertreatment catalysts," *Advances in chemical engineering*, vol. 33, pp. 103–283, 2007.

[137] E. Tronconi, "Interaction between chemical kinetics and transport phenomena in monolithic catalysts," *Catalysis today*, vol. 34, no. 3-4, pp. 421–427, 1997.

[138] P. S. Metkar, N. Salazar, R. Muncrief, V. Balakotaiah, and M. P. Harold, "Selective catalytic reduction of NO with NH_3 on iron zeolite monolithic catalysts: Steady-state and transient kinetics," *Applied Catalysis B: Environmental*, vol. 104, no. 1-2, pp. 110–126, 2011.

[139] J. M. Thomas and W. J. Thomas, *Principles and practice of heterogeneous catalysis*. John Wiley & Sons, 2014.

[140] B. E. Poling, J. M. Prausnitz, O. John Paul, and R. C. Reid, *The properties of gases and liquids*. Mcgraw-hill New York, 2001, vol. 5.

[141] E. Tronconi and A. Beretta, "The role of inter-and intra-phase mass transfer in the SCR-DeNO$_x$ reaction over catalysts of different shapes," *Catalysis Today*, vol. 52, no. 2-3, pp. 249–258, 1999.

[142] I. Chorkendorff and J. W. Niemantsverdriet, *Concepts of modern catalysis and kinetics*. John Wiley & Sons, 2017.

[143] R. Tesser and E. Santacesaria, "Kinetics of heterogeneous reactions and related mechanisms," in *The Chemical Reactor from Laboratory to Industrial Plant: A Modern Approach to Chemical Reaction Engineering*, Springer, 2025, pp. 317–417.

[144] J. Wang and X. Guo, "Adsorption isotherm models: Classification, physical meaning, application and solving method," *Chemosphere*, vol. 258, p. 127 279, 2020.

[145] R. Daya, C. Desai, and B. Vernham, "Development and validation of a two-site kinetic model for NH_3-SCR over Cu-SSZ-13. Part 1. detailed global kinetics development based on mechanistic considerations," *Emission Control Science and Technology*, vol. 4, no. 3, pp. 143–171, 2018.

[146] K. Y. Foo and B. H. Hameed, "Insights into the modeling of adsorption isotherm systems," *Chemical engineering journal*, vol. 156, no. 1, pp. 2–10, 2010.

[147] B. Boulinguiez, P. Le Cloirec, and D. Wolbert, "Revisiting the determination of Langmuir parameters application to Tetrahydrothiophene adsorption onto activated carbon," *Langmuir*, vol. 24, no. 13, pp. 6420–6424, 2008.

[148] L. Lietti, I. Nova, S. Camurri, E. Tronconi, and P. Forzatti, "Dynamics of the SCR-DeNO$_x$ reaction by the transient-response method," *AIChE Journal*, vol. 43, no. 10, pp. 2559–2570, 1997.

[149] Q. Li, X. Yang, W. Dong, and Y. Du, "Kinetic monte carlo modeling of heterogeneous catalysis on silica thermal protective materials based on reactive molecular dynamics simulation," *International Journal of Heat and Mass Transfer*, vol. 236, p. 126 378, 2025.

[150] L. Olsson, M. Fredriksson, and R. J. Blint, "Kinetic modeling of sulfur poisoning and regeneration of lean NO$_x$ traps," *Applied Catalysis B: Environmental*, vol. 100, no. 1-2, pp. 31–41, 2010.

[151] P. Atkins and J. De Paula, *Elements of physical chemistry*. Oxford University Press, USA, 2013.

[152] A. F. S. Corredor, "An experimental and modeling framework for catalysis. NH$_3$ adsorption studies for a vanadium-based SCR catalyst," Chalmers Tekniska Hogskola (Sweden), 2021.

[153] F. Giraud et al., "Experimental microkinetic approach of De-NO$_X$ by NH$_3$ on V$_2$O$_5$/WO$_3$/TiO$_2$ catalysts. 1. Individual heats of adsorption of adsorbed NH$_3$ species on a sulfate-free TiO$_2$ support using adsorption isobars," *The Journal of Physical Chemistry C*, vol. 118, no. 29, pp. 15 664–15 676, 2014.

[154] V. Ranea, J. Vicente, E. Mola, P. Arnal, H. Thomas, and L. Gambaro, "Adsorption of H$_2$O on the (001) plane of V$_2$O$_5$: Chemisorption site identification," *Surface Science*, vol. 463, no. 2, pp. 115–124, 2000.

[155] P. Hejduk, M. Szaleniec, and M. Witko, "Molecular and dissociative adsorption of water at low-index V$_2$O$_5$ surfaces: DFT studies using cluster surface models," *Journal of Molecular Catalysis A: Chemical*, vol. 325, no. 1-2, pp. 98–104, 2010.

[156] Z. Zhao et al., "Density functional theory (DFT) studies of vanadium-titanium based selective catalytic reduction (SCR) catalysts," *Journal of Environmental Sciences*, vol. 90, pp. 119–137, 2020.

[157] H. S. Wahab, T. Bredow, and S. M. Aliwi, "Computational investigation of water and oxygen adsorption on the anatase TiO_2 (100) surface," *Journal of Molecular Structure: THEOCHEM*, vol. 868, no. 1-3, pp. 101–108, 2008.

[158] X. Yin et al., "NH_3 adsorption on the Brönsted and Lewis acid sites of V_2O_5 (010): A periodic density functional study," *The Journal of Physical Chemistry B*, vol. 103, no. 22, pp. 4701–4706, 1999.

[159] S. R. Gundlapally, R. Dudgeon, and S. Wahiduzzaman, "Efficient solution of washcoat diffusion-reaction problem for real-time simulations," *Emission Control Science and Technology*, vol. 4, no. 2, pp. 90–102, 2018.

[160] R. E. Hayes and I. Cornejo, "Multi-scale modelling of monolith reactors: A 30-year perspective from 1990 to 2020," *The Canadian Journal of Chemical Engineering*, vol. 99, no. 12, pp. 2589–2606, 2021.

[161] H. Akaike, "A new look at the statistical model identification," *IEEE transactions on automatic control*, vol. 19, no. 6, pp. 716–723, 1974.

[162] D. Anderson and K. Burnham, "Model selection and multi-model inference," *Second. NY: Springer-Verlag*, vol. 63, no. 2020, p. 10, 2004.

[163] N. R. Draper and H. Smith, *Applied regression analysis*. John Wiley & Sons, 1998, vol. 326.

[164] C. Chatfield, "Model uncertainty, data mining and statistical inference," *Journal of the Royal Statistical Society: Series A (Statistics in Society)*, vol. 158, no. 3, pp. 419–444, 1995.

[165] J. E. Cavanaugh and A. A. Neath, "The Akaike information criterion: Background, derivation, properties, application, interpretation, and refinements," *Wiley Interdisciplinary Reviews: Computational Statistics*, vol. 11, no. 3, e1460, 2019.

[166] A. F. Suarez-Corredor, M. U. Bäbler, L. Olsson, M. Skoglundh, and B. Westerberg, "Understanding the NH_3 adsorption mechanism on a vanadium-based SCR catalyst: A data-driven modeling approach," *Chemical Engineering Science*, vol. 262, p. 117 975, 2022.

[167] J. Franklin, "The elements of statistical learning: Data mining, inference and prediction," *The Mathematical Intelligencer*, vol. 27, no. 2, pp. 83–85, 2005.

[168] M. Kuhn, K. Johnson, et al., *Applied predictive modeling*. Springer, 2013, vol. 26.

[169] A. Airola, T. Pahikkala, W. Waegeman, B. De Baets, and T. Salakoski, "An experimental comparison of cross-validation techniques for estimating the area under the ROC curve," *Computational Statistics & Data Analysis*, vol. 55, no. 4, pp. 1828–1844, 2011.